SLAC–435
UC–414
(E)

A Measurement of the Left-Right Cross Section Asymmetry in Z^0 Production with Polarized e^+e^- Collisions*

Hwanbae Park

Stanford Linear Accelerator Center
Stanford University
Stanford, California 94309

December 1993

Prepared for the Department of Energy
under contract number DE–AC03–76SF00515

Printed in the United States of America. Available from the National Technical Information Service, U.S. Department of Commerce, 5285 Port Royal Road, Springfield, Virginia 22161.

* Ph.D. thesis, University of Oregon

ABSTRACT

The Stanford Linear Collider at SLAC is an e^+e^- collider running at $\sqrt{s} \approx M_Z$ and has provided an electron beam with longitudinal polarization at the SLC interaction point. The 1992 polarized run data were taken with the SLD detector. We present here the measurement of the left-right cross section asymmetry (A_{LR}) for the 1992 run.

The polarized run began in May and ended in September of 1992 at a mean center-of-mass energy of 91.56 GeV. Tower hit information of the liquid argon calorimeter and endcap warm iron calorimeter pads were used for selecting hadronic Z^0 or tau pair events. The SLD detector collected about 11,000 events during this run.

The magnitude of the longitudinal polarization of the electron beam was continuously measured by a polarimeter based on Compton scattering, and was monitored by a polarimeter based on Moller scattering. The luminosity-weighted average longitudinal polarization during the 1992 run was measured as 22.4 ± 0.6 (syst.)%.

From these data, the value of A_{LR} has been measured to be 0.102 ± 0.044 (stat.) ± 0.003 (syst.), corresponding to an effective electroweak mixing angle ($\sin^2 \theta_w^{\rm eff}$) of 0.2375 ± 0.0056 (stat.) ± 0.0004 (syst.). The error is dominated by the statistical error. This value of $\sin^2 \theta_w^{\rm eff}$ is in good agreement with existing measurements from other experiments. Studies of improvements in A_{LR} event selection for future high-statistics runs are also discussed.

ACKNOWLEDGEMENTS

I am especially grateful to my advisor, Raymond Frey, for his guidance and invaluable advice. I also owe a tremendous debt of gratitude to James Brau who encouraged and supported my graduate studies over many years.

I also thank the members of the University of Oregon Luminosity Group: Jennifer Huber, Matthew Langston, Kevin Pitts, Cary Zeitlin and Jingchen Zhou, as well as the members of the University of Tennessee Luminosity Group: William Bugg, Robert Kroeger, Achim Weidemann and Sharon White.

Many thanks to the Electroweak Group and all the members of the SLD Collaboration.

My appreciation also goes to the following people for their help, encouragement and friendship: Ram Ben-David, Philip Burrows, Richard Dubois, Robert Elia, Saul González, Sarah Hedges, Andrea Higashi, Amitabh Lath, Peter Rowson and John Yamartino

This work was only made possible with the support and love of my family and parents. I especially want to thank my wife, Hyunju Ku, for her support and patience.

TABLE OF CONTENTS

LIST OF TABLES

LIST OF FIGURES

CHAPTER I

LEFT-RIGHT CROSS SECTION ASYMMETRY

Introduction

The electroweak Standard Model is known as a gauge theory, comprised of the $SU(2) \bigotimes U(1)$ gauge groups. It is a combination of weak and electromagnetic forces. The electroweak Standard Model was proposed by Glashow, Weinberg, and Salam [1]. It includes the gauge unification of weak and electromagnetic interactions which are based on the $SU(2)$ and $U(1)$ gauge groups, respectively. The interactions are specified by couplings of a weak isospin current of fermions to massless $SU(2)$ iso-triplet gauge fields ($\vec{W}$), and a weak hypercharge current of fermions to a massless $U(1)$ iso-singlet gauge field (B) [2].

The weak isospin is a quantum number to explain different charge substates of one particle and is conserved in the strong interaction. The weak hypercharge (Y) has the following relation with the weak isospin:

$$\frac{Y}{2} = Q - I_3 \tag{1}$$

where Q is the electric charge in units of $|e|$ and I_3 is the third component of the weak isospin.

The electroweak Standard Model has four physical spin-one vector gauge bosons, resulting from symmetry breaking [3]. This symmetry breaking is achieved by introducing the Higgs field, and three physical vector bosons acquire mass and one remains a massless boson which is identified as the photon. The mass eigenstates are given as follows:

$$W^{\pm} = \frac{1}{\sqrt{2}}(W_1 \pm iW_2) \tag{2}$$

$$A = \frac{1}{\sqrt{(g^2 + g'^2)}}(g'W_3 + gB) \tag{3}$$

$$Z^{\circ} = \frac{1}{\sqrt{(g^2 + g'^2)}}(gW_3 - g'B) \tag{4}$$

where g and g' are coupling constants for the weak isospin group $SU(2)$ and weak hypercharge group $U(1)$. The ratio of $U(1)$ and $SU(2)$ coupling constants defines a weak mixing angle:

$$\tan\theta_w = \frac{g'}{g} \tag{5}$$

One massless and electrically neutral boson, the photon (A), mediates the electromagnetic force over an infinite range between particles. On the other hand, two massive charged bosons ($W^{\pm}$) and one electrically neutral boson (Z°) mediate the weak force over a finite range. The existence of the massive gauge bosons, $W^{\pm}$ and Z°, were confirmed by hadron collider experiments in 1983 [4].

Table 1.1 shows the properties of these four physical gauge bosons.

Gauge Boson	Mass (GeV)	Electric Charge	spin	Force
γ	0	0	1	elecromagnetic
$W^{\pm}$	80.0 [5]	± 1	1	weak
Z°	91.18 [6]	0	1	weak

Table 1.1 The properties of the gauge bosons in the Standard Model.

By rewriting the Lagrangian of the electroweak interaction with the above three mass eigenstates, it can be shown that the photon couples to the electromagnetic

current and $W^{\pm}$ couples to the charged current of left-handed fermions (or right-handed antifermions) and Z° couples to the neutral current of left- and right-handed fermions.

The left- (right-) handed fermion state is defined when the spin direction of a fermion is opposite (parallel) to the momentum direction. The left- and right-handed fermion states are doublets and singlets under the weak isospin group, respectively. Fermions, which are pointlike spin one-half particles called leptons and quarks, are grouped into three generations:

				I_3
Leptons :	$\begin{pmatrix}\nu_e \\ e\end{pmatrix}_L$	$\begin{pmatrix}\nu_\mu \\ \mu\end{pmatrix}_L$	$\begin{pmatrix}\nu_\tau \\ \tau\end{pmatrix}_L$	$\begin{matrix}1/2 \\ -1/2\end{matrix}$
	$(e)_R$	$(\mu)_R$	$(\tau)_R$	0

Since neutrinos are assumed to be massless, there are no right-handed neutrinos.

				I_3
Quarks :	$\begin{pmatrix}u \\ d\end{pmatrix}_L$	$\begin{pmatrix}c \\ s\end{pmatrix}_L$	$\begin{pmatrix}t \\ b\end{pmatrix}_L$	$\begin{matrix}1/2 \\ -1/2\end{matrix}$
	$(u)_R$	$(c)_R$	$(t)_R$	0
	$(d)_R$	$(s)_R$	$(d)_R$	0

The three electrically charged leptons are called the electron, muon and tau, while the three neutral leptons are called the electron neutrino, muon neutrino and tau neutrino. The six quarks consist of up, down, charm, strange, top and bottom quark.

The top quark has not been discovered yet, but its existence is known from the measurement of the non-zero forward-backward asymmetry in the $b\bar{b}$ final state (A_{FB}^{b}) [7] and the cancellation of triangle anomalies which says that the number of quarks should be the same as the number of the leptons [8]. In addition, if the b quark is a singlet, then flavor changing neutral current decays of B mesons will appear [9]. An upper limit of $\mathrm{Br}(B \rightarrow \ell^{+}\ell^{-}X) < 0.0024$ supports the evidence that the b quark is a member of a weak isospin doublet [10].

The neutral current can couple to both the left- and right-handed fermions. The left- and right-handed couplings of a fermion to the Z° boson are defined as follows:

$$\begin{aligned} L_f &= I_3^f - Q^f \sin^2\theta_w \\ R_f &= -\ Q^f \sin^2\theta_w \end{aligned} \tag{6}$$

The vector and axial vector couplings of a fermion are defined as the sum and difference of the left- and right-handed couplings:

$$\begin{aligned} v_f &= L_f + R_f \\ a_f &= L_f - R_f \end{aligned} \tag{7}$$

Table 1.2 shows the values of electric charges, third components of the weak isospin, and vector and axial vector couplings of the fundamental fermions.

The massless photon, the three fermion generations, and the weak isospin doublet of the scalar Higgs particle are essential constituents in the minimal Standard Model. There are 21 empirical parameters in the minimal Standard Model. The $SU(2)$ coupling constant (g), the $U(1)$ coupling constant (g') and a vacuum expectation value of the Higgs field ($\langle\phi\rangle$), are the three parameters needed to determine electroweak dynamics.

fermions	Q_f	I_3	a_f	v_f
e, μ, τ	-1	$-1/2$	$-1/2$	$-1/2 + 2\sin^2\theta_w$
ν_e, ν_μ, ν_τ	0	$1/2$	$1/2$	$1/2$
u, c, t	$2/3$	$1/2$	$1/2$	$1/2 - 4/3\sin^2\theta_w$
d, s, b	$-1/3$	$-1/2$	$-1/2$	$-1/2 + 2/3\sin^2\theta_w$

Table 1.2 The electroweak properties of fermions.

The fine structure constant (α), the Fermi coupling constant (G_F), and the mass of Z° gauge boson (M_Z) are related to g, g', and $\langle\phi\rangle$ at the lowest order of perturbation (tree-level) calculation via the following relationships:

$$\alpha = \frac{1}{4\pi}\frac{g^2 g'^2}{g^2 + g'^2} \tag{8}$$

$$G_F = \frac{\sqrt{2}}{4}\frac{1}{\langle\phi\rangle^2} \tag{9}$$

$$M_Z = \langle\phi\rangle\sqrt{\frac{g^2 + g'^2}{2}} \tag{10}$$

α and G_F are well measured by the electron charge from Thomson scattering at $q^2 = 0$ and by the muon lifetime, after extracting specific purely electromagnetic radiative corrections [11], respectively. M_Z is accurately measured (91.187 ± 0.007 GeV) from the Z° line shape [12].

These three relationships are only valid at tree-level, and precise measurements of the three parameters are not enough to constrain the Standard Model. We must take account of virtual electroweak corrections in order to provide the precise values of the electroweak parameters, and additional electroweak measurements will serve as constraints to test physics beyond the Standard Model.

Since the left-right cross section asymmetry (A_{LR}) has a direct relationship with the vector and axial vector couplings, the precise measurement of A_{LR} can serve as an additional electroweak measurement to test the Standard Model. Since A_{LR} is also sensitive to electroweak corrections, it serves to constrain the masses of the top quark, the Higgs particle, or other new physics because the virtual electroweak radiative corrections depend on the masses of the top quark and the Higgs particle in the minimal Standard Model.

This thesis describes an A_{LR} measurement using the SLAC Large Detector (SLD) at the polarized SLAC Linear Collider (SLC). In Chapter 2, descriptions of the polarized SLC and the components of the SLD are presented. One of the main features of the SLC which is crucial to this analysis is a longitudinally polarized electron beam. A description of how the longitudinally polarized electron beam is produced and measured is included in this chapter. In Chapter 3, descriptions of the event selection and background estimation for hadronic Z° or tau pair events are presented. In Chapter 4 a measurement of the longitudinal electron beam polarization by the Compton polarimeter is described. In Chapter 5 final results, systematic errors, and future prospects of A_{LR} measurement at the SLC are described. In the final Chapter, the 1993 event selection procedures for hadronic Z°, and studies for improving the 1992 event selection, including tracking assisted event selection, are presented.

Theory

The fermion pair final state in the electron and positron annihilation process occurs via photon (γ) and Z° boson exchange. The lowest order Feynman diagrams of $e^+e^- \rightarrow f\bar{f}$ are shown in Figure 1.1. The differential cross section is then proportional to the square of the sum of amplitudes of the invariant matrices for the photon and Z° exchanges.

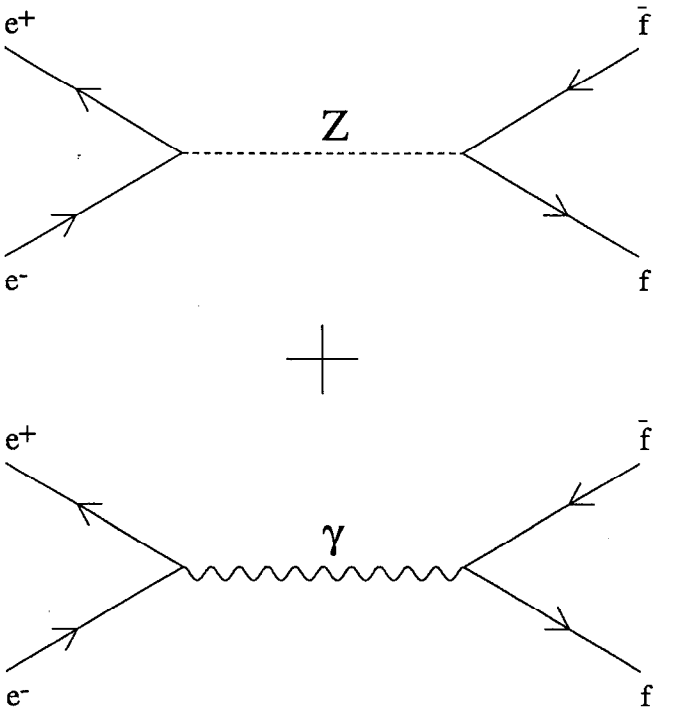

Figure 1.1 The Feynman diagrams of photon and Z° exchange in $e^+e^- \rightarrow f\bar{f}$ at tree-level.

$$\frac{d\sigma}{d\Omega} \propto |\mathcal{M}_\gamma + \mathcal{M}_{Z^\circ}|^2 \tag{11}$$

At the Z° pole ($s = M_Z^2$) the photon (pure QED) contribution is about 10^{-3} of the Z° contribution and is negligible, while the interference term ($\mathcal{M}_{\gamma Z^\circ}$) is zero. The contribution (pure weak) from the Z° is completely dominant at the Z° pole.

The differential cross section for a massless fermion, f, in $e^+e^- \rightarrow f\bar{f}$ at the

Z° pole with a longitudinally polarized electron beam is given by the following expression:

$$\frac{d\sigma}{d\cos\theta} = 2\sigma_\circ(v_e^2 + a_e^2)(v_f^2 + a_f^2)[(1 - \mathcal{P}A_e)(1 + \cos^2\theta) - 2A_f(\mathcal{P} - A_e)\cos\theta] \tag{12}$$

where θ is the angle between incoming fermion (e^-) and outgoing fermion (f), and v_f and a_f are the vector and axial vector couplings of a fermion f to the Z°, and $\mathcal{P}$ is the longitudinal polarization of the electron beam and is positive (negative) for the left- (right-) handed polarized electron beam. $\sigma_\circ$ and A_f are defined as follows:

$$\sigma_\circ = \frac{\pi\alpha^2}{4\Gamma_Z^2 \sin^4(2\theta_w)} \tag{13}$$

$$A_f = \frac{2v_f a_f}{(v_f^2 + a_f^2)}, \tag{14}$$

where:

$$\Gamma_Z = \frac{G_F M_Z^3}{24\pi\sqrt{2}} \sum_f N_c[1 + \frac{3\alpha {Q_f}^2}{4\pi}]({v_f}^2 + {a_f}^2) \tag{15}$$

and N_c is the color factor: 3 for quarks and 1 for leptons.

A_{LR} is defined as the ratio of the difference of total production rates with the left- and right-handed electrons to total Z° production rate [13]. A_{LR} is then expressed by the following equation:

$$\begin{aligned} A_{LR} &= \frac{\int_{-\cos\theta}^{\cos\theta} \frac{d\sigma_L}{d\cos\theta} d\cos\theta - \int_{-\cos\theta}^{\cos\theta} \frac{d\sigma_R}{d\cos\theta} d\cos\theta}{\int_{-\cos\theta}^{\cos\theta} \frac{d\sigma_L}{d\cos\theta} d\cos\theta + \int_{-\cos\theta}^{\cos\theta} \frac{d\sigma_R}{d\cos\theta} d\cos\theta} \\ &= \frac{\sigma_L - \sigma_R}{\sigma_L + \sigma_R} \end{aligned} \tag{16}$$

where $\cos\theta$ is the limit of the detector acceptance and $\sigma_L(\sigma_R)$ is the cross section

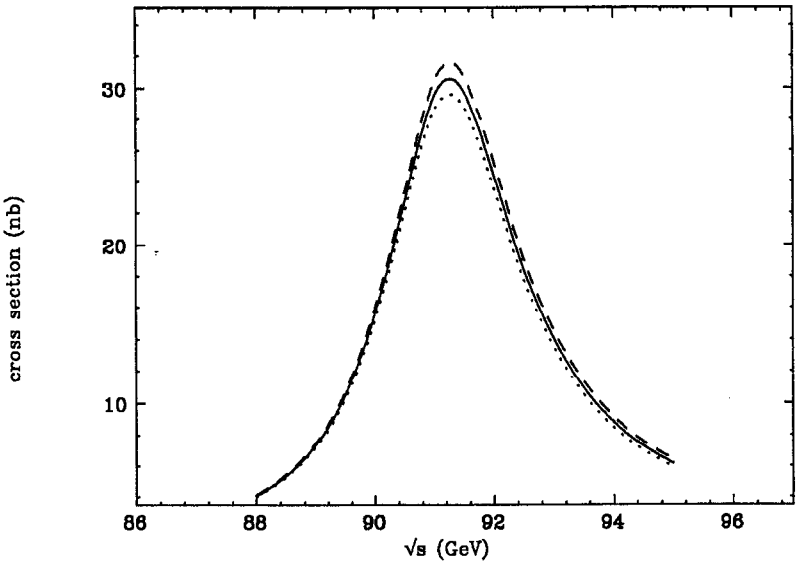

Figure 1.2 The cross section of $e^+e^- \rightarrow f\bar{f}$ versus the center-of-mass energy for 22% longitudinally polarized electron beam with 150 GeV top quark mass and 100 GeV Higgs mass. The solid curve is the cross section for unpolarized beam, the dotted curve is the cross section for $-$ 22% and the dashed curve is the cross section for $+$ 22% polarized electron beam.

of Z° production with the left- (right-) handed electrons.

Figure 1.2 shows the dependence of the total cross section of $e^+e^- \rightarrow f\bar{f}$ on the center-of-mass energy and the polarization of the electron beam. A ZSHAPE Monte Carlo [14], which takes care of initial state and final state QED corrections, one loop weak corrections and QCD corrections, is modified for the longitudinally polarized incident electron beam. The modified version of the ZSHAPE is used for this Figure. In the Figure the solid line is the cross section with unpolarized electron beam and the dots and dashed lines are the cross sections for the right- and left-handed polarized electron beams with 22% polarization, respectively.

With the differential cross section equation and the A_f definition, A_{LR} is given

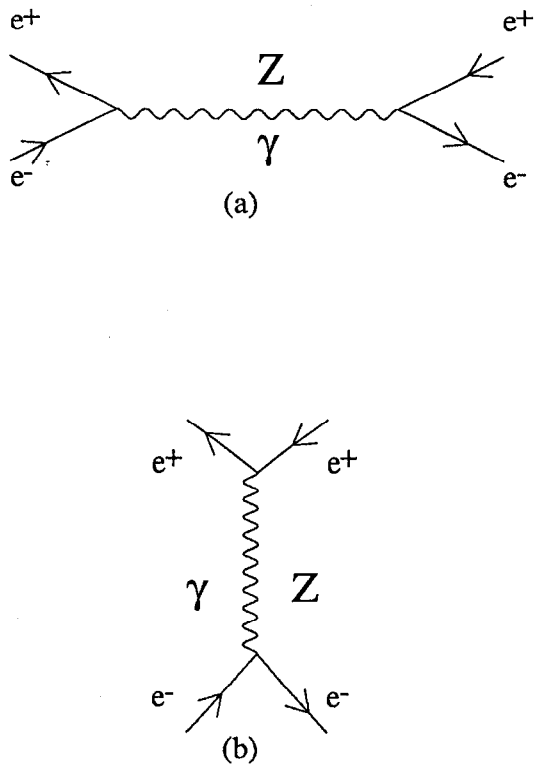

Figure 1.3 The Feynman diagrams of photon and Z° exchange in $e^+e^- \rightarrow e^+e^-$ at tree-level. (a) and (b) are the contributions from s and t channels, respectively.

by the following expression:

$$\begin{aligned} A_{LR} &= \frac{2v_e a_e}{v_e^2 + a_e^2} \\ &= A_e \end{aligned} \tag{17}$$

A_{LR} only depends on the initial state coupling of the electron to Z°. Therefore, it is insensitive to the final state radiation, and all visible final fermion states

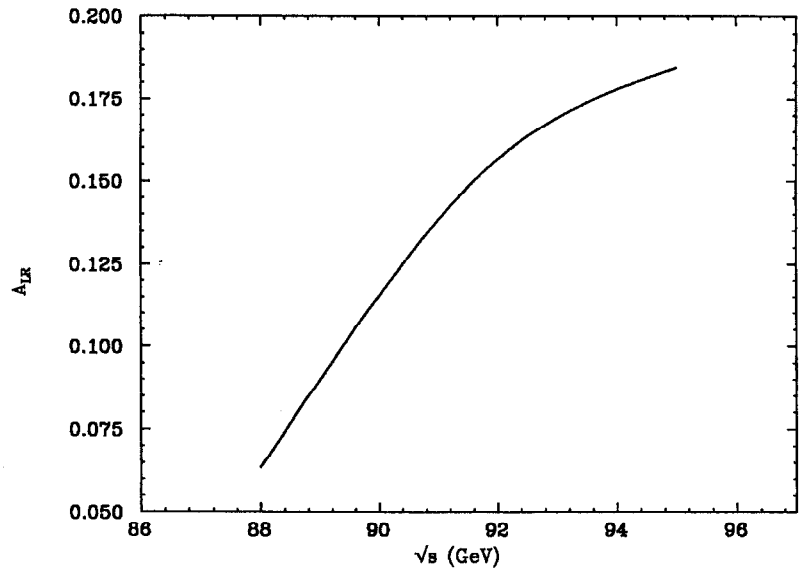

Figure 1.4 The A_{LR} versus the center-of-mass energy.

except e^+e^- can be used for the A_{LR} measurement. There is a t-channel scattering process contribution to the final electron-positron pair state, which dilutes A_{LR}; hence the e^+e^- final state is excluded. Figure 1.3 shows the Feynman diagrams for $e^+e^- \rightarrow e^+e^-$ via photon and Z° exchange. A_{LR} is independent of the final state acceptance and efficiency as long as the product of efficiency and acceptance of the fermion is the same as that for the antifermion.

Figure 1.4 shows the center-of-mass energy dependence of A_{LR}. It was assumed that the masses of the top quark and the Higgs particle are 150 and 100 GeV, respectively, with 22% polarized electron beam. A_{LR} changes by about 0.02 per GeV of the center-of-mass energy near the Z° mass. Thus, A_{LR} is quite insensitive to a small change in the center-of-mass energy. The effect of the initial state radiative corrections is, therefore, small. Since A_{LR} is insensitive to the center-of-mass energy, a several hundred MeV uncertainty in the measurement of the

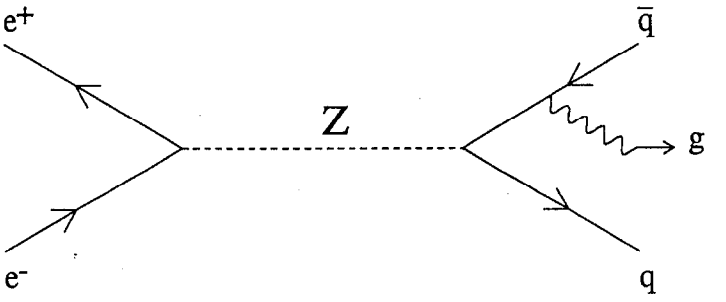

Figure 1.5 Final state gluon radiation in $e^+e^- \rightarrow q\bar{q}$.

center-of-mass energy is not a problem for the A_{LR} measurement.

There are QCD and electroweak corrections beyond the tree-level. Since A_{LR} is independent of the properties of the final state due to pure QCD corrections at the Z° pole, the effects of QCD corrections on the A_{LR} measurement vanish [15]. The largest QCD corrections occur from gluon radiation in the $q\bar{q}$ final states. Figure 1.5 shows final state radiation via gluon emission.

The electroweak corrections include the electromagnetic (QED) effects from the initial and final state photon radiation, and the weak corrections such as the oblique, vertex and box corrections. Figure 1.6 shows Feynman diagrams of the electroweak corrections.

Final state QED bremsstrahlung does not affect A_{LR} because it factorizes in the cross section. Most radiative corrections factorize and drop away in A_{LR}. The emission of real photons by the incident electron and positron causes a smearing of the center-of-mass energy of final fermion states. Since A_{LR} is quite insensitive to small changes in the center-of-mass energy, the effect of the initial state radiation is small and the size of the effect is calculated to be $\delta A_{LR} = 0.002$ [16]. This is small compared with the forward-backward asymmetry, which varies rapidly depending

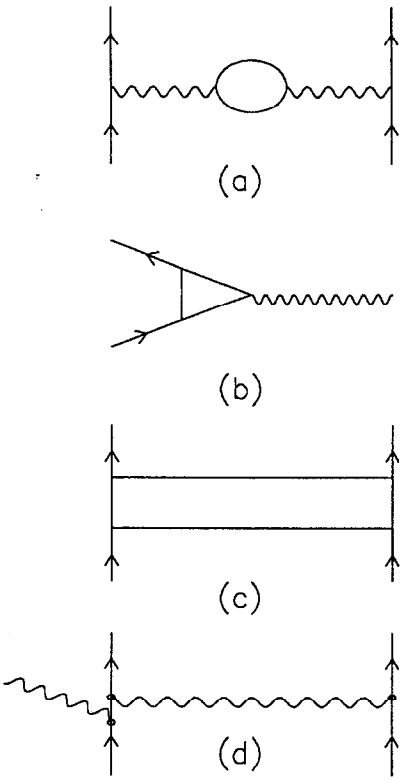

Figure 1.6 The electroweak corrections such as the oblique, vertex, box corrections, and bremsstrahlung amplitudes. (a) involves γ and Z°, (b) and (c) involve γ, $W^\pm$, and Z° and (d) involves γ.

on the center-of-mass energy around the Z° pole.

The effects of the vertex and box corrections are small and negligible [17]. The oblique corrections are important to new physics because of the presence of virtual loops in higher order calculations. These higher order effects are related to the top quark, Higgs particle, and other new physics processes, as well as the self interaction of the gauge fields. A_{LR} is very sensitive to these corrections and

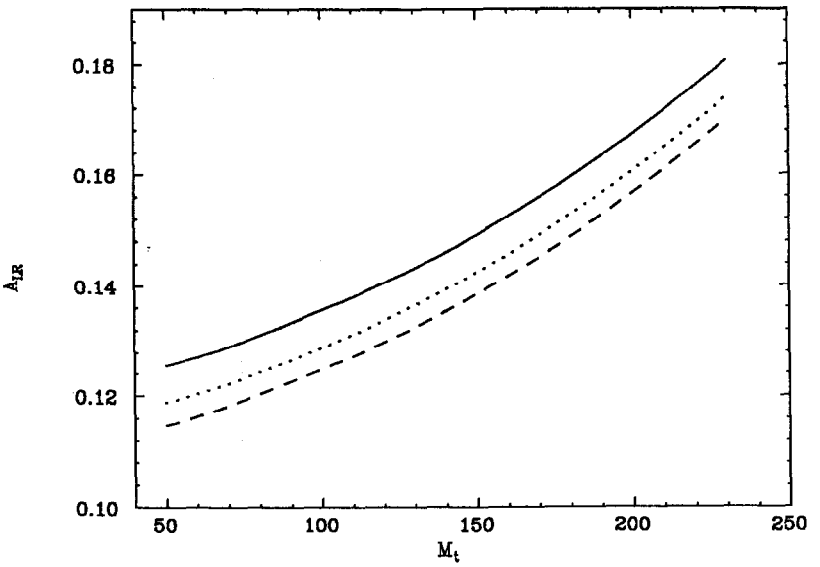

Figure 1.7 A_{LR} versus the top quark mass with different Higgs masses. The solid curve is for 100 GeV, the dotted curve is for 450 GeV, and the dashed curve is for 1000 GeV Higgs mass.

the correction term is proportional to the square of the top quark mass and to the logarithm of the mass of the Higgs particle in the minimal Standard Model [18]. Figure 1.7 shows the top quark mass dependence of A_{LR} for different Higgs masses. Since A_{LR} is affected by the mass of the top quark and the Higgs particle, its precise measurement will provide constraints on these masses.

The effective electroweak mixing angle, which takes account of the real parts of oblique corrections but ignores small corrections from imaginary parts of the oblique, vertex, and box corrections, is used. The effective electroweak mixing angle is defined as a combination of the electron vector and axial vector couplings:

$$\sin^2 \theta_w^{\text{eff}} = \frac{1}{4}(1 - \frac{v}{a}) \tag{18}$$

A_{LR} is then expressed in terms of the effective electroweak mixing angle for electrons:

$$A_{LR} = \frac{2(1 - 4\sin^2\theta_w^{\text{eff}})}{1 + (1 - 4\sin^2\theta_w^{\text{eff}})^2} \tag{19}$$

The precise measurement of A_{LR} provides an accurate value of the effective electroweak mixing angle. By comparing with other electroweak measurements the unknown radiative corrections can be probed and indications of new physics can arise from deviations between measurements.

The modified minimal subtraction scheme ($\overline{MS}$ – scheme) is one of the ways to calculate finite one-loop expressions [19]. There is a relation between the effective elecroweak mixing angle and the mixing angle defined in the $\overline{MS}$ – scheme $\sin^2\theta_w(M_Z)_{\overline{MS}}$, as follows [20]:

$$\sin^2\theta_w^{\text{eff}} = \sin^2\theta_w(M_Z)_{\overline{MS}} + 0.0006 \tag{20}$$

where the renormalized mixing angle is defined as follows:

$$\sin^2 2\theta_w(M_Z)_{\overline{MS}} = \frac{4\pi\alpha}{\sqrt{2}G_F M_Z^2(1 - \delta\hat{r})} \tag{21}$$

where the radiative correction term, $\delta\hat{r}$, is sensitive to the top quark and Higgs masses and a deviation is then an indicator of new physics beyond the minimal Standard Model.

Other asymmetry measurements can be made such as the forward-backward asymmetry, A_{FB}, and the forward-backward polarization asymmetry, $\tilde{A}_{FB}$. A_{FB} and $\tilde{A}_{FB}$ are defined, with the assumption of full polar-angle acceptance of the detector, as follows:

$$\begin{aligned} A_{FB} &= \frac{\sigma_F - \sigma_B}{\sigma_F + \sigma_B} \\ &= \frac{3}{4} A_e A_f \end{aligned} \tag{22}$$

where $\sigma_{F(B)}$ is the forward (backward) cross section. The forward (backward) is defined when $\cos\theta$ is positive (negative) with angle, θ, between incoming fermion (electron) and outgoing fermion:

$$\begin{aligned} \tilde{A}_{FB} &= \frac{(\sigma_F^L - \sigma_B^L) - (\sigma_F^R - \sigma_B^R)}{\sigma_F^L + \sigma_B^L + \sigma_F^R + \sigma_B^R} \\ &= -\frac{3}{4} A_f \end{aligned} \tag{23}$$

where $\sigma_{F(B)}^{L(R)}$ is the forward (backward) cross section with left- (right-) handed electrons. Since $A_{LR} = A_e$ and $A_e = 2v_e a_e/(v_e^2 + a_e^2)$, A_{LR} is 0.16 for $\sin^2\theta_w = 0.23$ at the tree-level. The numerical value of the asymmetry is relatively large compared with that of the A_{FB} measurement. Since $\tilde{A}_{FB}$ and A_{FB} depend on final state couplings, each fermion final state must be used separately, and an identification of the final fermion state is required.

The sensitivity of A_{LR} to the effective electroweak mixing angle is given by the following relation:

$$\frac{\delta A_{LR}}{\delta \sin^2\theta_w^{\text{eff}}} = 7.84 \tag{24}$$

A_{LR} is the electroweak parameter which is most sensitive to the electroweak mixing parameter, $\sin^2\theta_w^{\text{eff}}$, compared with other polarization-related measurements, $A_{FB}(\mathcal{P})$ and $\tilde{A}_{FB}(\mathcal{P})$ [21]. The sensitivity to the electroweak mixing angle of the tau polarization measurement, which is defined as $\bar{\mathcal{P}}_\tau = -A_\tau$ averaged over all

angles, is comparable to the A_{LR} measurement, but the branching ratio of the tau decay is about 3% of Z° decays.

Summary of Physics Motivation

The measurement of A_{LR} in Z° production with a longitudinally polarized electron beam is one of the unique measurements which can be done with the SLD at the SLC. The SLC began physics operation with longitudinally polarized electron beam in May of the 1992 and produced a sample of about 11,000 Z° events with a magnitude of polarization $\mathcal{P} \simeq 22\%$ in the 1992 run. This data was used for the measurements presented here. The SLC polarized electron beam provides, potentially, the most stringent test of the Standard Model of the electroweak interactions through the measurement of A_{LR}.

Since all visible Z° decay modes can be used for the A_{LR} measurement, except the e^+e^- final state, and A_{LR} is very sensitive measurement to $\sin^2\theta_w^{\rm eff}$, the measurent of A_{LR} is a beautiful test of the Standard Model. Since A_{LR} is, at present, the best observable for the large weak radiative corrections, the precise measurement of A_{LR} will provide information on the masses of the top quark and the Higgs, and beyond the Standard Model.

From the experimental point of view, the A_{LR} measurement is insensitive to small changes in the center-of-mass energy, QED radiative corrections, acceptance and efficiency. Since the measurement also does not require tagging and identification of specific final states, the A_{LR} measurement provides good systematics.

CHAPTER II

EXPERIMENTAL APPARATUS

Polarization at SLC

Introduction

In this chapter the SLC and the SLD are described. The SLC is located at the Stanford Linear Accelerator Center (SLAC), an e^+e^- collider, and was constructed for producing Z° particles at center-of-mass energy around 90 GeV for studying Z° physics.

Two electron bunches are produced from an electron source, the electron bunches are then injected into the north damping ring. After two electron bunches are extracted from this damping ring, the second electron bunch, which has reached 33 GeV at the 2/3 point of the linear accelerator (linac), is diverted by a kicker magnet to a positron target for producing positrons. The positrons produced are returned to the first linac sector by passing through a long return line. The electron and positron bunches are then co-accelerated to 1.21 GeV before being injected into the north and the south damping rings, respectively. When one positron bunch and two electron bunches are extracted from the damping rings, the SLC machine cycle begins.

Figure 2.1 shows a schematic layout of the polarized SLC [22]. The spin direction of the electrons is also shown from the polarized electron source to the SLC interaction point. After the positron and electron bunches are extracted from the first linac sector, they are co-accelerated and the beam energy reaches about 46 GeV at the end of the linac. The positron and electron beams are then sent to

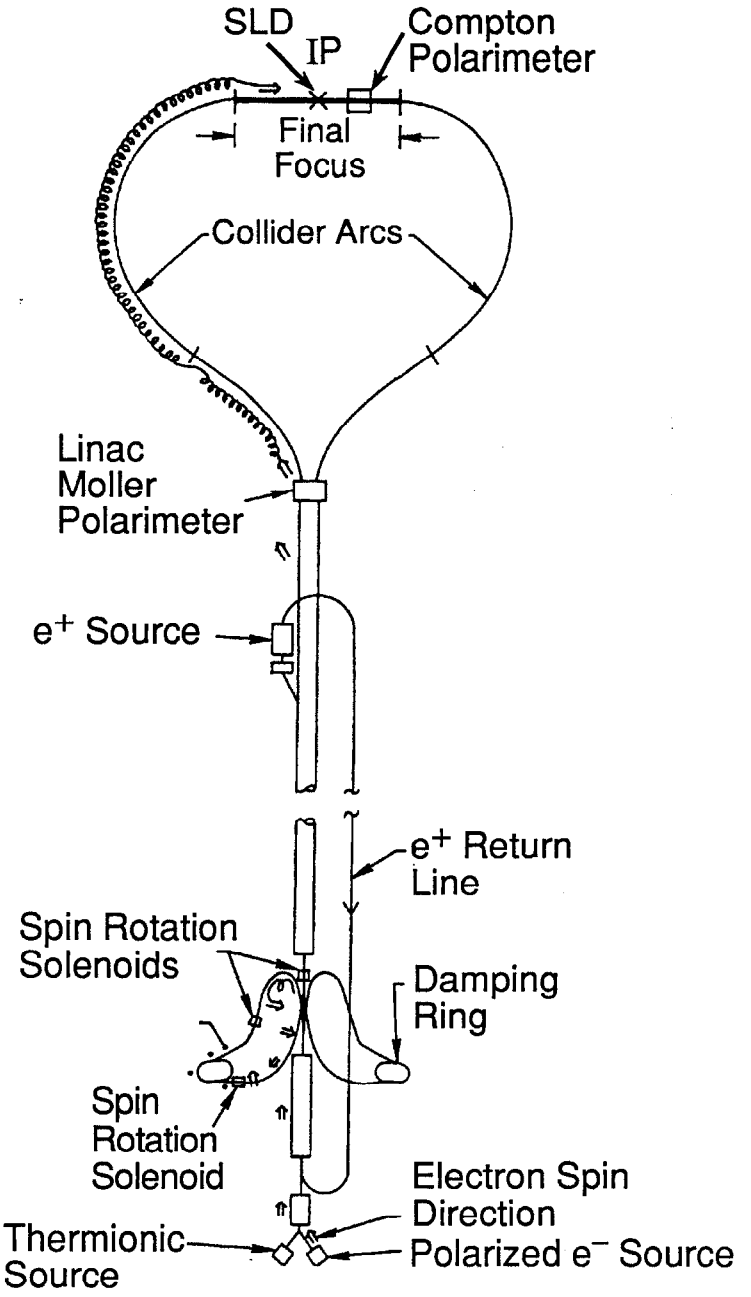

Figure 2.1 A schematic layout of the SLAC polarized Linear Collider. The direction of the electron spin vector is shown when the electron beam is delivered from the polarized electron source to the SLC interaction point.

the south and north arcs by a large dipole magnet. There is about 1 GeV energy loss due to the synchrotron radiation in the arcs. The final focus superconducting magnets are used for achieving a small beam size at the SLC interaction point.

There are a few main differences from the accelerator point of view between the SLC and Large Electron Positron (LEP) collider at CERN. The SLC is a linear collider which accelerates, collides, and discards the electron and positron beams after each collision. The SLC is a single-pass machine and provides a smaller beam size. LEP is a storage ring accelerator which stores the beams in its rings for collision and it provides a large repetition rate.

The luminosity is given by the following expression:

$$\mathcal{L} = \frac{N^+ N^- f}{4\pi\sigma_x\sigma_y} \tag{25}$$

where N^+ and N^- are the numbers of the positrons and electrons in each bunch, f is the collision repetition rate, and σ_x and σ_y are the horizontal and vertical beam sizes. Since the luminosity is inversely proportional to the beam size and is proportional to the repetition rate, the smaller beam size at the SLC compensates for the lower repetition rate. Another main feature of the SLC is that it can provide a longitudinally polarized electron beam, and this is the key to the study of the left-right cross section asymmetry (A_{LR}) in this dissertation.

The SLC was operated at a 120 H_Z repetition rate during the 1992 run with a longitudinally polarized electron beam. The typical beam intensity (N^-) was $\approx 3 \times 10^{10}$, the beam spot sizes ($\sigma_x \times \sigma_y$) were $\approx 2 \times 2\ \mu m^2$, and the average polarization of the electron beam was $\approx 22\%$. The integrated luminosity for the polarized 1992 run was 385 nb^{-1} [23]. The important features in the longitudinally polarized SLC are the polarized electron source system, the spin rotator system in the damping ring, the electron spin precession through the north arc and the

polarimetry.

Polarized Light and Electron Source

A polarized light source (PLS) at the SLC has to be capable of producing the required beam intensity and pulse structure. A flashlamp-pumped dye laser was used for the PLS, tuned to 715 nm of wavelength, and had 2.5 KW of power in the 1992 run.

A bulk gallium arsenide (GaAs) cathode was used for the polarized electron source at the SLC in the 1992 run [24]. When photons, which have slightly greater energy than the bandgap energy (E_g) of GaAs, illuminate the cathode, longitudinally polarized electrons are produced.

Figure 2.2 shows the band structure of GaAs and the allowed transition states for incident circularly polarized photons. When GaAs absorbs the circularly polarized laser light, the selection rules for angular momentum conservation require $\Delta m_j = +1$ and $\Delta m_j = -1$ for positive helicity ("right-handed") and negative helicity ("left-handed") circularly polarized photons, respectively. These transitions are shown as solid and dashed arrows in Figure 2.2.

If the energy, E_γ, of the right-handed circularly polarized photons are in the range $E_g \leq E_\gamma \leq E_g + \Delta$, the transition occurs from the $P_{3/2}$ state to the $S_{1/2}$ state. The transition rate of $(1, 3/2, -3/2) \rightarrow (0, 1/2, -1/2)$ is three times higher than that of $(1, 3/2, -1/2) \rightarrow (0, 1/2, +1/2)$ from the Clebsch-Gordon coefficients. The notation (n, m, m_j) is used, where n is the principal quantum number, m is the angular momentum quantum number and m_j is the third component of the angular momentum quantum number. Right-handed polarized electrons are then preferentially produced by right-handed circularly polarized laser light with a resulting polarization:

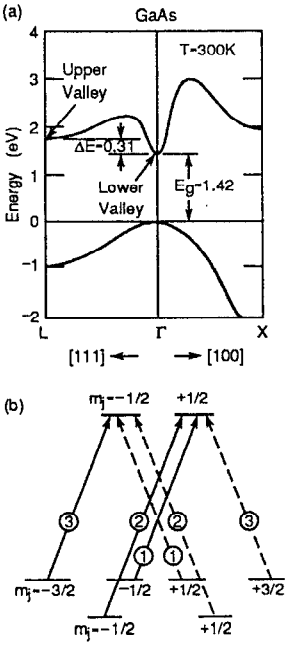

Figure 2.2 (a) is the band structure of GaAs. (b) shows energy levels of the state. Solid and dashed arrows show the allowed transitions after absorbing right- and left-handed circularly polarized photons, respectively.

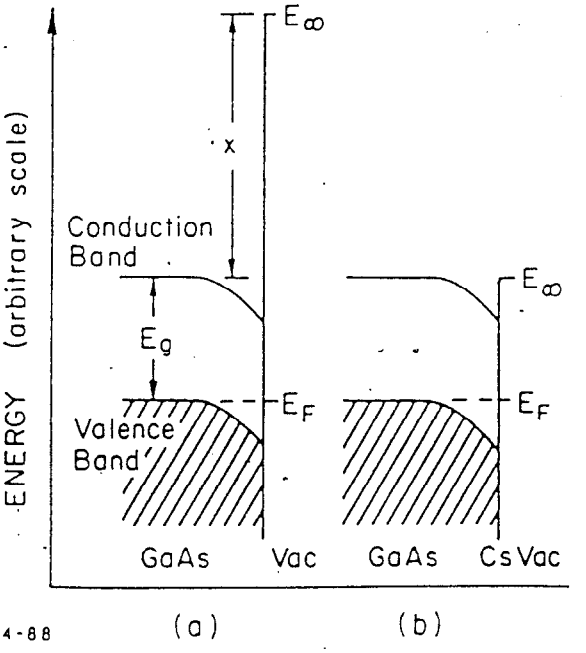

Figure 2.3 A negative work function is accomplished by deposition of a cesium-fluorine monolayer on the bulk GaAs photocathode surface. (a) is for pure GaAs and (b) is for the GaAs with the cesiated surface.

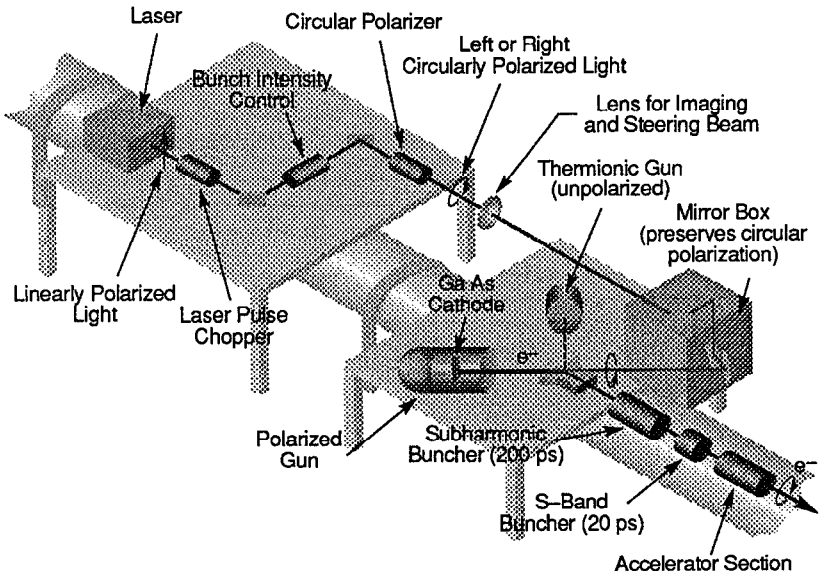

Figure 2.4 The polarized light source and electron source system.

$$\begin{aligned} \mathcal{P} &= \frac{3-1}{3+1} \\ &= 50\% \end{aligned} \tag{26}$$

The maximum theoretical electron polarization of the GaAs photocathode is then 50% in the case of 100% circularly polarized laser light.

For freeing the polarized electrons from the GaAs surface, a small energy gap between the conduction band and the free electron state is required for achieving high quantum efficiency. This is accomplished by the deposition of a cesium-fluorine (Cesium and NF_3) monolayer on the GaAs surface, which is called "cesiation". Figure 2.3 shows the result of cesiation on the GaAs surface. The negative work function results from the cesiation and this provides a high quantum efficiency for the photoemission of the conduction band electrons.

Figure 2.4 shows a schematic of the hardware of the polarized light source and polarized electron source system at the SLC. After the dye laser produces

a 750 ns pulse, two 2 ns pulses with 60 ns separation are produced by the laser pulse chopper. The first 2 ns pulse is used for producing the electron bunch and the second for the positrons. A bunch intensity control system consisting of a Pockels cell is used to regulate the laser light intensity on the GaAs photocathode. The circular polarizer is used for producing circularly polarized light from initially linearly polarized light by using a quarter-wave plate. The helicities of the circular polarized light are controlled by a random number generator which randomly sets the sign of the quarter-wave high voltage at a 120 H_Z repetition rate. The positive and negative high voltage settings produce right-handed and left-handed circularly polarized light, respectively. After the circular polarizer, the laser light enters a 20 meters long vacuum transport line to the GaAs photocathode. There is a 6 meter focal length imaging lens about midway between the circular polarizer and the photocathode, and the lens is used for imaging and steering the laser beam to the photocathode. Four mirrors are used in the mirror box. Each pair of mirrors, which have 90° reflections and are rotated with respect to each other by 38°, preserves the circular polarization and another pair of mirrors is used for raising the light beam by 16.3 cm for steering the light to the photocathode.

The pulse energy of ≈ 5 μJ in each 2 ns pulse is delivered to the photocathode with 99% circular polarization [25]. About 6×10^{10} electrons per pulse (a peak current of 5 A) are produced from the bulk GaAs photocathode.

For smooth SLC running, the polarized light system was required to provide a quantum efficiency (Q.E.) of more than 3%. The Q.E. was typically between 3% and 13% with the dye laser and bulk GaAs in the 1992 run. Whenever the Q.E. dropped below 3%, the cesiation procedure was performed. It required, on average, 30 minutes every week. It required about four hours every two weeks to change the dye and flashlamp. A reactivation and heat treatment of the photocathode was done every month and it required about eight hours.

An important factor in the gun performance was the cooling of the photocathode to just above $0°C$. This provides a longer cathode lifetime and reduces the frequency of interventions needed for re-cesiation of the source. The polarized electron source operated quite well, delivering polarized electron beam to the SLC with over 95% of uptime efficiency. The SLC produced 28−29% polarized electron beam at the bulk GaAs photocathode electron source using the 715 nm dye laser in the 1992 run. This lower polarization than theoretical prediction is due to several reasons, one of which is spin relaxation in the photocathode.

Spin Transport System

To provide longitudinally polarized electron beam at the SLC interaction point at any center-of-mass energy, there is a spin rotator system consisting of three solenoid spin rotators near the north damping ring. The spin rotators are superconducting solenoidal magnets with absolute field integrals 6.34 T-m.

After the longitudinally polarized electron beams are produced from the electron source, they are accelerated through the linac and transfered to the north damping ring. The linac-to-ring (LTR) bend magnets and superconducting solenoid are used to rotate the electron spin from the longitudinal direction to the vertical direction for storing the electrons in the damping ring.

Spin motion of a particle in synchrotron orbit is given by the Thomas-BMT equation [26]. The electron spin motion can be written in the laboratory frame from the Thomas-BMT equation:

$$\frac{d\theta_S}{dt} = \frac{ge}{2\mathrm{m}\gamma}[\gamma(\vec{B}_\perp - \vec{v}\times\vec{E}) + \vec{B}_\parallel] - (\gamma-1)\frac{e\vec{B}_\perp}{\mathrm{m}\gamma} \qquad (27)$$

where g is the electron gyromagnetic ratio, γ is the Lorentz boost factor, and $B_\perp$ and $B_\parallel$ are the transverse and parallel components of the magnetic field relative

to the electron velocity. With no significant electric field and $\gamma \approx 10^5$ for the SLC energy, the above equation is written conveniently:

$$\frac{d\theta_S}{dt} = [1 + \gamma\frac{g-2}{2}]\frac{e\vec{B}_\perp}{m\gamma} \tag{28}$$

The spin precession of the electron passing through a uniform magnetic field is then given by the momentum rotation θ_{bend}:

$$\theta_S = [1 + \gamma\frac{g-2}{2}]\theta_{bend} \tag{29}$$

For the damping ring design operating energy of 1.21 GeV, the coefficient is about 2.74.

When the electron bunch arrives at the entrance to the LTR transfer line with 1.21 GeV energy, the spin of the electron precesses by 90° for each 32.8° which the electron trajectories are bent by the transverse magnetic field. The 6.34 T-m superconducting solenoid, which is located after the bend of $5 \times 32.8°$ $(5\pi/2)$, rotates the spin of the electrons parallel to the magnetic field of the north damping ring magnets. Figure 2.5 shows the schematic layout of the north damping ring with the electron spin direction and magnetic fields of the north damping ring.

Another solenoid is in the ring-to-linac (RTL) transport and is located very close to the exit of the north damping ring for re-establishing the longitudinal direction from the vertical direction of the electron spin. The RTL rotates the spin from the horizontal to the longitudinal direction by a subsequent bend of $3 \times 32.8°$ $(3\pi/2)$.

The third solenoid is located in the linac line just after the beam bunches are injected into the linac. This spin rotator is used to provide longitudinally polarized electron beam at any center-of-mass energy at the SLC interaction point. The

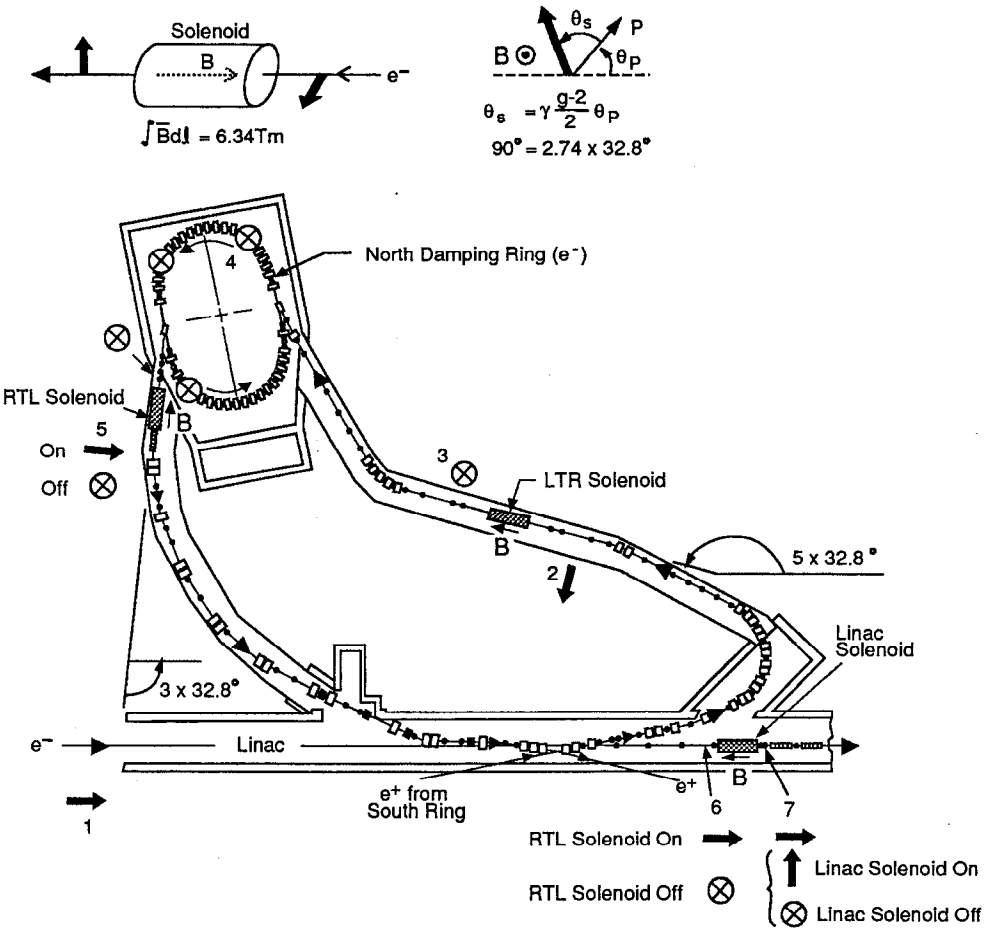

Figure 2.5 A schematic layout of the north damping ring. The arrow shown is the electron spin direction.

combination of the two solenoids and the RTL bending magnets allows arbitary spin orientation. Only the LTR and the RTL solenoids were used in the 1992 polarized run.

After the electron bunch is sent to the north arc by the dipole magnet, the electron spin undergoes a total of 236° of bend and a total of 70 spin precessions. For predicting the proper spin rotator settings to maximize the magnitude of longitudinal polarization at the SLC interaction point, the measurement of the longitudinal component of the beam polarization is used for each of three orthogonal spin direc-

tions at the end of the linac. Figure 2.6 shows the longitudinal beam polarization as a function of the electron beam energy. There are phase and period shifts in the longitudinal polarization component not predicted by the spin transport simulation. It shows that the maximum longitudinal polarization is near the Z° mass and that the proper spin rotator settings can be achieved from this measurement.

There are 23 achromats in the arc and the betatron phase advance of the SLC achromat is 1080° but the spin precession through the achromat is 1085°. Each of the achromats consists of 20 combined function magnets. Depending on the relative phases of spin and betatron oscillation, either the initial horizontal or longitudinal spin component will couple into the vertical. The electrons in the arc do not travel in ideal circular orbits for many different reasons, but the electrons wander in and out from the circular path and this transverse oscillation is called the betatron oscillation. Even though the coupling effect is small in each achromat, the cumulative effect is large enough due to the 23 achromats. Figure 2.7 shows the dramatic indication of this coupling as the launch of the electron beam into the arc varies. It shows that small changes in the launch position (Y_{pos}) or angle (Y_{ang}) produce big changes in the electron beam polarization near the SLC interaction point. It turned out that the betatron effect, which was not expected, is one of the main depolarization effects for the 1992 polarized run. After the collision, the electron beam is transported to the south final focus region where the Compton polarimeter is located for the measurement of the electron beam polarization.

Polarimetry

There are two polarimeters in the polarized SLC for monitoring and measuring the electron beam polarization. One is called the Moller polarimeter and the other is called the Compton polarimeter.

Figure 2.8 shows the location of these two polarimeters at the SLC. The Moller

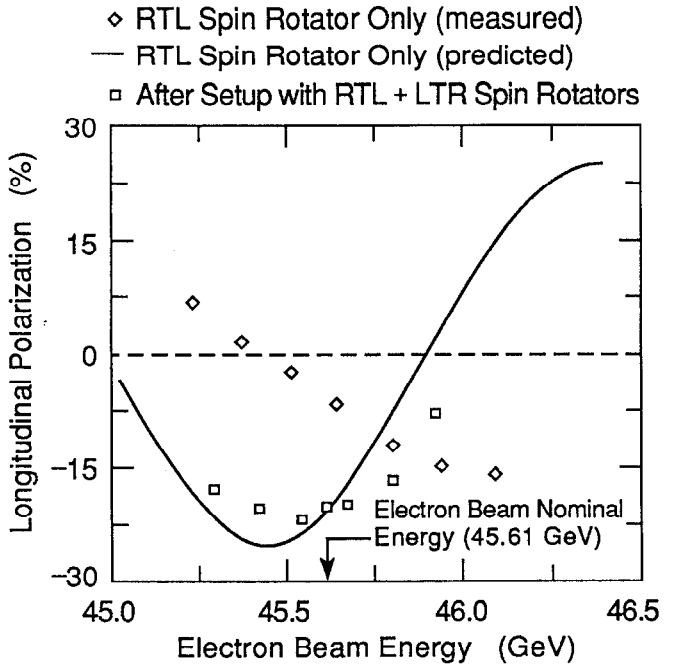

Figure 2.6 The electron beam polarization measurement with Compton polarimeter as a function of the electron beam energy.

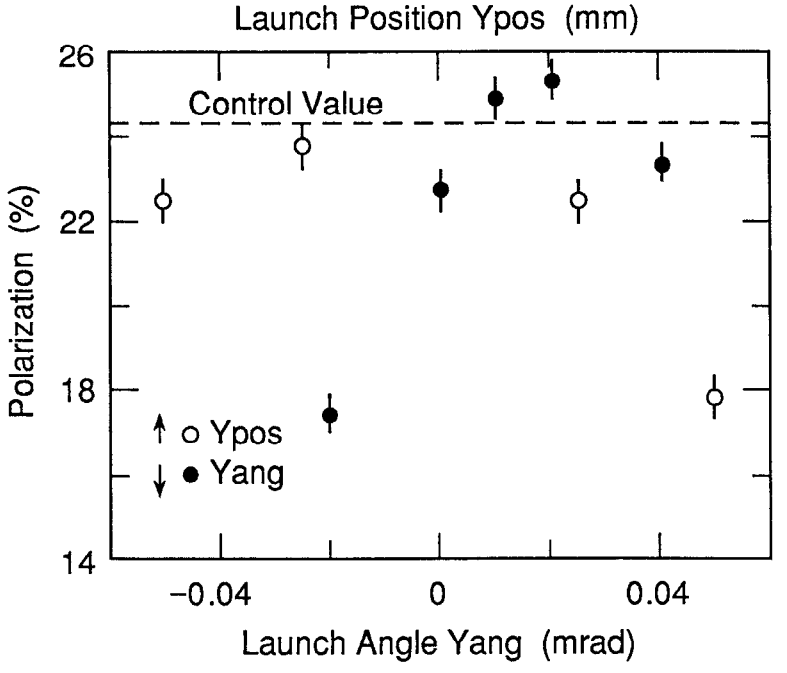

Figure 2.7 The betatron effect on the beam polarization in the arc due to the SLC achromats.

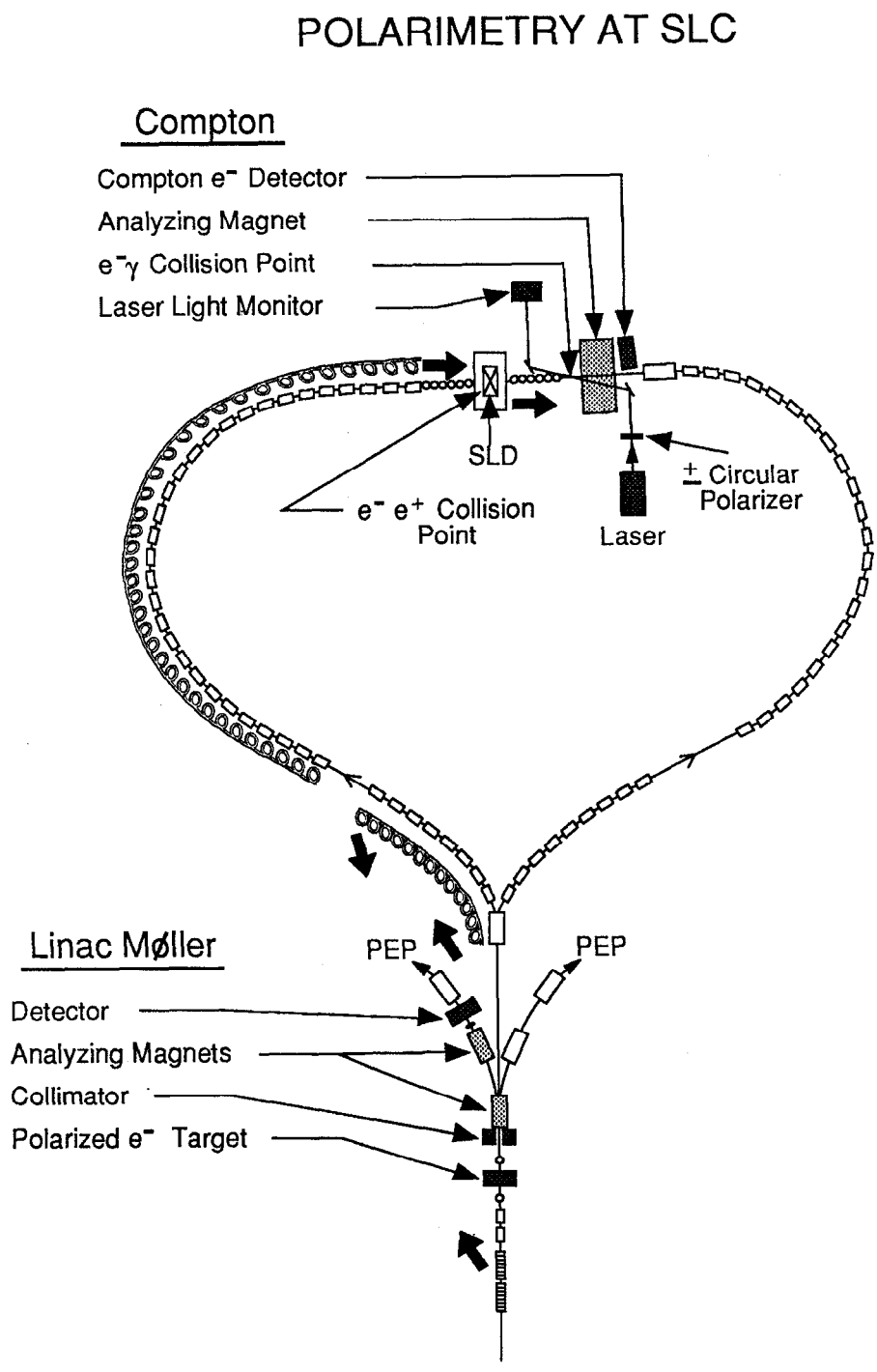

Figure 2.8 The Moller and Compton polarimeters are located at the end of the linac and near the SLC interaction point, respectively.

polarimeter is based on doubly polarized electron scattering and is located at the end of the linac for monitoring the electron beam polarization. The Compton polarimeter is based on doubly polarized electron and photon scattering and is located in the south final focus region.

The Moller Polarimeter

The Moller polarimeter is used for monitoring the electron beam polarization and checking depolarization sources. It is located at the end of the linac in the PEP extraction line.

The polarimeter measures all three components of the polarization vector and serves as a diagnostic tool in tuning the polarization and defining the initial precession angle. The measured components can then be used to predict the proper spin rotator settings needed to achieve a fully longitudinal polarized beam at the SLC interaction point at any given center-of-mass energy.

It also provides an independent polarization measurement without transporting the electron beam to the SLC interaction point. There was a difference in magnitude of the electron beam polarization between the Moller and Compton polarimeters, one possible reason being the betatron effect in the north arc.

Figure 2.9 shows a schematic of the Moller polarimeter. A magnetized iron target is used and a collimator is used to define the scattering plane. The polarimeter is based on the measurement of the scattering cross section asymmetry of the polarized electron beams with the electrons in the iron foil target of 50.8 μm thickness. Since the target is inclined at 20° with respect to the incident polarized electron beam, the effective thickness of the target is actually 152 μm. For 3×10^{10} electrons in a bunch, about a total of 15 Moller electrons are scattered from the target. A well-segmented silicon strip detector detects scattered Moller electrons which have momentum in the range 14–15 GeV/c. The differential cross section

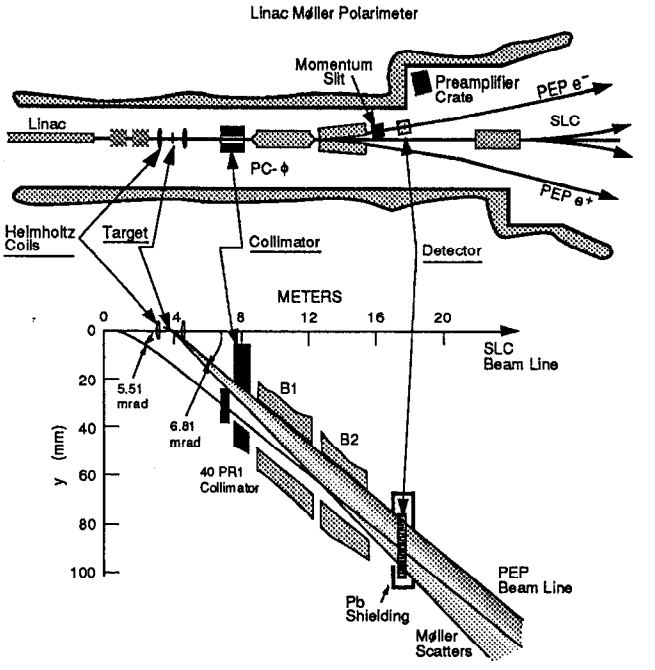

Figure 2.9 A schematic of the Moller polarimeter.

for Moller scattering has the following form:

$$\frac{d\sigma_p}{d\theta} = \frac{d\sigma_u}{d\theta}[1 - \mathcal{P}_z^{beam}\mathcal{P}_z^{target}A_z(\theta) - \mathcal{P}_t^{beam}\mathcal{P}_t^{target}A_t(\theta,\phi)] \qquad (30)$$

where σ_p and σ_u are the polarized and unpolarized Moller scattering cross sections, θ is the scattering angle in the center-of-mass frame, $\mathcal{P}_z^{beam}$ and $\mathcal{P}_t^{beam}$ are the longitudinal and tranverse polarizations of the incident electron beam, $\mathcal{P}_z^{target}$ and $\mathcal{P}_t^{target}$ are the longitudinal and tranverse polarizations of the target, and $A_z(\theta)$ and $A_t(\theta,\phi)$ are the longitudinal and transverse asymmetry functions.

The electron beam polarization at the polarimeter is measured from the asymmetry in the scattering rate of the polarized Moller scattering when the sign of the electron beam polarization is reversed:

$$\begin{aligned} \mathcal{P}_z^{beam} &= \frac{1}{\mathcal{P}_z^{target} A_z} \frac{[R(\mathcal{P}_z^{target}\mathcal{P}_z^{beam} > 0) - R(\mathcal{P}_z^{target}\mathcal{P}_z^{beam} < 0)]}{[R(\mathcal{P}_z^{target}\mathcal{P}_z^{beam} > 0) + R(\mathcal{P}_z^{target}\mathcal{P}_z^{beam} < 0)]} \\ &= \frac{A_{Moller}^{mea}}{\mathcal{P}_z^{target} A_z} \end{aligned} \tag{31}$$

The dominant systematic error in the incident electron beam polarization measurement at the polarimeter comes from the uncertainty of the target polarization measurement. In the 1992 polarized run the polarimeter measured $(29 \pm 1.25)\%$ polarization at the end of linac without passing the electron beam through the north damping ring.

The Compton Polarimeter

The Compton polarimeter is used for monitoring and measuring the magnitude of the electron beam polarization near the SLC interaction point. The polarimeter is based on Compton scattering of longitudinally polarized electrons with circularly polarized laser light [27].

A frequency-doubled Nd:Yag laser was used for providing the circularly polarized photons at the polarimeter. Figure 2.10 shows a schematic of the Compton light source. After the Compton laser light passes through a linear polarizer and the Pockels cell, which produces a $\lambda/4$ phase rotation, the absolute sign of the phase rotation is determined by comparision with a calibrated quarter-wave plate. The sign of the circular polarization is changed randomly on a pluse-to-pulse basis with 11 H_Z repetition rate for studying possible systematic effects. The laser beam is transmitted to the Compton scattering interaction point, which is located at 33 meters downstream from the SLC interaction point, within a vacuum transport system which consists of four phase-compensated pairs of mirrors, a focusing lens, and four vacuum windows. The outgoing electron beam and the photons cross at

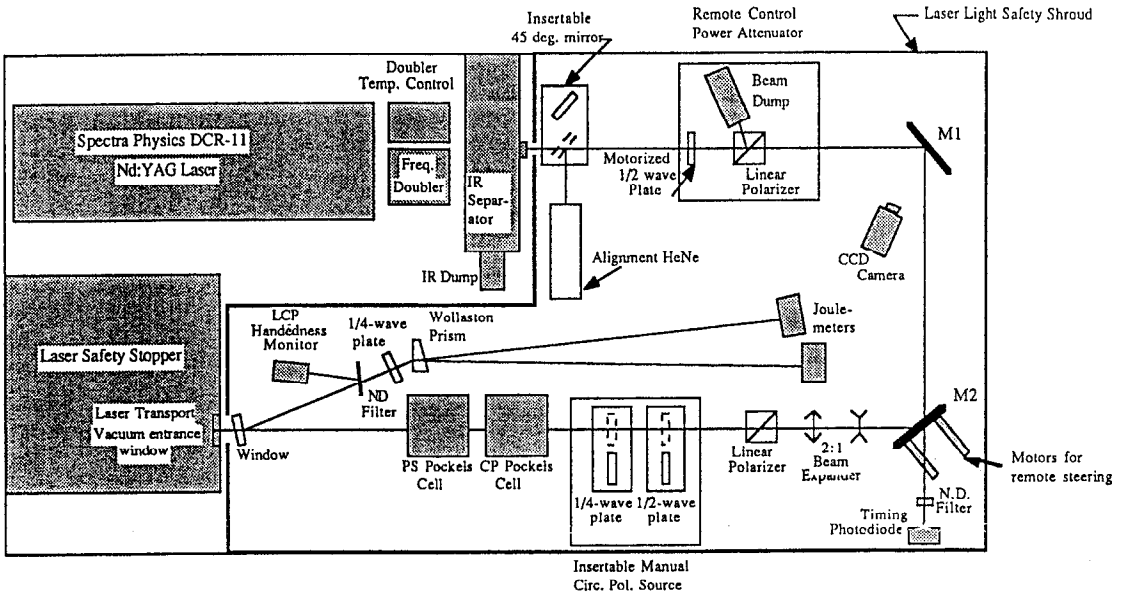

Figure 2.10 A schematic of the Compton light source.

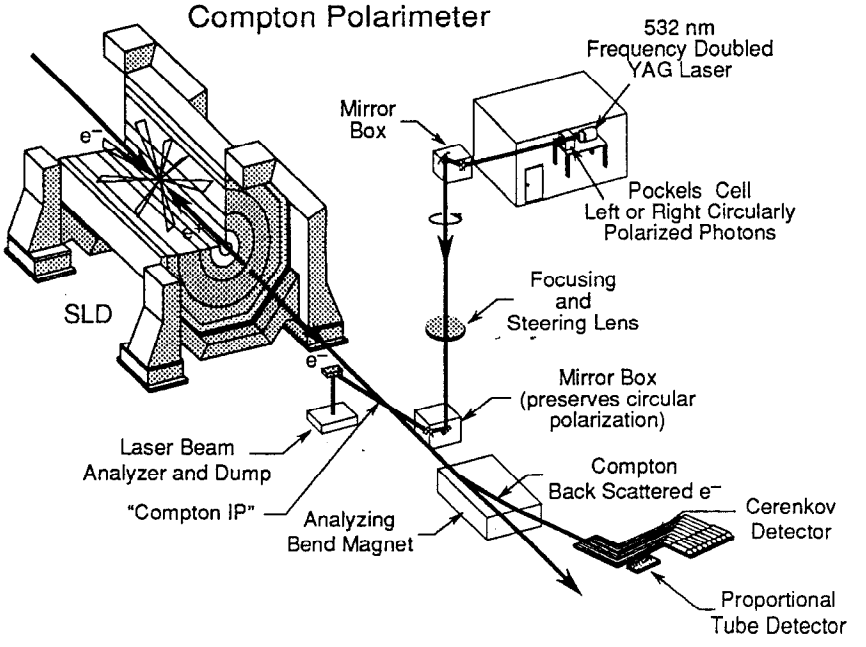

Figure 2.11 A schematic of the Compton polarimeter.

an angle of 10 milliradians and the approximate RMS transverse beam sizes are 350 μm for the electron beam and 750 μm for the photon beam.

The polarimeter measures the Compton electron scattering rate for the combinations of the two different helicity states of the electron and the two different helicity states of the photon. These combinations give two independent nonzero and two null asymmetries.

The circularly polarized photons, which have 2.33 eV energy, collide with the outgoing electron beam which has 45.7 GeV energy at 33 meters downstream of the SLC interaction point. Since the scattered electrons have a very small scattering angle, the scattered and unscattered electrons are only separated by a pair of analyzing dipole magnets which are used as electron momentum analyzers and have a 3.05 T-m field integral. After the electrons pass through the magnets, the scattered electrons are dispersed horizontally and exit the vaccum system through a thin window into a Čerenkov detector and a propotional tube detector (PTD). Figure 2.11 shows the polarimeter diagram and the two detectors.

The Čerenkov detector is located 3.57 m downstream of the effective bend center of the dipole pair which consists of magnets SB1 and B1. Since there are backgrounds due to low energy photons from synchrotron radiation and beam-gas interactions, the Čerenkov detector is used as a threshold device. Figure 2.12 shows the schematic layout of the Čerenkov detector and the PTD.

The Čerenkov detector has a retractable 1.4 radiation length plate of lead as the radiator, followed by a nine-channel threshold gas Čerenkov counter. Each channel is separated by aluminum walls of 0.025 cm thickness and has 1.00 cm width in the scattering plane for minimizing showering. Each $1 \times 1.5 \times 20$ cm^3 cell was filled with non-scintillating gas at a pressure of 1.0 atm and a Hamamatsu 1398 phototube was used for counting rates in the detector for different combinations of electron-photon spins. A 10 MeV energy threshold is applied for each channel

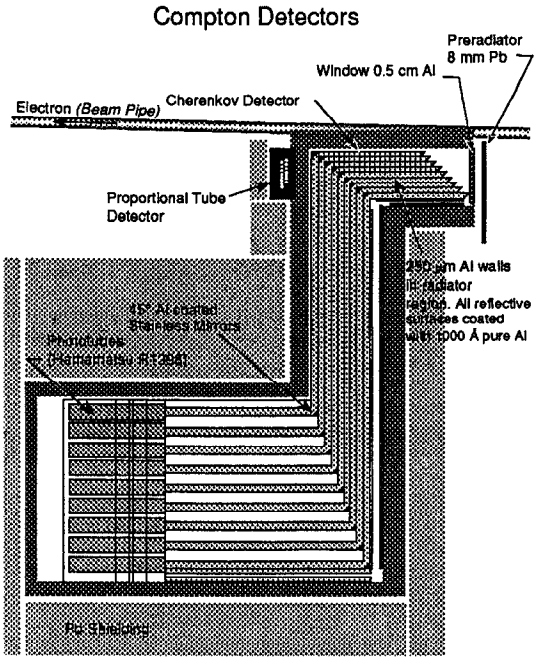

Figure 2.12 The Čerenkov detector and the proportional tube detector.

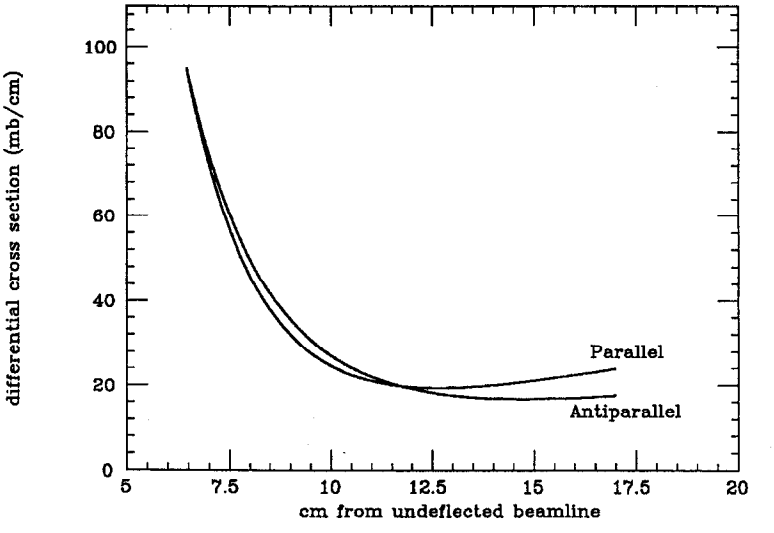

Figure 2.13 The Compton cross section for two different helicity combinations of the electron and Compton laser polarizations. The degree of the electron and photon polarization are assumed to be 22.4% and 93%, respectively.

for removing low energy photon backgrounds. The phototubes are operated at low gain ($\sim 10^5$) in order to ensure linear response. A Typical signal-to-noise ratio is 5−10, depending on the SLC's operating conditions.

Only the Čerenkov detector was used for the measurement of the electron beam polarization due to a calibration problem of the PTD in the 1992 polarized run. The scattered electrons of energies of 17−30 GeV are detected and the momenta are analysized by the bend magnet and position in the detector.

The differential cross section for the doubly polarized Compton scattering of the electron and photon is given by the following equation [28]:

$$\frac{d\sigma_p}{dE_s} = \frac{d\sigma_u}{dE_s}[1 + \mathcal{P}_\gamma \mathcal{P}_e A(E_s)] \tag{32}$$

where σ_p and σ_u are the polarized and unpolarized cross sections, E_s is the scattered electron energy, $\mathcal{P}_\gamma$ is the polarization of the photon, $\mathcal{P}_e$ is the electron beam polarization, and A(E_s) is the cross section ratio of parallel to anti-parallel electron-photon spins.

The unpolarized Compton scattering cross section and the Compton raw asymmetry depend on the energies of the electron beam and the photon. The largest cross section and asymmetry occurs for fully back-scattered electrons in the center-of-mass frame, which corresponds to a 17.4 GeV scattered electron energy in the lab frame. This locates the kinematic endpoint of the Compton spectrum at a distance of 16.97 cm from the undeflected beamline in the transverse direction. Since the distance in the beamline direction between the dipole magnet B1 and the Čerenkov detector is well-known, the B1 strength can be used as a calibration cross-check.

As the scattered electron energy is increased, the asymmetry is decreased. The asymmetry is zero for a scattered electron energy of 25.2 GeV and above this energy

the sign of the asymmetry changes to negative. The zero asymmetry corresponds to 11.71 cm of transverse distance from the undeflected beamline. Fig 2.13 shows the cross section of the parallel and anti-parallel electron-photon spins.

The magnitude of the electron beam polarization is obtained from the large asymmetry in the polarized Compton scattering cross section of Eq. (32). Eq. (32) can be usefully re-written in the following way:

$$\mathcal{P}_e = \frac{1}{\mathcal{P}_\gamma \alpha} \frac{[R(\mathcal{P}_\gamma \mathcal{P}_e > 0) - R(\mathcal{P}_\gamma \mathcal{P}_e < 0)]}{[R(\mathcal{P}_\gamma \mathcal{P}_e > 0) + R(\mathcal{P}_\gamma \mathcal{P}_e < 0)]} = \frac{A^{mea}_{compton}}{\mathcal{P}_\gamma \alpha} \tag{33}$$

where $A^{mea}_{compton}$ is the measured raw asymmetry of a Čerenkov detector channel and α is its analyzing power:

$$\alpha = \frac{\int A(E_s)\sigma(E_s)f(E_s)dE_s}{\int \sigma(E_s)f(E_s)dE_s} \tag{34}$$

where $f(E_s)$ is the channel response function for the scattered electron energy E_s and $\sigma(E_s)$ is the unpolarized differential Compton cross section.

The magnitude of the electron beam polarization can be extracted from a simple fit of Eq. (33) when the Čerenkov detector measures a rate asymmetry, $A^{mea}_{compton}$, and the photon polarization is known.

The second of the Compton polarimeter detectors is the PTD. The detector has 5 radiation lengths of a lead radiator and is instrumented with 16 proportional tubes of 3.9 mm diameter. The sensitive area of the detector is 60 mm by 6 mm in the horizontal and the vertical planes. The tubes are filled with a gas mixture composed of 89% argon, 10% carbon dioxide, and 1% methane. In order to maintain the linear response of the detector, the PTD like the Čerenkov detector, is operated at very low gain (50−100). A typical signal-to-noise ratio is 1−2, depending on the SLC's operating conditions.

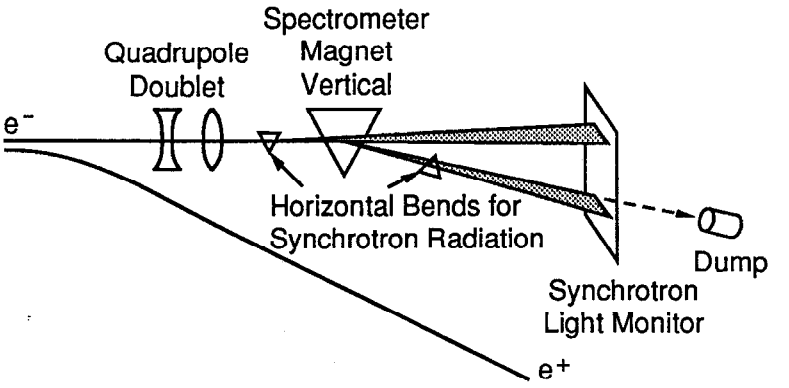

Figure 2.14 A schematic of the energy spectrometer for measurement of the center-of-mass energy at the SLC.

Energy Spectrometer

The beam energy needs to be measured accurately in order to constrain spin dynamics. The energy spectrometers in each extraction line measure the average energy of the particles in the positron and electron bunches after the positron and electron bunches pass through each other at the SLC interaction point and before they are dumped. A pair of wire imaging synchrotron radiation detectors (WISRD) are used for measuring the beam energies [29].

Figure 2.14 shows the schematic layout of the extraction line energy spectrometer. As the beam passes through three dipole magnets, the beam energy is extracted by measuring the distance between the two stripes of synchrotron radiation (d) with knowledge of the distance from the magnetic center of the spectrometer magnet to the WISRD wire arrays (L):

$$E_{beam} = (\frac{e}{c})(\frac{L}{d})\int B \cdot dl \tag{35}$$

where $\int B \cdot dl$ is about 3 T-m, L is about 15 m, and d is about 25 cm.

It is expected that systematic errors in the pulse-to-pulse measurement of the center-of-mass energy is 20 MeV.

Polarization Data Acquisition

There are redundant paths for synchronizing the measurement of the helicities of the electron beam polarization with the SLD data acquisition. One is called the Klystron Veto Module (KVM) polarization bit and the other is called the MACH line polarization bit. The KVM bits come from the sign of the high voltage on the Pockels cell on the polarized light source system while the MACH bits come from a SLD CAMAC crate directly.

The polarimeter run data are acquired for intervals of 20,000 machine pulses which corresponds to a 3 minute run and are logged to the SLD data tapes.

Overview of the SLD

Introduction

SLD is a detector to study Z° physics with e^+e^- collisions at SLAC [30]. The SLD is composed of a vertex detector for tracking of charged particles, a pair of tungsten/silicon calorimeters used as a luminosity monitor, a drift chamber system for high resolution momentum measurement of charged particles, a Čerenkov ring imaging detector for particle identification, a lead/liquid argon calorimeter for energy depositions of neutral and charged particles, and an iron limited-streamer tube calorimeter for muon tracking and continuation of hadron energy measurements.

One highlight of the SLD is the vertex detector (VXD) based on a precision charge coupled silicon device. The combination of the VXD and small beam size

of SLC result in effective secondary vertex tagging. Another advantage is the Čerenkov ring imaging detector (CRID) which potentially provides particle identification of charged particles.

Figure 2.15 shows a quadrant drawing of the SLD.

The Vertex Detector

The VXD is made of 480 charge coupled devices (CCDs) and has four concentric layers of CCDs [31]. The CCDs are pixel devices which provide two dimensional readout. The detector provides three dimensional information since the position of the CCDs is already known. Each CCD contains about 400×600 pixels and each pixel size is 22×22 μm^2. The active area of the CCD is then about 9×13 mm^2.

The radii of the four layers, called barrels, increase from 29.5 mm by 4 mm for each layer from the beam line. The inner and outer two barrels are composed of 13 and 17 ladders, respectively. Each ladder is 13.6 cm in length, and is composed of eight CCDs, of four on either side of the ladder to give total coverage of the ladder. Figure 2.16 shows a schematic layout of the VXD.

To minimize the multiple scattering, the detector has only 1.75% of a radiation length before the second hit in the VXD and 5.9% radiation lengths before the first hit in the central drift chamber.

The readout time of the detector is 160 ms, corresponding to about 19 beam crossings. When another trigger occurs during the readout of an event, the system continues reading for 19 beam crossings after that trigger. Since the *HADRON*, *TRACK*, and *RANDOM* triggers read the VXD data and the readout time of the central drift chamber is longer than that of the VXD, there is no deadtime due to the relatively slow readout time of the VXD.

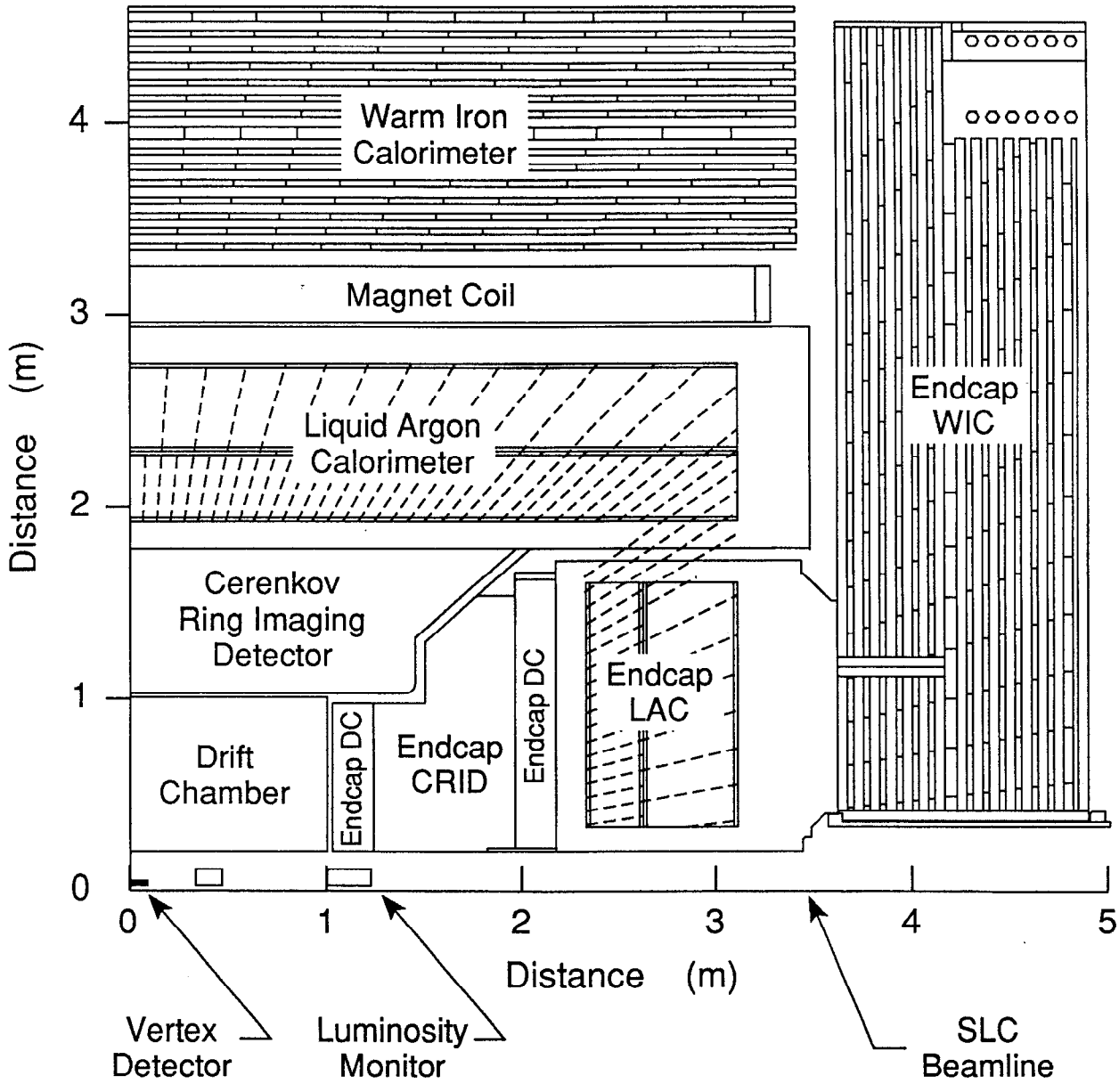

Figure 2.15 A quarter of the overall layout of the SLD detector.

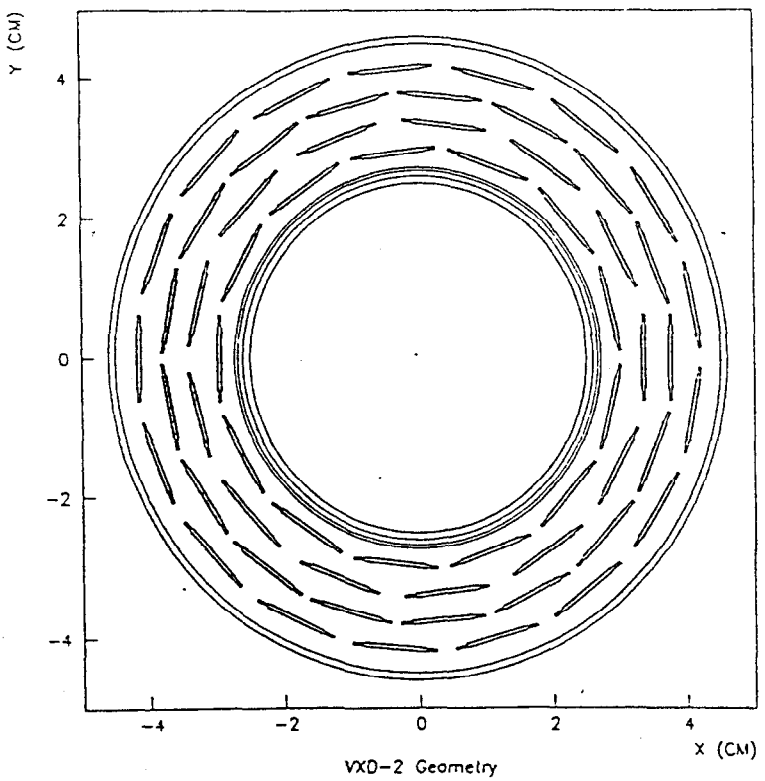

Figure 2.16 The charge coupled device vertex detector in the transverse plane.

The Luminosity Monitor

The luminosity monitor system consists of a luminosity monitor and small angle tagger (LMSAT) and a medium angle silicon calorimeter (MASC) [32]. The front faces of the two detectors are located at 1 m and 30 cm away from the SLC interaction point, respectively.

The luminosity monitors were designed to contain more than 99% of the energy of a small-angle Bhabha event. The luminosity monitor is very important for an accurate integrated luminosity measurement in order to provide precision measurements of Z^0 resonance parameters.

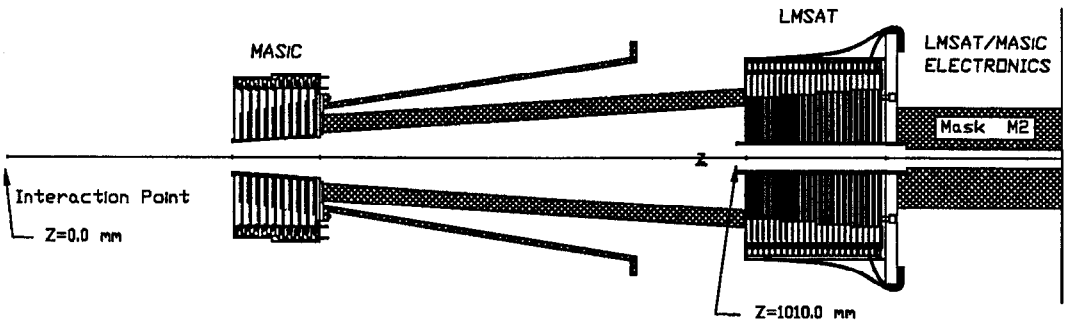

Figure 2.17 The luminosity monitor system which consists of a pair of luminosity monitor and small angle tagger (LMSAT) detectors and the medium angle silicon calorimeters (MASC).

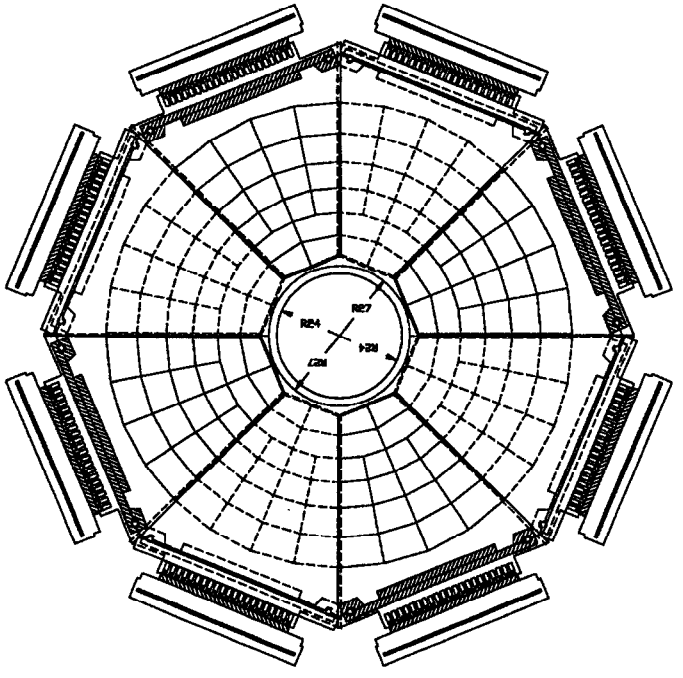

Figure 2.18 Well-segmented tower geometry of the LMSAT for providing good angular resolution.

The luminosity monitor system is divided into the LMSAT and the MASC for protecting the VXD from background radiations. The MASC shields the VXD from radiation which is rescattered into the central drift chamber system and is positioned to optimize this shielding effect.

Figure 2.17 shows the configuration of the MASC and LMSAT of the luminosity monitor system. The MASC and LMSAT are silicon sampling calorimeters with an alloy of tungsten as the radiator. For the MASC the radiator is an alloy of 95% tungsten and 5% copper, a total depth of 17 radiation lengths. For the LMSAT the radiator is an alloy of 90% tungsten, 6% copper and 4% nickel, a total depth of 22 radiation lengths. The LMSAT and MASC have 23 and 10 silicon layers, respectively, on each side of the SLC interaction point.

The LMSAT covers the angular range between 28 and 65 mrad and the MASC covers between 65 and 190 mrad. Since the differential cross section of the small-angle Bhabha process is large and rapidly changes at small angles (falling as $1/\theta^3$), the LMSAT is required to have excellent angular resolution. The LMSAT has a well-segmented tower geometry in the transverse plane for providing good angular resolution. Figure 2.18 shows the projective tower geometry of the LMSAT. The silicon pads in the LMSAT are segmented into 20 towers.

The LMSAT is mounted from the back on the support tube for the superconducting final focus (SCFF) quadrupoles and has two halves for easy disassembly and to provide easy access to the VXD.

The front-end electronics, called a "tophat", of the LMSAT and MASC are located behind the LMSAT. The LMSAT and MASC consist of a total of 640 and 384 electronic channels, respectively, and both of them have two readout electronics sections. The first section, which is composed of the first six layers, is called EM1 while the second section, which is composed of the last seventeen layers, is called EM2. There are two tophats for the luminosity monitor, one on each side of the

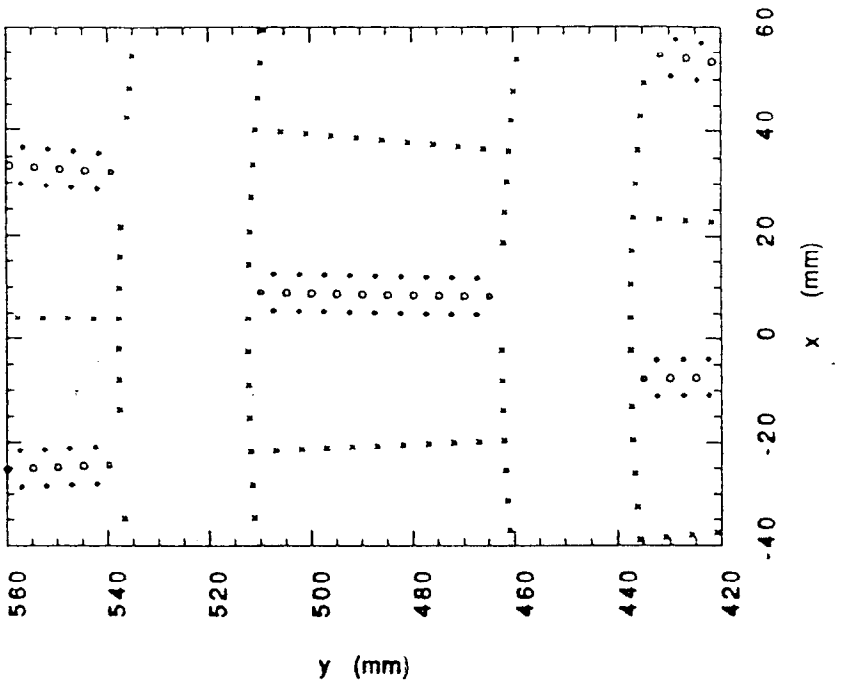

Figure 2.19 The layout of wires in a cell. The field, guard and sense wires are represented by the diagonal crosses, diamonds, and circles, respectively.

SLD. It is expected to have $20\%/\sqrt{E}$ energy resolution, and a spatial resolution of $\delta\theta = 0.4$ mrad and $\delta\phi = 6.5$ mrad.

The Drift Chamber

The drift chamber systems consist of a central drift chamber (CDC) and an endcap drift chamber (EDC). The CDC and EDC share common readout electronics, drift gas, and have a similar drift cell design.

The drift chamber systems provide the precise momentum measurement of charged particles by using a drift time, a drift velocity, and a drift distance of drifted electrons. The drift gas used is a mixture of 75% CO_2, 21% Ar, 4% C_4H_{10}(Isobutane) and 0.2% H_2O. The gas mixture has a low diffusion coefficient allowing for intrinsic spatial resolutions of $40-100$ μm depending on the drift distance within a cell. The gas mixture has an average drift velocity of about 10 μm/ns.

The CDC is cylindrical. It is 2 m long and extends from 20 to 100 cm in radius from the beam line. The CDC consists of 10 concentric superlayers of jet cells. Each layer is made of independent cells 6 cm wide by 3 cm long and each cell consists of 8 sense wires, 18 guard wires, and 36 field shaping wires. The guard and field shaping wires are used for charge amplification and electric field shaping.

Figure 2.19 shows the layout of wires in a cell. The guard, field shaping and two dummy sense wires are 150 μm gold-coated aluminum wire and the sense wires are 25 μm gold-coated tungsten. There are 28 cells in the innermost superlayer and the number of cells in each superlayer increases by 8 going outward, giving a total of 640 cells in the 10 CDC superlayers.

The 10 superlayers are arranged in four axial and six stero layers and the interlayer distance is 5 cm. The label "A" is for axial layers which are parallel to the beam line. The labels "U" and "V" are for stereo layers which have $\pm$ 40 mrad stereo angle with respect to the axial wires to provide the measurement of the z coordinate of charged tracks [33].

The EDC consists of four planar and circular modules, two of them located at the north and south side, respectively, to provide the tracking of charged particle from 10° to 40° in polar angle. In the angular range between 20° and 40° the CDC also detects charged particles. Each module consists of three superlayers rotated 120° from each other and each of these functions like a superlayer of the CDC. The rotated superlayers provide three dimensional tracking and each superlayer consists of many jet cells like that in the CDC.

The Čerenkov Ring Imaging Detector

When a charged particle of speed βc passes through a material which has refractive index n, it radiates light, called "Čerenkov radiation", when $\beta > 1/n$. The opening angle of the light cone is given by the following equation:

$$\cos\theta = \frac{c}{vn} \tag{36}$$

where v is the velocity of the charge particle, n is the refractive index of the material, and c is the speed of light.

The Čerenkov radiation is imaged into the drift box where Čerenkov rings are observed. Particle identification is performed by measuring the radius of the ring and the momentum of the charged particle from the CDC.

There are barrel and endcap Čerenkov detectors. The barrel detector provides particle identification over 70% of the solid angle [34].

A charged particle first passes through the liquid radiator composed of Freon (C_6F_{14}) with a refractive index of 1.277. The photons of the Čerenkov radiation then ionize the gas in the drift box and the ions are drifted to one end. When the anode wires receive the signals, the rings of the liquid radiator are reconstructed using the drift time, wire address and charge division (sharing of charge on the two ends of the wires).

The gas used in the time projection chamber (TPC) is a mixture of C_2H_6 (ethane) and Tetrakis Dimethyl Amino Ethylene ($TMAE$), which is sensitive to ultraviolet Čerenkov photons.

Beyond the drift box, a charged particle passes through a large volume gas radiator which is filled with gaseous Freon C_5F_{12} with a refractive index of 1.002. The photons of the Čerenkov radiation are sent back into the drift box by mirrors, and the rings of the gas radiator are reconstructed from the signals received on the wire plane at the end of the drift box. Figure 2.20 shows the two radiators and Čerenkov photons in the Čerenkov ring imaging detector barrel section. A π/K/p and e/π separation are possible up to 30 GeV/c and 6 GeV/c with the liquid and the gas radiator, respectively.

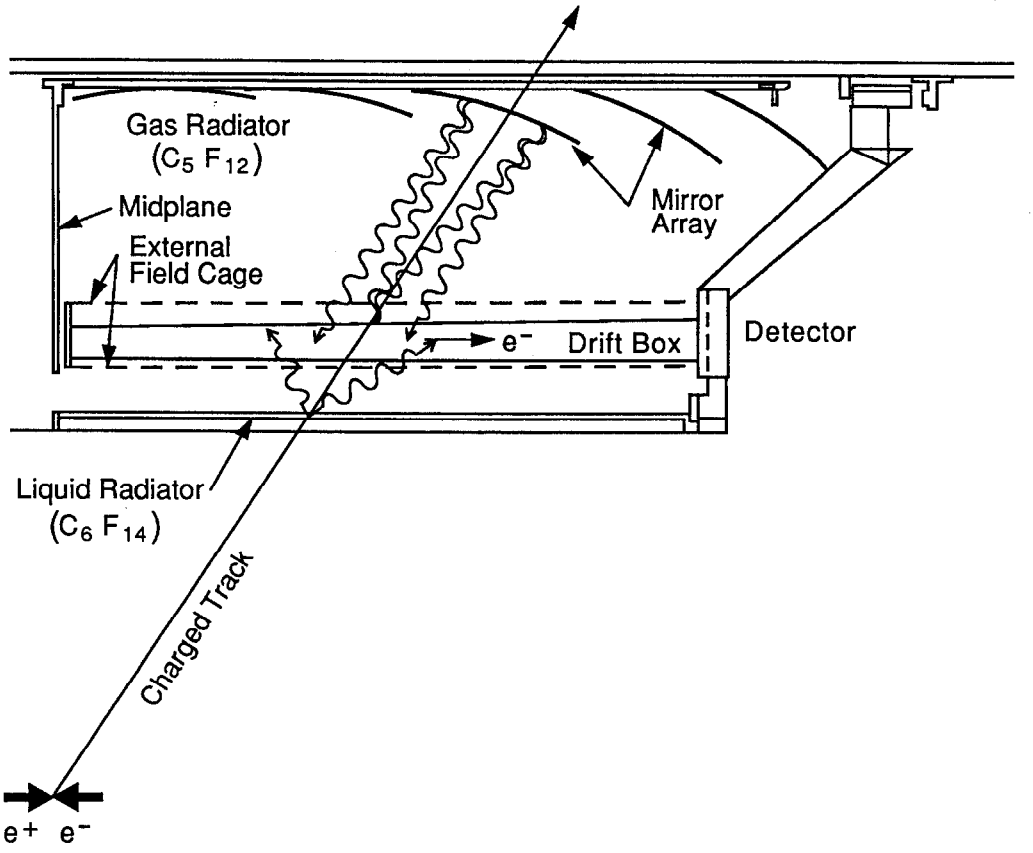

Figure 2.20 Schematic of the Čerenkov ring imaging detector barrel section which shows Čerenkov photons. There are two radiator devices. One is a liquid radiator which is a proximity focusing device and other is a gas radiator which is a ring imaging device with gas.

The Liquid Argon Calorimeter

The lead liquid argon sampling calorimeter (LAC) is a hermetic detector with good energy resolution and a uniform response for electrons and hadrons [35]. The LAC is located within the SLD solenoidal magnet which is 0.29 m thick and provides 0.65 Tesla of uniform magnetic field. The LAC also serves to support the

magnet and warm iron calorimeter.

The LAC consists of a cylindrical barrel and two endcap calorimeters and covers 98% of the full solid angle for both electromagnetic and hadronic showers. The cylindrical barrel LAC is 6 m long, and extends from 1.8 to 2.9 m in radius.

The lead material is used as an absorber/radiator for getting uniform response for electrons and hadrons ($e/h = 1$) and the LAC is composed of about 3 absorption lengths. The absorber consists of alternate planes of lead sheets and segmented lead tiles, and liquid argon is filled between the planes. The lead used for the plates and tiles is a "dispersion strengthened" alloy, containing 1.5% Sn (tin) and 0.06% Ca (calcium) since pure lead caused excessive sag in the long vertically oriented plates on the cryostat.

The thickness of the lead plates and tiles are 2 mm and 6 mm, respectively, with a gap between them of 2.75 mm. The lead tiles are held at a negative high voltage as charge collecting electrodes and are connected radially for making projective towers and for electronic readout.

The barrel LAC covers the angular region $35° \leq \theta \leq 145°$, where θ is the polar angle from the beamline. There are electromagnetic (EM) and hadronic (HAD) modules in the radial direction. There is a "center" and two "end" modules in the beamline direction. Modules are $\sim$ 2 m in length and are separated by washers. The center and end modules are only different in the size and layout of segmented towers. Figure 2.21 shows a schematic of the barrel calorimeter of the LAC. There are a total of 96 EM and HAD modules in the azimuthal direction and each module has $\sim$ 30 cm of width. The barrel LAC has a total of 288 of EM and HAD modules.

There are 192 towers in the azimuthal angle and each has $\delta\phi = 33$ mrad opening angle. There are 34 EM towers in polar angle for the north and south sides, respectively, and each tower has from $\delta\theta = 21$ to 36 mrad depending on tower location for providing constant projective area. The HAD towers are twice

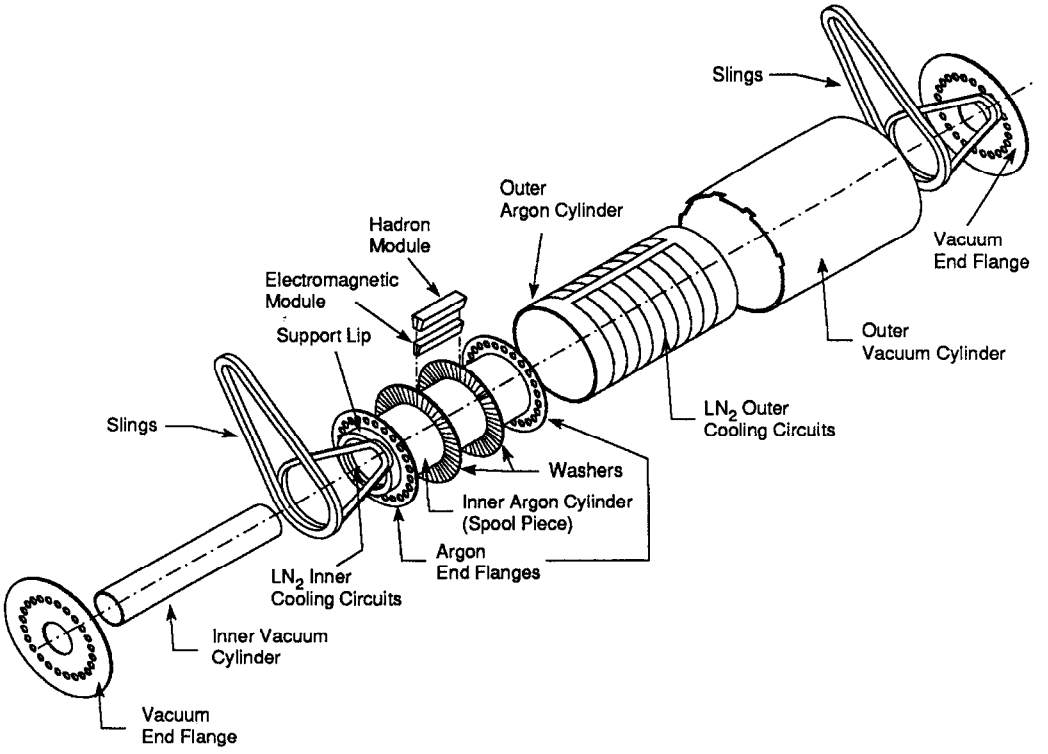

Figure 2.21 An exploded view of the barrel section of the LAC.

as wide as the EM towers in azimuthal angle due to different tower segmentation.

The EM module of 21 radiation lengths has two separate readout electronics sections for providing longitudinal shower information for e/π discrimination. The absorption length of a EM module is 0.84. The first section of 6 radiation lengths and second section of 15 radiation lengths are called "EM1" and "EM2", respectively. It is expected that the energy resolution of EM showers is $10-12\%$, including $1-2\%$ degradation from material in front of the LAC.

The HAD module of 2 absorption lengths also has two separate readout electronics sections. The first section of 1 absorption length and the second section of 1 absorption length are called "HAD1" and "HAD2", respectively. It is expected that the energy resolution of hadronic showers is about $60\%/\sqrt{E}$. The total of 2.8 absorption lengths in the LAC is expected to contain $\sim 85\%$ of hadronic shower

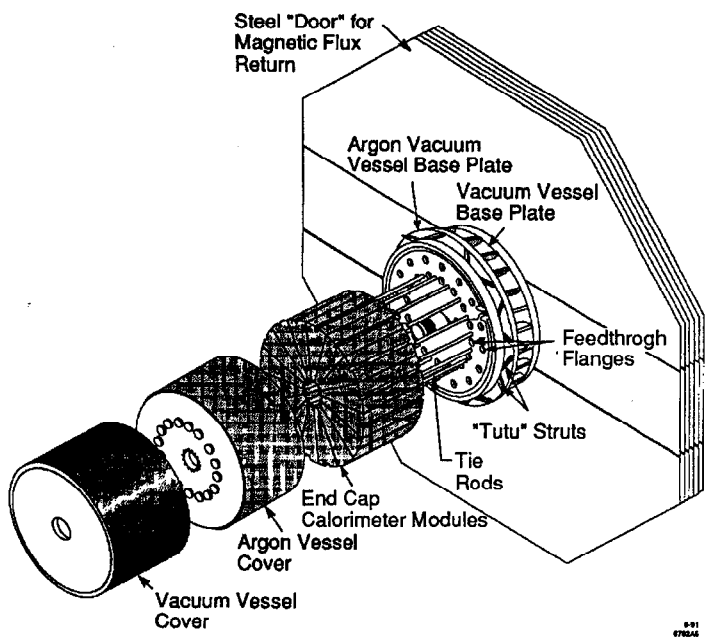

Figure 2.22 A schematic of the endcap section of the LAC

energy.

The endcap LAC covers the angular range $8° \leq \theta \leq 35°$ and $145° \leq \theta \leq 172°$. The two LAC endcaps are mounted on retractable end doors of the SLD and are located just inside the barrel LAC in radius. The endcap LAC consists of 16 wedge shaped modules. There is energy degradation in the overlap region ($31° < \theta < 35°$) with the barrel due to dewar and support material which is effectively $\sim$ 5 radiation lengths.

The endcap LAC modules are functionally similar to barrel LAC modules but there are differences in the module design and construction. The endcap modules incorporate both EM and HAD sections in one mechanical unit. The transverse segmentation in the endcap LAC is the extension of that of the barrel LAC as shown in Figure 2.22, but there are 192, 96, and 48 towers in the electromagnetic section depending on the polar angle, for providing a constant projective area.

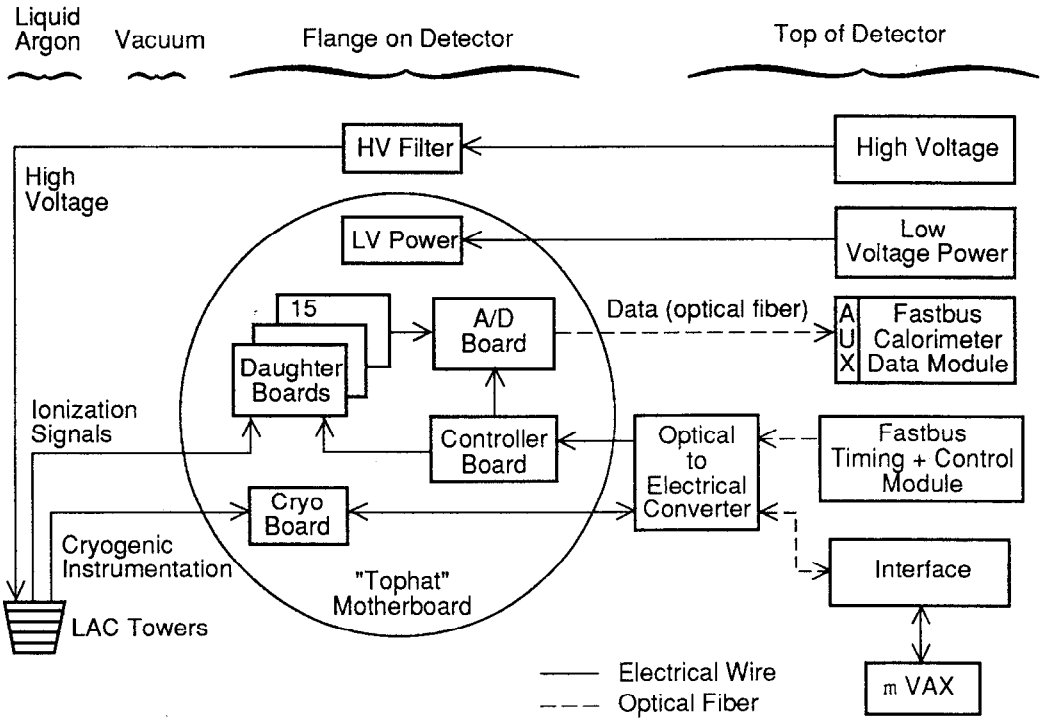

Figure 2.23 A logical layout of the barrel LAC electronics.

There are 17 towers in polar angle for both the north and south sides. The HAD towers are twice as wide as the EM towers in azimuthal angle, like the barrel.

The front-end electronics are located in a total of 64 tophats which are mounted directly on flanges on the outside of the cryostat. Of the 64 total, 48 and 16 tophats are for the barrel and endcap LAC electronics, respectively. Figure 2.23 shows the logical layout of the barrel LAC electronics from the LAC tower to data acquisition systems.

The barrel tophat is composed of 15 daughterboards, a power supply board, two high voltage feedthroughs, a controller board, an analog-to-digital converter (A/D) board, and a cryogenics instrumentation board. Each daughterboard has six charge sensitive preamplifiers and each preamplifier has 8 electronics tower channels. Figures 2.24 and 2.25 show the layout and the numbering of the preamplifiers

in the barrel and endcap tophats.

The endcap tophat is logically the same as that of the barrel but there are small differences due to different flange arrangements and space limitations. The endcap tophat consists of three motherboards. A motherboard of the endcap consists of 4 daughterboards and each daughterboard has 48 channels. The electronics are spread over four flanges and consist of one A type and three B types. The A type flange accommodates a power supply board, a high voltage feedthrough, a controller board, an A/D board, and a cryogenics board. There is no daughterboard in the A type motherboard. The three B type flanges accommodate four daughterboards for each flange. These flanges are connected electrically by flat jumper cables.

A Fastbus Timing and Control Module (TCM) sends commands and timing signals into the controller board of the tophat and the controller board controls the tophat. There are three signals from the TCM, which are a clock, a command and a data signal. The signals are transmitted by a set of optical fibers. The signals are converted from optical to electrical form by a optical-to-electrical converter before arriving at the tophat.

There are redundant fiber and cables sets for sending the signals from the TCM to the tophat for avoiding failure of the tophat due to optical fibers.

When charge is collected on the LAC tower electrodes, there follows amplification, shaping, sampling, storage and digitization on a mutiplexed A/D converter in the analog signal processing. A calorimeter data unit (CDU) is used for analog storage and multiplexing. Figure 2.26 shows a logical overview of the electronics from the LAC tower to the A/D board in the tophat.

The preamplifier boards are connected directly to the cryostat feedthroughs to access the input signals from the LAC towers. The analog signals are digitized by the A/D converter board in each tophat and the digitized signals are then

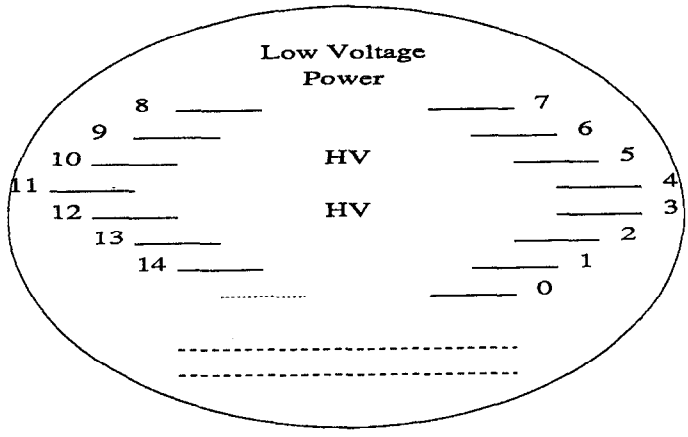

Figure 2.24 The layout and numbering of the boards within the barrel tophat. The solid lines are for the daughter boards, dotted lines are for the cryogenics board and dashed lines are for the controller and A/D board.

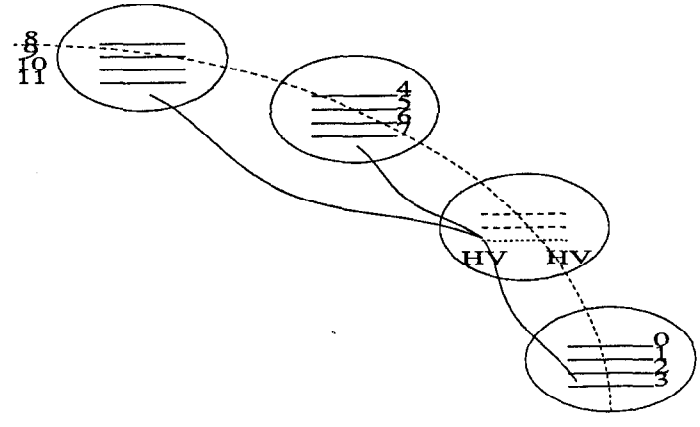

Figure 2.25 The layout and numbering of the boards within the south endcap tophat. The solid lines are for the daughter boards, dotted lines are for the cryogenics board and dashed lines are for the controller and A/D board.

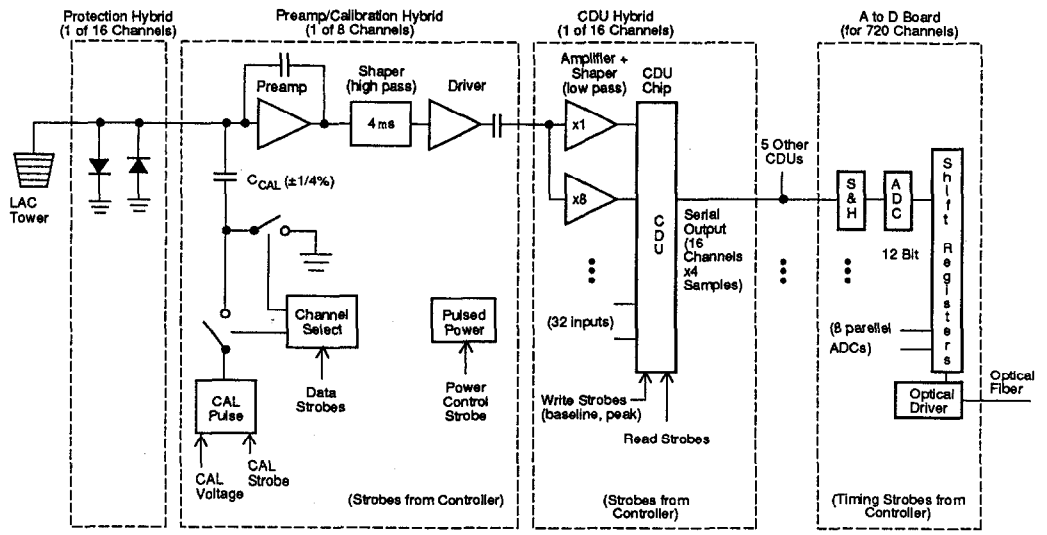

Figure 2.26 A diagram of the tophat signal processing.

transmitted serially on an optical fiber cable, which is plugged into auxiliary cards located on the back of the Fastbus Calorimeter Data Modules (CDMs). The CDM is responsible for receiving, correcting, and storing data from the front-end electronics. Each CDM reads and processes data from two tophats, giving a total of 32 CDMs for the LAC. The data is transmitted at 32 MH_Z. There is an "Aleph Event Builder" (AEB) which coordinates the operations of the TCM and CDMs. Figure 2.27 shows the schematic of the LAC fastbus system.

The Warm Iron Calorimeter

The warm iron gas calorimeter (WIC) is located outside the SLD solenoidal magnet, which also functions as the flux return of the magnetic field [36].

The WIC uses limited streamer tubes and has a total depth of ~ 4 absorption lengths. The WIC consists of eight iron sectors ("Octants") and two endcaps, which cover over 99% of the solid angle. The iron is segmented into 14 layers which are separated by 3.2 cm gaps instrumented with the plastic limited streamer tube chambers. Each chamber consists of a single layer of streamer tubes sandwiched

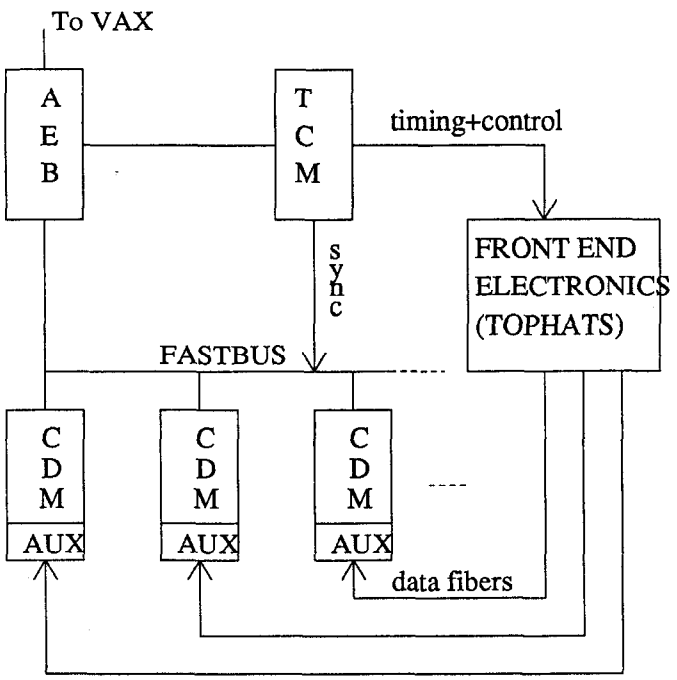

Figure 2.27 A schematic diagram of the LAC fastbus system.

between two external readout electrode sheets, which pick up the signals induced by streamer discharge.

The WIC provides a complete hadronic shower measurement, muon indentification and muon tracking. The limited streamer tubes are read out with strip electrodes for muon tracking and identification, and pad electrodes for hadron calorimetry.

The WIC pads in different layers of streamer tubes are daisy chained to form projective towers which point to the SLC interaction point. In the barrel both inner and outer octants consist of eight pad layers. The signals collected with

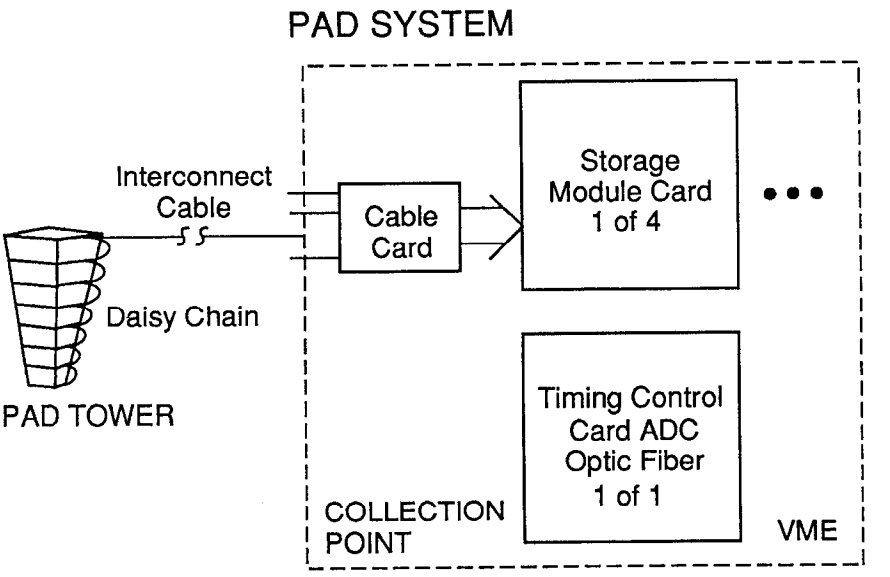

Figure 2.28 Schematic of a collection point.

the electrodes are recorded through analog amplifiers and are digitized. The WIC electronics are designed to acquire digital data from $\sim 80,000$ strip channels and analog data from $\sim 8,600$ calorimeter towers. The overall readout time is ~ 0.8 ms and the data is multiplexed and transmitted by optical fibers. The WIC also has redundant optical filber and cable sets like the luminosity monitor and the LAC.

Data from pad towers are read out through sixteen collection points, eight mounted on the barrel and four on each endcap, each comprising a VME crate and appropriate readout electronics. Figure 2.28 shows the electronics diagram of the WIC pad system. The signals from the towers are sent to VME cards and digitized by an analog-to-digital converter. Then the digitized signals are sent serially through fiber optic cables to two Fastbus Calorimeter Data Modules. The expected energy resolution is $80\%/\sqrt{E}$ (E in GeV).

The Trigger and Data Acquisition

Four independent triggers were used for taking 1992 data with polarized electron beams. *ENERGY* and *TRACK* triggers were used for triggering Z° events, a *BHABHA* trigger for small-angle Bhabha events, and a *RANDOM* trigger for background studies. The whole idea of the *ENERGY* and *TRACK* triggers is based on maximization of the number of Z° events.

1. The total energy of the LAC is formed by summing all towers exceeding a predetermined threshold, and this is used for the *ENERGY* trigger. The tower thresholds for the EM and HAD layers were 60 and 120 ADC counts, respectively, for eliminating the SLC muon background, and this threshold was called the "high tower thresholds". Due to the unique SLC muon background there are lots of SLC muon hits on the west and east side of the barrel LAC and this is called the "ring of fire". For reducing the ring of fire, the towers at $\Theta_{bin} = 48$ were excluded in the tower energy sum, which corresponds to the angular value $|\cos\theta| = 0.98$. Only energy above 8 GeV triggered the calorimeter detector. There was the "low tower thresholds" which is 8 (12) ADC counts for the EM (HAD) layers. This tower threshold was used for providing a noise monitor for the SLC and for vetoing the energy trigger. The energy trigger was vetoed in case the total LAC energy was above 150 GeV or the number of total tower hits above 1000 with low tower threshold.

2. The *TRACK* trigger required more than two charged tracks in the CDC, which has the angular coverage $|\cos\theta| \leq 0.8$. The opening angle between a pair of charged tracks was required to be more than 20° for eliminating background. At least 6 out of 8 sense wires must be hit to be counted as a hit cell and the track was required to have more than 8 superlayers with hit cells for triggering the *TRACK* trigger. The *TRACK* trigger caused readout of the full detector.

Since backgrounds easily triggered the *TRACK* trigger, a trigger rate limit was implemented for reducing the SLD dead time and the trigger was vetoed in case it triggered more than 10 events during 100 seconds. The trigger was also vetoed if the total hit cell count was above 275.

3. The total energy of the luminosiy detector on each side was summed, and all towers exceeding a predetermined threshold in the second electromagnetic layer (EM2) were used for the *BHABHA* trigger. A 1 GeV tower threshold was used in the EM2 layer for the *BHABHA* trigger. The towers of the medium angle silicon calorimeter did not participate in the trigger in order to reduce backgrounds. Events having energy above 10 GeV in the north and the south side, were triggered. Only the calorimetric part of the SLD was readout.

4. Random beam crossings were recorded by the *RANDOM* trigger on average every 20 seconds. This triggered the full detector and was used for background studies.

There is a non-independent trigger called the *HADRON* trigger. This trigger used information of both the LAC and the CDC, and it required the total LAC energy to be above 8 GeV with high tower threshold and at least a single track in the CDC. The *HADRON* trigger readout the full detector.

The CDM forms tower energy sums for use in the trigger decision. For triggered events, the CDM compacts the event data using layer-dependent threshold cuts, and attaches a tower identification tag to each hit above tower threshold. The AEB coordinates the operation of the CDMs [37], ensuring that they deliver information belonging to the same event. The AEB also reorganizes the tower identification tags and converts the data collected from the CDMs to the proper offline format for logging.

CHAPTER III

EVENT SELECTION

Introduction

Two independent triggers, $ENERGY$ and $TRACK$, were used for triggering Z° events. Since $ENERGY$ triggered events and endcap Z° events do not have tracking information from the drift chamber, the event selection procedures were based only on the calorimeters for the 1992 A_{LR} measurement.

All of the visible Z° decays except e^+e^- and $\mu^+\mu^-$ final states were used for the A_{LR} measurement. Since there was no independent muon pair trigger in the 1992 run and the event selection only used the information of calorimeter tower hits, muon pair events were not included in the final data set. Since the e^+e^- final state has t-channel contributions, it was also excluded.

The event selection procedures were for hadronic Z° or τ pair events using the liquid argon calorimeter (LAC) and the endcap warm iron calorimeter (WIC) pads [38]. The event selection procedures consist of three event selection filters. All three filters use only the tower hit information of the calorimeters and do not use any reconstructed cluster information. The first filter ($KZ0FLT$) is used for selecting possible hadronic Z° events including tau pair and wide-angle Bhabha events. The second stage filter ($KWABID$) is used for removing wide-angle Bhabha candidates. Finally, the third stage filter ($KMONOJT$) further removes beam-related background events. The three filters are described in the following section.

In order to develop criteria for removing wide-angle Bhabha events and beam-related backgrounds, approximately 12,000 events were handscanned. In addition,

the scan served as the basis for wide-angle Bhabha and beam-related background estimations in the final data set.

The events are classified as hadronic Z°, tau pair, wide-angle Bhabha and beam-related events by the following scanning criteria:

- Hadronic Z° Events
  1. Sufficient and well balanced energy deposition in the LAC.
  2. Sufficient number of vectored hits in the central drift chamber if there is tracking information available.
- Tau Pair Events
  1. Multi-prong events are separated from wide-angle Bhabha events by the number of vectored hits if there is tracking information.
  2. Transverse shower shapes of tau events are broader than those of wide-angle Bhabha events and longitudinal shower shapes are also different since wide-angle Bhabha events deposit most of the energy in the electromagnetic layers.
  3. Tau events which have $\tau \rightarrow e$ decay mode were classified as wide-angle Bhabha events.
  4. Tau events can have unbalanced energy depositions but these were classified as beam-related backgrounds in order to avoid confusion with real beam-related backgrounds.
- Wide-angle Bhabha Events
  1. Two tracks if there is tracking information available.
  2. Generally, two clusters that are contained in a small number of electromagnetic towers.
  3. In the overlap region between the barrel and endcap LAC, clusters can be smeared and separated into the barrel and endcap regions.
  4. In the endcap region transverse shower shapes of clusters can be broader than those of clusters in the barrel because of preshowering due to interactions with

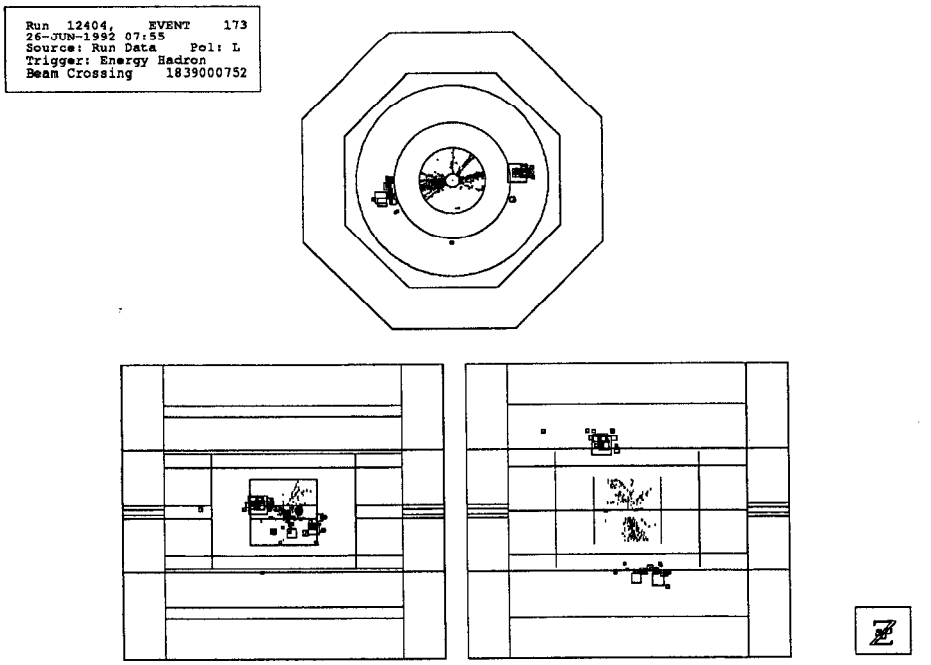

Figure 3.1 Typical hadronic Z° event with LAC tower hits and vectored hits in the central drift chamber.

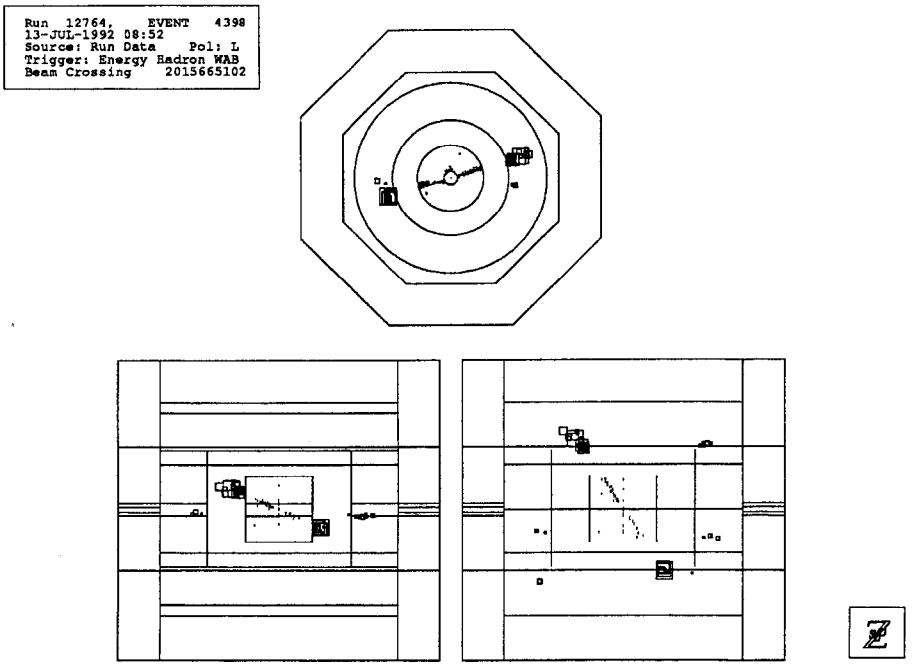

Figure 3.2 Typical tau pair event.

materials in front of the endcap LAC.

5. In the deep forward region there are significant energy leakages into hadronic layers.

- Beam-related Background Events
  1. Tower hits which are long, narrow, and parallel to the beamline.
  2. Low energy deposition in the LAC and not well balanced energy deposition.
  3. Sufficient energy deposition in the LAC but clusters do not point back to the SLC interaction point.
  4. Most of the vectored hits do not point back to the SLC interaction point if there is tracking information available.

Figures 3.1 and 3.2 are typical hadronic Z° and tau pair events, respectively. The LAC tower hits and sense wire hits in the central drift chamber are shown in the Figures.

The estimated background from wide-angle Bhabha and beam-related background events with the above event criteria and the combined efficiency of the trigger and filtering for selecting hadronic Z° and tau pair events are described in this Chapter.

In the 1992 polarized beam run 13,478 events passed the first stage filter ($KZ0FLT$) and after all three stages 10,437 events were identified as hadronic Z° or tau pair events and comprised the data set for the A_{LR} analysis.

The final event sample was scanned by using an event display which has the LAC tower hits and central drift chamber vectored hits. The estimated background from wide-angle Bhabha and beam-related background events is $(1.9 \pm 0.7)\%$.

Event Selection Procedure

Introduction

There are 49 and 25 LAC towers in the electromagnetic (EM) and hadronic

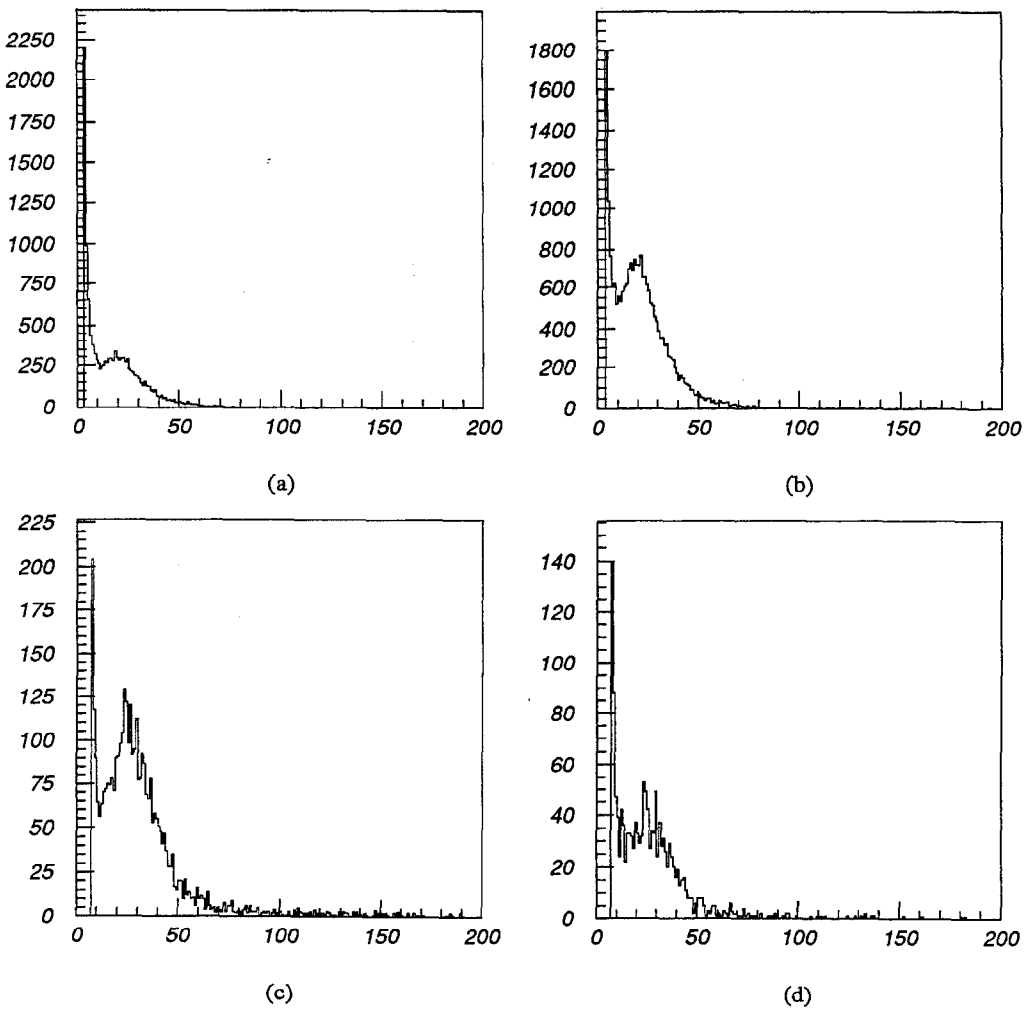

Figure 3.3 ADC distributions of tower hits of identified SLC muons for four LAC layers. (a)–(d) are EM1, EM2, HAD1, and HAD2 layers, respectively.

(HAD) layers in the angle from the beamline (polar angle), respectively. Since each LAC tower has an electronics readout, the LAC towers are labelled as bins in the angle. The EM towers are binned from 0 to 48, while the HAD towers are binned from 0 to 48 by even numbers. Thus the LAC covers the range from $\Theta_{bin} = 0$ to $\Theta_{bin} = 48$ on each side of the SLD. $\Theta_{bin} = 0$ represents the towers at $\theta = 90°$, where θ is the scattering angle with respect to the beamline.

The liquid argon ionization energy is 23.6 eV, and 21,200 ionized electrons are produced for a 1 MeV energy deposition in the liquid argon and are collected by the LAC preamplifiers (a factor of 1/2 comes from uniform ionization across the argon gap):

$$\begin{aligned} \text{1 MeV Deposition} &\rightarrow \frac{1}{2}\left(\frac{10^6\ eV}{23.6\ eV}\right) \\ &= 21,200\ e^- \end{aligned}$$

The electronics are calibrated using DAC pulses ranging from 0−2.5 Volts, which charges 8.4 pF capacitors in the preamplifier. The calibration constants are stored in Calorimeter Data Modules (CDM's) for correcting the data. Since one "calibrated ADC" count corresponds to 8,011 ionized electrons, 1 MeV energy deposition in the liquid argon corresponds to 2.64 calibrated ADC counts. The EM and HAD sampling fractions based on dE/dx for muons are 0.185 and 0.070, respectively. Conversion factors from ADC counts to GeV for the EM and HAD layers are then 489 and 185 ADC/GeV. When an energy is calculated in GeV by using these conversion factors, it is called an energy in "muonic"(or "min i") scale. These conversion factors correspond to 0.262 and 0.692 in units of 1/128 GeV. The electromagnetic showers calibrated by the muons indicated an e/μ response of the liquid argon to be 0.69 [39]. When an energy in the muonic scale is corrected by an e/μ factor, it is called an energy in "electronic" scale.

ADC counts of the LAC tower hits are required to be greater than 2, 3, 6 and 6 for the two EM and HAD layers, respectively, for reading out the LAC tower energy. These ADC count requirements on the LAC tower hits are called "readout thresholds".

The halos of the electron and positron beams can interact with nuclei in SLC collimators (beam optics elements), or the beampipe and produce hadrons. Muons are produced by decay of these hadrons and are a significant source of the SLD beam background, called " SLC muons". Figure 3.3 shows ADC spectra of the EM and HAD layers for clusters identified as SLC muons. The spike in the low ADC region is due to electronics noise above the readout thresholds and it also shows that the ADC count of the SLC muons is about 20−30.

Characteristics of SLC muons are that they produce longitudinally isolated and non-projective LAC tower hits, and low and not well balanced energy depositions in the LAC. Figure 3.4 shows a SLC muon event. Most beam-related background events come from SLC muons and the remaining backgrounds consist of cosmic rays and beam gas. It is estimated that the fraction of hadronic Z° to total triggered events is 1%.

In order to remove background energy effectively while preserving the higher energy Z° events, tower thresholds of the EM and HAD layers were chosen as 60 and 120 ADC counts, respectively [40]. These tower thresholds are called "high tower thresholds".

Due to large SLC muon backgrounds in the closest LAC towers to the beamline, called the "ring of fire", towers of $\Theta_{bin} = 48$ are excluded in calculating analysis quantities.

First Stage ($KZ0FLT$)

$KZ0FLT$ filter uses the LAC and endcap WIC pads tower hit information

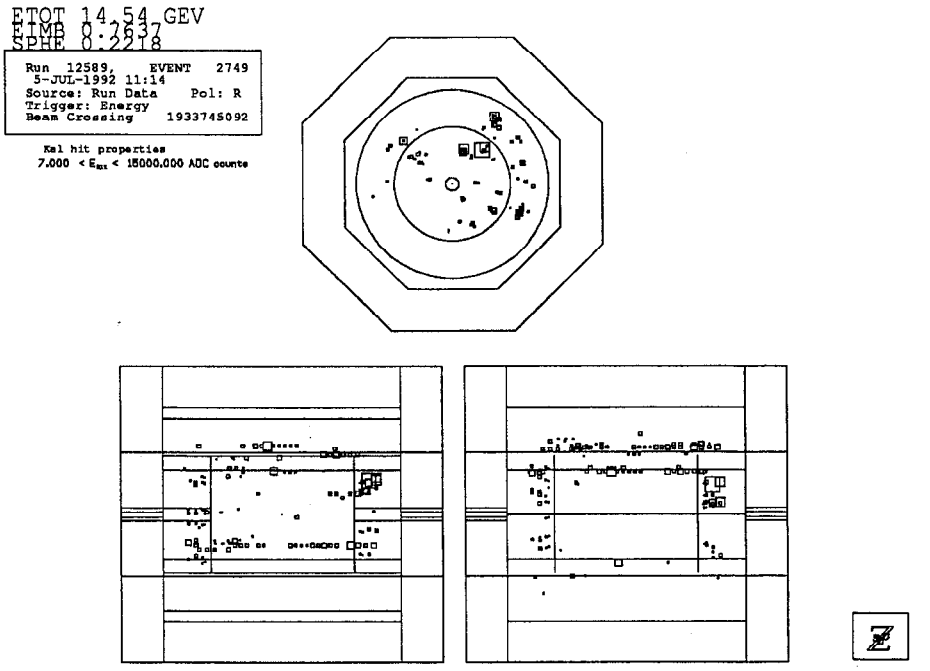

Figure 3.4 Typical SLC muon event which has barrel LAC tower hits parallel to the beamline.

for selecting hadronic Z°, tau pair and wide-angle Bhabha events. The LAC is segmented longitudinally into two electromagnetic layers, referred to as EM1 and EM2, and two hadronic layers, HAD1 and HAD2. The HAD layers are segmented transversely into towers which are twice as large as the EM towers in both θ and ϕ (except $\Theta_{bin} > 45$, where the ϕ segmentation of the HAD layers is the same as that of the EM layers). Hence, each HAD tower has four corresponding projective EM towers.

In calculating the quantities E_{LAC}, E_{IMB} and $SPHE$ as defined below, the high tower thresholds were applied. E_{LAC} is the sum of the tower energies, E_{IMB} is the energy imbalance in the LAC and $SPHE$ is defined as the sphericity of the event [41]. The sphericity tensor is given by

$$S_{\alpha\beta} = \frac{\sum E_{i\alpha} E_{i\beta}}{\sum E_i^2} \tag{37}$$

After diagonalizing $S_{\alpha\beta}$, three eigenvalues λ_1, λ_2 and λ_3 are given. Then the sphericity is given by

$$SPHE = \frac{3}{2}(\lambda_2 + \lambda_3)$$

where $\lambda_1 \geq \lambda_2 \geq \lambda_3$ and $\lambda_1 + \lambda_2 + \lambda_3 = 1$.

Because SLC muons tend to produce LAC tower hits which are longitudinally isolated and non-projective, it is useful to define a total LAC energy, E_{TOT}, which excludes the obvious background hits. The LAC EM towers are included in E_{TOT} only if both EM1 and EM2 are hit, and HAD towers are included in E_{TOT} only if one of the four corresponding EM towers has qualified (these are defined as "non-isolated" hits). Hence, E_{TOT} is defined as the sum of non-isolated tower energies. E_{LAC}, E_{TOT} and E_{WIC}^{end} are calculated using the electronic energy scale.

The LAC can have many tower hits due to mis-steering of beams or many SLC muons, and a cut on the number of LAC towers was applied for removing these events. For removing the SLC muon events, a significant energy deposition in the LAC is required after high tower threshold cuts. An E_{LAC} cut was used. For removing "ring of fire" events, a relatively significant energy depositon in the LAC compared with endcap WIC energy is required. Cosmic rays and beam gas events can sometimes deposit significant energy in the LAC, however the distribution of energy depositions is very asymmetric in the polar angle. SLC muon events also have characteristically unbalanced energy depostions in the LAC. Hence, the energy imbalance and sphericity cuts were applied for removing these events.

The selection cuts are defined as follows:

1. $0 < N_{LAC} < 3,000$

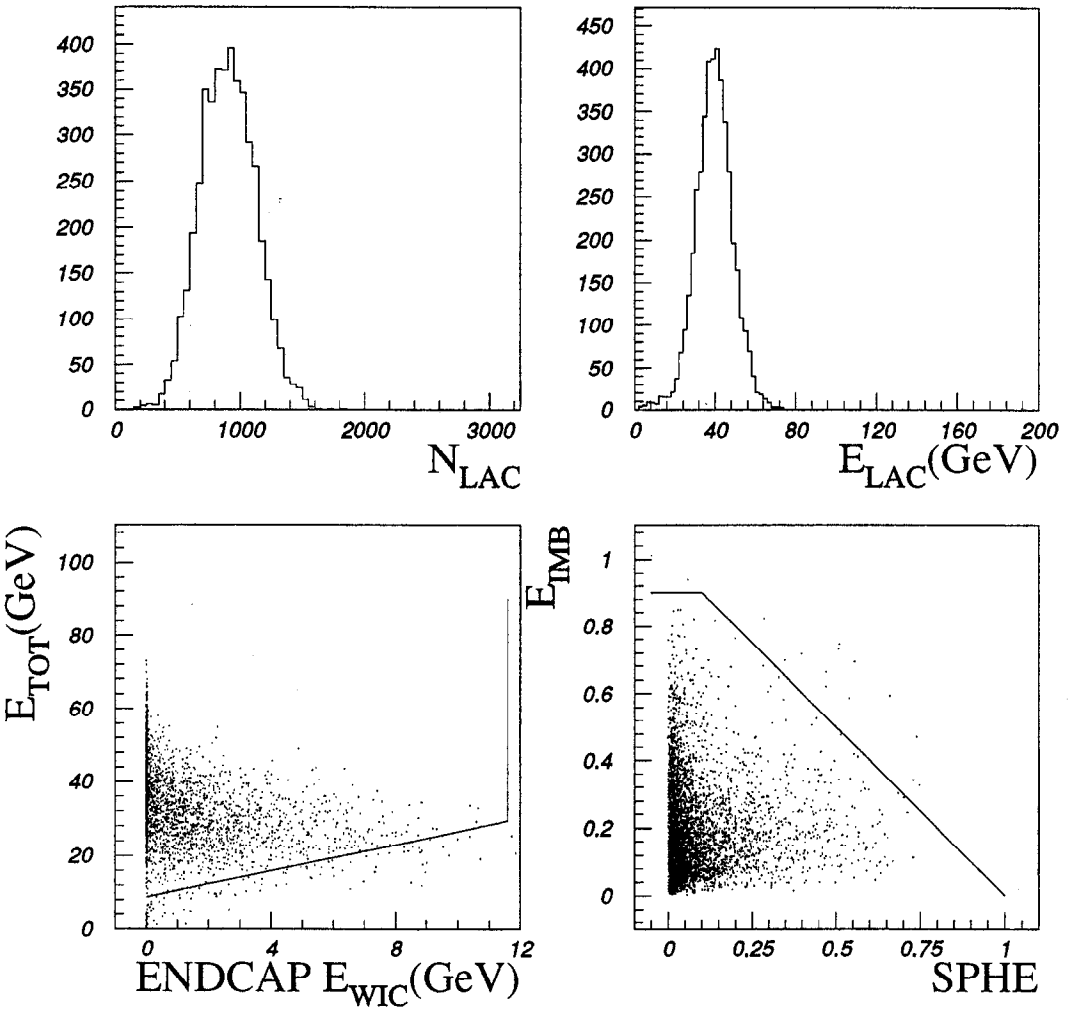

Figure 3.5 The distribution of N_{LAC}, E_{LAC}, E_{WIC}^{end}, E_{IMB} and SPHE of Monte Carlo hadronic Z° events.

where N_{LAC} is the number of towers in the four LAC layers above the readout thresholds.

2. $E_{LAC} > 20$ GeV
3. $E_{WIC}^{end} < 11.6$ GeV and $E_{TOT} - E_{WIC}^{end} > 8.7$ GeV
   where E_{WIC}^{end} is the sum of the endcap WIC pads towers with non-isolated hits. The e/μ factor is 0.95 for the WIC.
4. $E_{IMB} < 0.9$

$$E_{IMB} = \frac{1}{E_{TOT}} \sqrt{(\sum E_x)^2 + (\sum E_y)^2 + (\sum E_z)^2} \ .$$

   where $E = \vec{E} \cdot \hat{r}$ and $\hat{r} = (\sin\theta\cos\phi, \sin\theta\sin\phi, \cos\theta)$. Energy, E, is the tower hit energy, and the polar (θ) and azimuthal angles (ϕ) are calculated at the center of towers.
5. $E_{IMB} + SPHE < 1.0$
   This cut was developed during the 1991 engineering run when beam backgrounds were severe. It had a negligible effect on the 1992 data and this cut was not used for the 1993 run.

Cuts (1) and (2) are offline versions of the $ENERGY$ trigger and (3), (4) and (5) were designed to eliminate SLC muon events.

Figure 3.5 shows the distributions for Monte Carlo hadronic events of the quantities applied to remove the background events. It shows that these cuts are quite efficient in preserving Z° events.

Figure 3.6(a) shows the distribution of N_{LAC} for all triggered events of four sample runs, from run number 13,605 to 13,608, which were logged in August 1992, and the distribution of E_{LAC} is shown in Figure 3.6(b). Figure 3.6(c) is the distribution of E_{LAC} after the N_{LAC} cut and it shows that many high energy

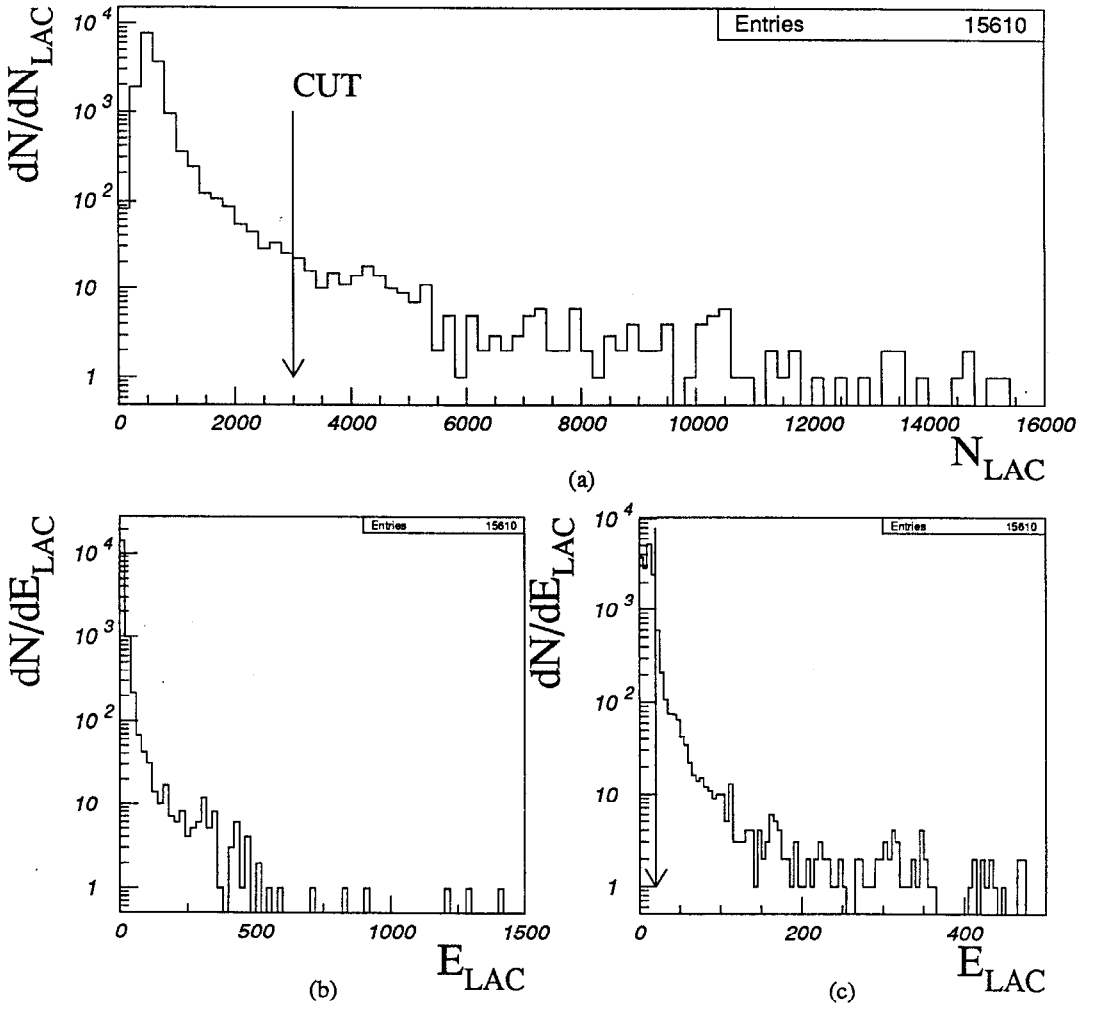

Figure 3.6 (a) is the number of tower hits, (b) is the total energy of the LAC tower hits in the four LAC layers for all triggered events of the four sample runs, and (c) is the total LAC energy distribution for the events which passed the N_{LAC} cut.

events are removed by cut (1). About 98% of triggered events pass cut (1).

Figures 3.7(a) and (b) are scatter plots of E_{TOT} versus E_{WIC}^{end} after cut (1) and cuts (1) and (2), respectively. Cut (3) is also shown in Figure 3.7(b) and about 8% of triggered events pass cuts (1) and (2), indicating cut (2) is one of the most effective cuts. Figures 3.7(c) and (d) are E_{IMB} distributions after cuts (1) and (2), and cuts (1), (2) and (3), respectively. About 1.5% of all events pass cuts (1), (2) and (3). Most random triggers, and low energy beam-related background events which mostly come from $TRACK$ and $BHABHA$ triggers are removed by requiring sufficient energy deposition in the LAC, and high energy beam-related backgrounds are populated in the high energy-imbalance region, as seen by the large spike in Figure 3.7(d).

Figures 3.8(a) and (b) are scatter plots of E_{IMB} versus $SPHE$ after cuts (1), (2), (3) and cuts (1), (2), (3) and (4), respectively. About 40% of events which passed the first three cuts are removed by the E_{IMB} cut, indicating cut (4) is an effective cut. Cut (5) is shown in Figure 3.8(b) and Figure 3.8(c) is the E_{TOT} distribution after all cuts are applied. There is a peak from hadronic Z° events and it also shows some wide-angle Bhabha events at high energy.

When these five cuts were applied to the 1992 polarized beam run, 13,478 out of all triggered events passed. Figure 3.9 is the distributions of events which passed the first filter and shows the distributions of the quantities N_{LAC}, E_{LAC}, E_{WIC}^{end}, E_{IMB} and SPHE. By comparing the E_{LAC} distributions in Figures 3.5 and 3.9 it is shown that good hadronic Z° and wide-angle Bhabha events are populated around 40 GeV and 90 GeV, respectively. The E_{IMB} distributions in Figures 3.5 and 3.9 show that most beam-related background events have high E_{IMB}.

Table 3.1 is a statistics summary of the five cuts in the first filter for the four sample runs.

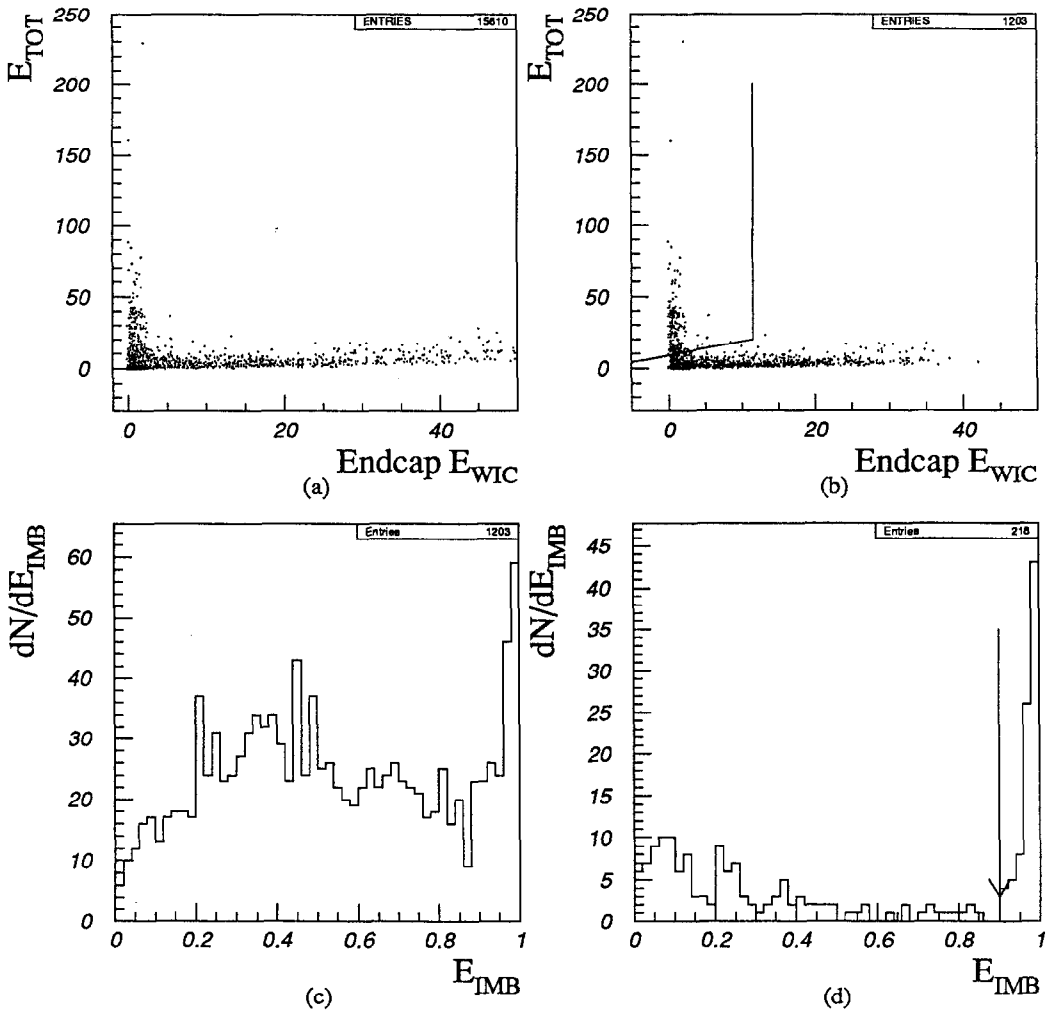

Figure 3.7 (a) is the distribution of the total LAC energy and the endcap WIC energy for the events which passed the N_{LAC} cut for the four sample runs, (b) is the same distribution as (a) and (c) is the energy imbalance distribution for the events which passed the N_{LAC} and E_{TOT} cuts. (d) is the same distribution as (c) except for applying one more cut (3).

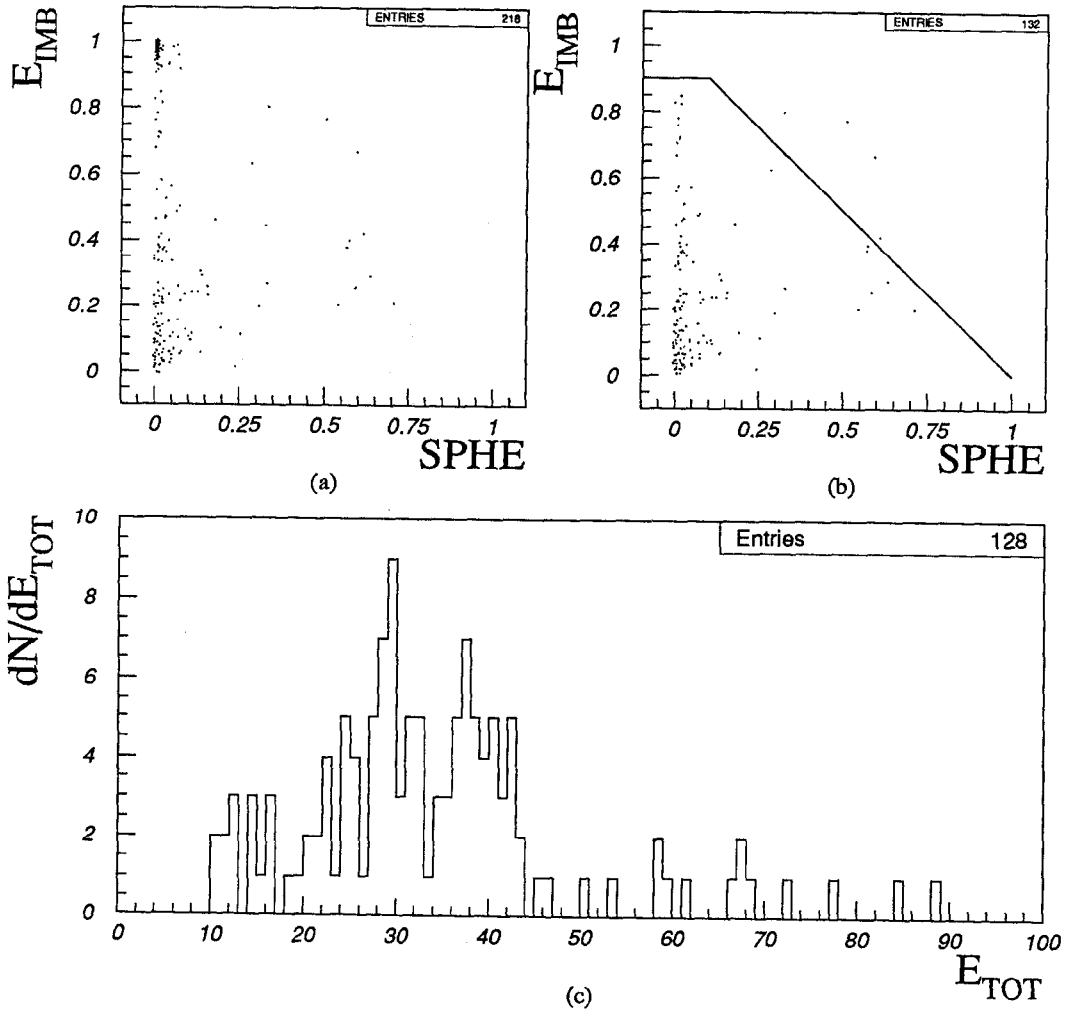

Figure 3.8 (a) is the distribution of the energy imbalance and sphericity for the events which passed cuts (1), (2), and (3) for the four sample runs, (b) is the same distribution of (a) after cuts (1), (2), (3), and (4), and (c) is the total LAC energy distribution of non-isolated tower hits after all cuts applied.

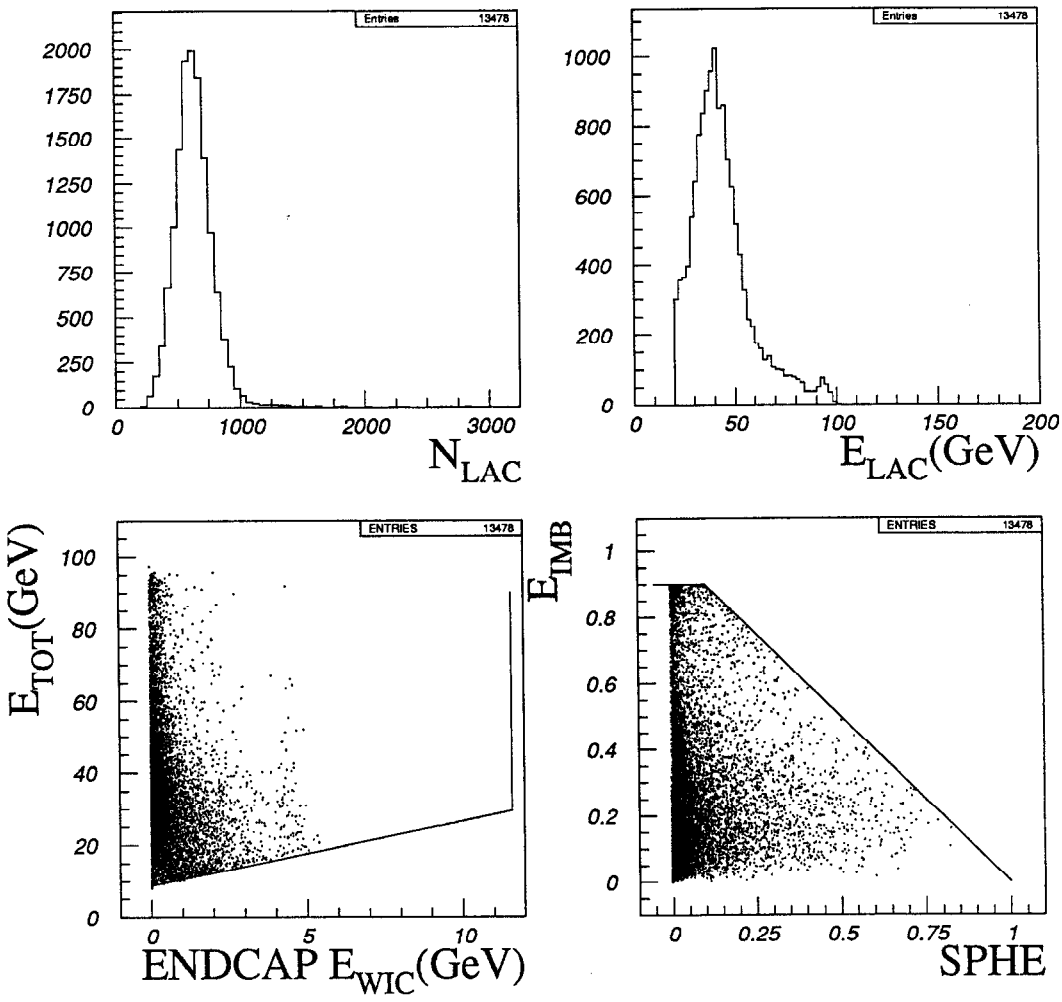

Figure 3.9 The distribution of N_{LAC}, E_{LAC}, E^{end}_{WIC}, E_{IMB} and SPHE of events which passed the first filter for all triggered events of the 1992 polarized run. .

Selection Cuts	Number of Events
Input Rawdata	15,610
(1)	15,353
(2)	1,203
(3)	218
(4)	132
(5)	128

Table 3.1 Statistics summary of cuts for the four sample runs. (1) is the number of the LAC tower hits cut. (2) is the sum of the total tower hit energies cut. (3) is the sum of the endcap WIC pads tower energies cut along with the total LAC energy of non-isolated tower hits. (4) is the energy imbalance cut. (5) is the sphericity cut along with the energy imbalance cut.

Second Stage ($KWABID$)

Since s-channel wide-angle Bhabha (WAB) events represent a small fraction of useful A_{LR} events and cannot be completely separated from t-channel WAB events, it is reasonable to eliminate all identifiable WAB events. Figure 3.10 shows the distribution of E_{TOT} and E_{IMB} for all events which passed the first filter. WAB events can be seen around 90 GeV of E_{TOT}, whereas beam-related background events due to SLC muons tend to populate the large-E_{IMB} regions.

The $KWABID$ filter attempts to remove WAB events in the following way. On average, about 95% of the total energy of a barrel WAB electron or positron is deposited in two towers in the LAC EM1 and EM2 layers. The quantity S_4 is defined as the sum of two maximum towers in the EM1 and two maximum towers in the EM2 with 2 GeV tower threshold cut. Let $TMAX$ be Θ_{bin} of the tower having the maximum $EM1$ energy. A factor 0.524 GeV/128 ADC (the "min i" $\times$ 2), called the "trigger" scale, is used for conversion from ADC to energy for S_4.

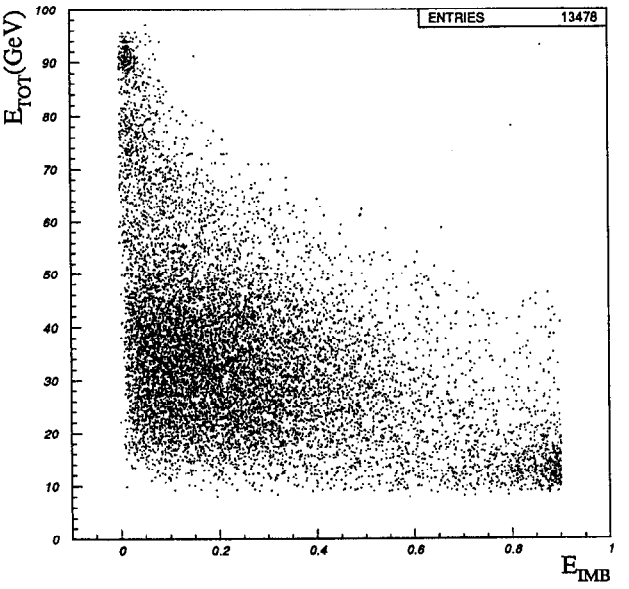

Figure 3.10 The distribution of total LAC energy versus the energy imbalance for the events which passed the first filter.

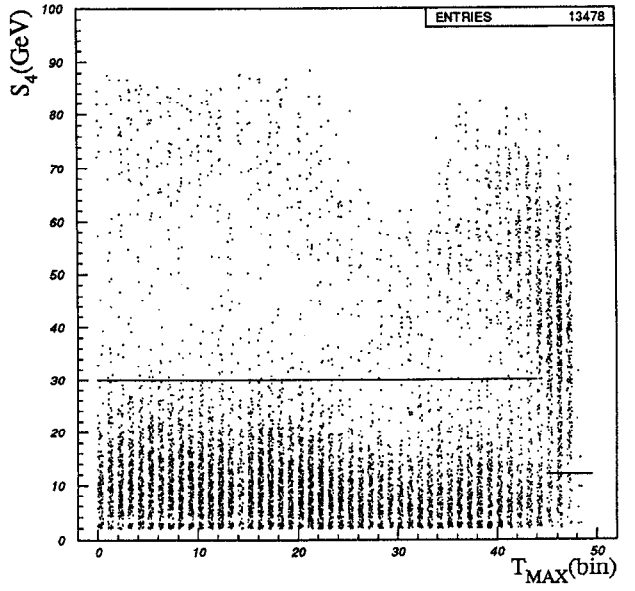

Figure 3.11 The distribution of the sum of four maximum electromagnetic tower energies versus theta (binned in electromagnetic towers) for the events which passed the first filter.

A WAB is then defined as an event which meets the following criteria:

1. Region (I): $S_4 > 30 \quad TMAX \leq 44$
2. Region (II): $S_4 > 12 \quad TMAX > 44$

Figure 3.11 is a scatter plot of S_4 versus $TMAX$ for all events which passed the $KZ0FLT$ filter and it also shows the dependence of the energy cut on $TMAX$. The necessity of using different cuts for different acceptance regions became apparent from this figure. There is energy degradation in the forward region and an abundance of events with relatively low energy compared with barrel WAB events, which were identified as WAB events by handscan results. Region (II) above was found to select a majority of these events.

Figure 3.12 is the event display of a typical endcap Bhabha event, while Figure 3.13 is an event which was mis-identified as a hadronic or tau event. Preshowering is presumably the cause of the lower tower energy in the endcap region and there are also WAB events with even more energy degradation than the remainder of the endcap in $\Theta_{bin} > 44$ due to lots of energy leakage into the hadronic layers.

1,865 events satisfied these criteria and were removed from the A_{LR} sample. Figure 3.14(a) is the E_{TOT} distribution versus E_{IMB} of events which are identified as WAB events by region (I) and (II) cuts. Figure 3.14(b) shows the total energy distribution of 1,865 events with a large spike around 90 GeV to indicate good barrel WAB events. Figures 3.14(c) and (d) show the energy distribution of identified events as WAB events in regions (I) and (II), respectively. Since the barrel LAC covers to about T_{MAX} of 32, there is a low energy tail from the endcap WAB events and the overlap region between the barrel and endcap LAC, as shown in Figure 3.14(c). Figure 3.14(d) shows much lower energies which passed the region (II) cut and it also shows the much lower energy in the deep endcap region compared to the remainder of the LAC.

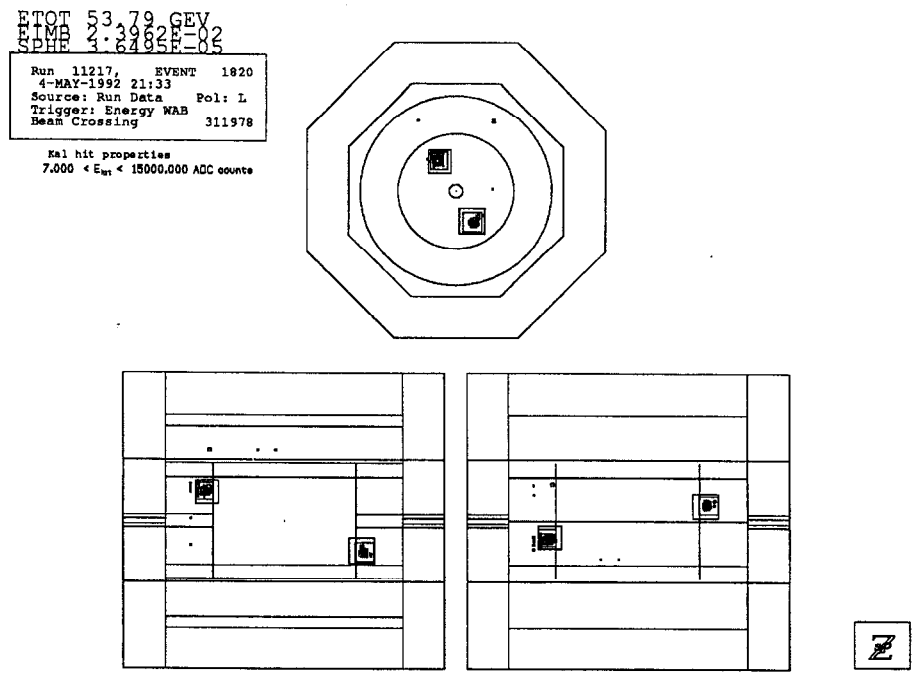

Figure 3.12 Typical wide-angle Bhabha event in the endcap liquid argon calorimeter.

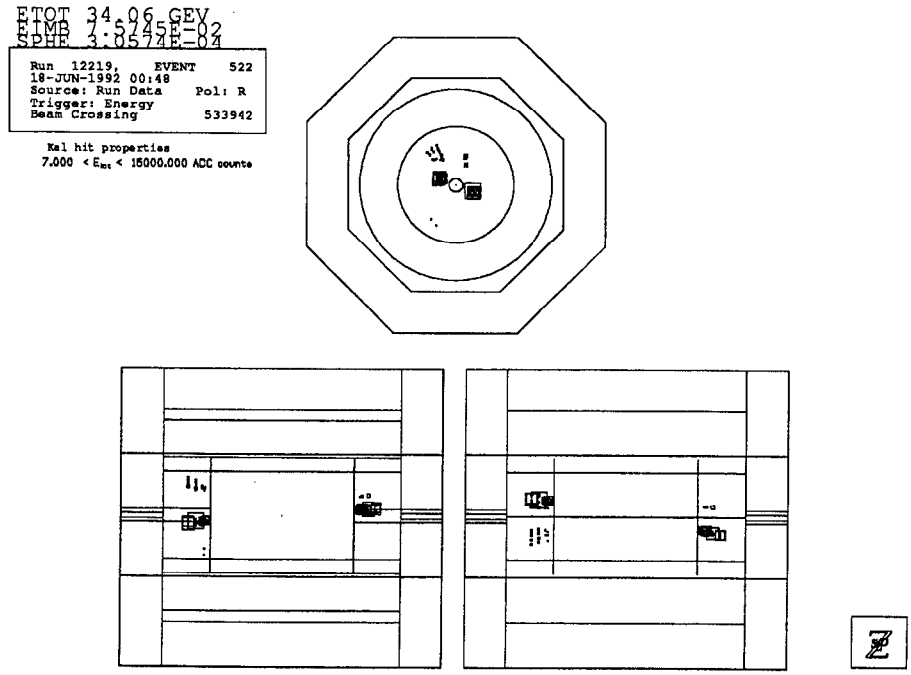

Figure 3.13 Suspicious event (presumably a wide-angle Bhabha) which has lots of energy leakage in the hadronic layers at $T_{MAX} > 44$.

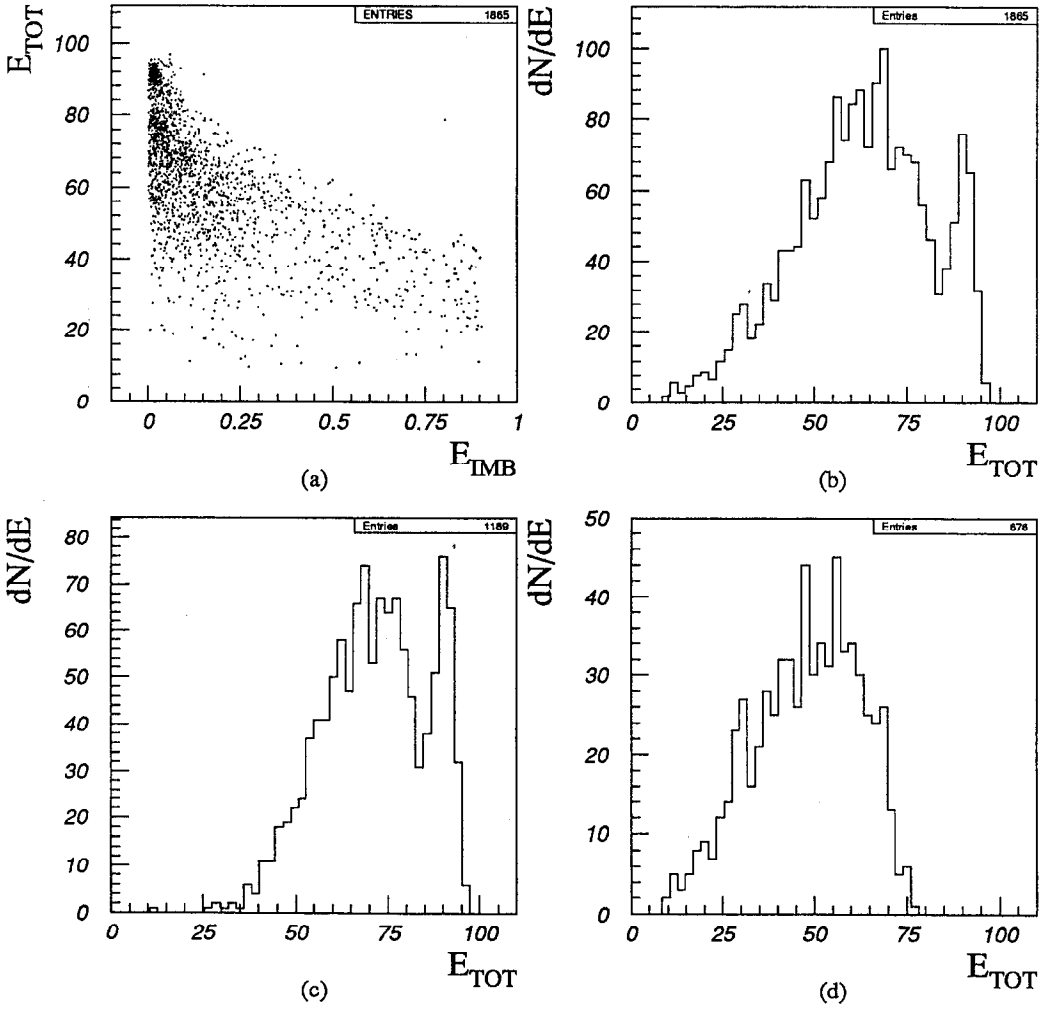

Figure 3.14 (a) is the distribution of the total LAC energy and the energy imbalance, (b) is the total LAC energy distribution, and (c) and (d) are the total energy distributions in regions (I) and (II), respectively, for the events which are identified as wide-angle Bhabha.

Third Stage ($KMONOJT$)

The $KMONOJT$ filter in this stage is used for removing the SLC muon events which are the source of most beam-related backgrounds. Since energy depositions are expected in the EM layers for hadronic Z° and tau pair events, $M1$ ($M2$) is defined as the maximum tower energy in the EM layers for the north (south) side of the SLD. Each side of the SLD detector is defined as a hemisphere.

Figures 3.15(a)-(c) show the distributions of E_{TOT} versus E_{IMB}, minimum tower energy out of maximum tower energy for each hemisphere, ($MIN(M1, M2)$) versus E_{IMB}, and E_{TOT} versus $MIN(M1, M2)$, respectively, for events which passed the first filter and were not identified as WAB events in the second filter. The lines shown in the Figure are the E_{TOT}, $MIN(M1, M2)$ and E_{IMB} cuts which are applied in this stage. Clearly, the majority of WAB events having large E_{TOT} and small E_{IMB} were removed by the second filter. Figure 3.15(b) shows that beam-related backgrounds are accumulated at small $MIN(M1, M2)$ and large E_{IMB}.

Good hadronic Z° or tau pair events are required to pass the following cuts:

1. $14.5 < E_{TOT} < 101$ GeV
2. $E_{IMB} < 0.8$

   This is tighter than cut (4) in the first filter.
3. Min$(M1, M2) > 0.5$ GeV

   $M1$ and $M2$ energies are calculated with the trigger energy scale.

Figures 3.16(a)-(c) show the distributions of 3.15(a)-(c) with one of the three cuts applied in this stage.

Based on a handscan of all events which passed the first filter and were not identified as WAB events in the second filter, it is estimated that the $KMONOJT$ is $(91 \pm 4)\%$ efficient at removing residual beam-related backgrounds. An estimated

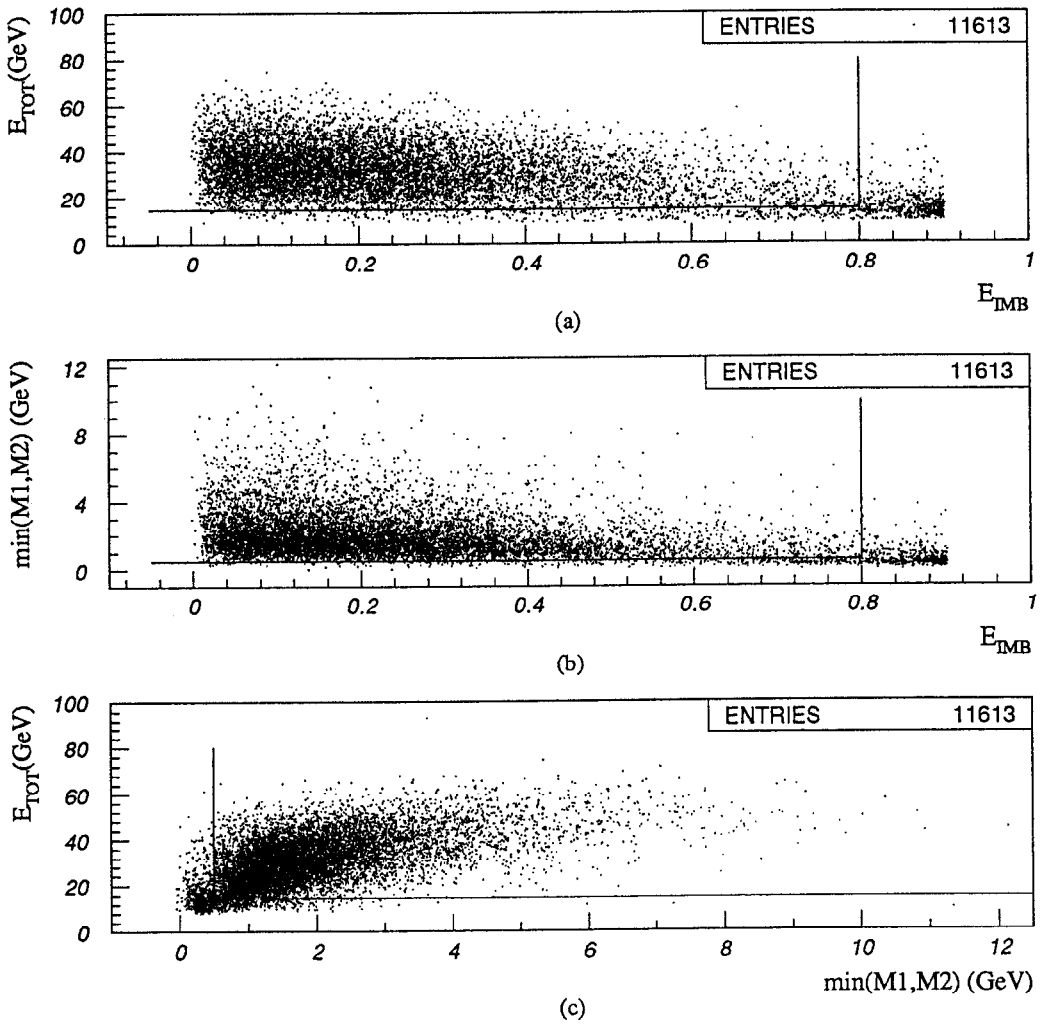

Figure 3.15 (a) is the distribution of the total LAC energy versus energy imbalance, (b) is the distribution of the minimum energy out of two maximum electromagnetic tower energies and the energy imbalance, and (c) is the distribution of the total LAC energy and the minimum tower energy out of two maximum electromagnetic tower energies for the events which passed the first filter and were not identified as wide-angle Bhabha events.

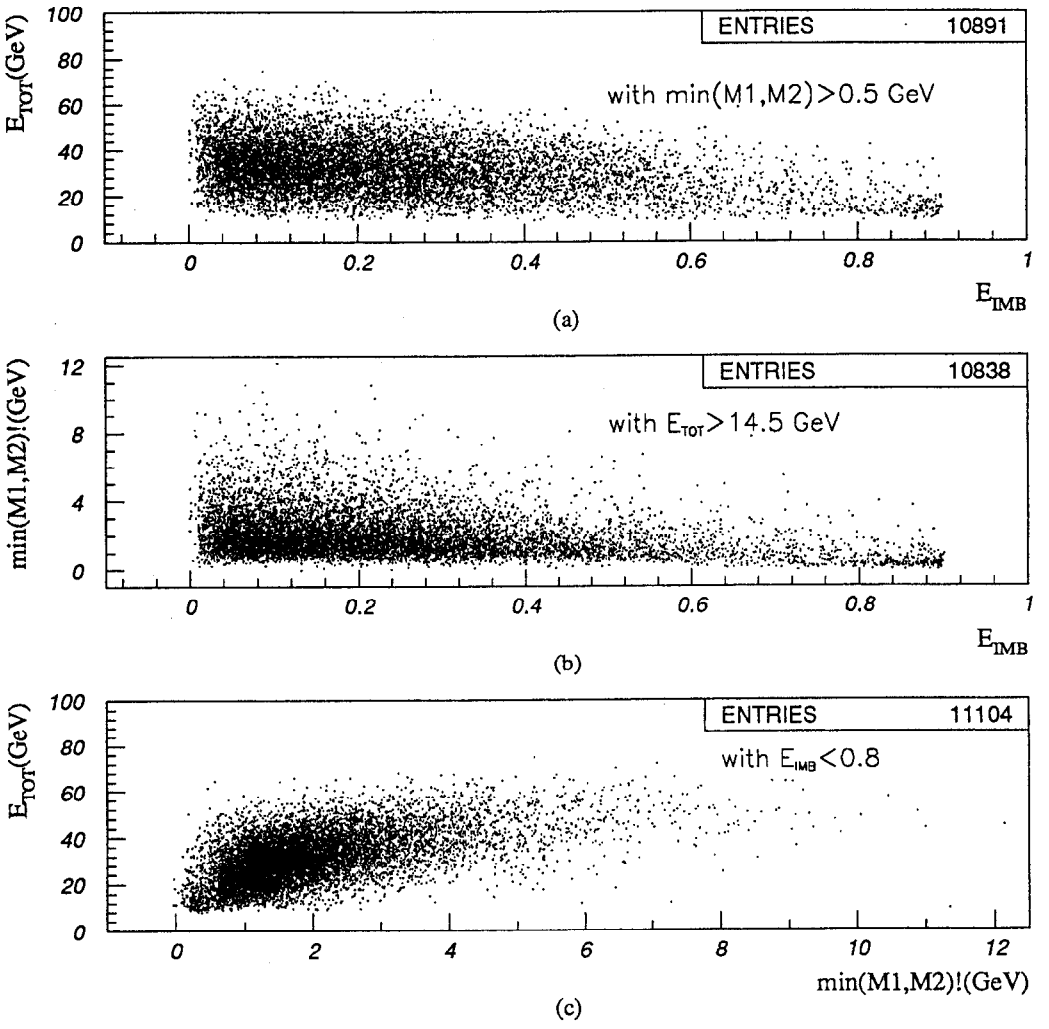

Figure 3.16 (a) is the distribution of the E_{TOT} versus E_{IMB} after cut(3), (b) is the distribution of the $MIN(M1, M2)$ versus E_{IMB} after cut (1), and (c) is the distribution of the E_{TOT} versus $MIN(M1, M2)$ after cut (2), for events which passed the first filter and were not identified as wide-angle Bhabha.

lower limit of $(96 \pm 1)\%$ efficiency of this procedure for selecting hadronic and tau pair events is obtained by assuming all *HADRON* triggered events are good hadronic Z° or tau pair events.

Figures 3.17(a)-(d) show the total LAC energy dependence in the acceptance region, the distribution of the total LAC energy, the distribution of the energy imbalance and the minimum tower energy out of two maximum electromagnetic tower energies, respectively, for the final event sample. Figure 3.17(a) shows the energy degradation due to the washer, which separates "center" and "end" modules of the LAC in the beamline direction, around $\Theta_{bin} = 15$, the overlap region between the barrel and the endcap LAC, and the deep forward region. Figure 3.17(b) shows the inefficiency of the event selection in the low energy region due to the E_{TOT} cut.

Summary

Table 3.2 is the statistics summary of the three filters for selecting hadronic Z° or tau pair events. 10,437 events remain after all three filter stages.

Filter	Number of Events
KZ0FLT	13,478
KWABID	11,613
KMONOJT	10,437

Table 3.2 Statistics summary of the three filters for the 1992 polarized run. Numbers in the second column are the number of events which passed the filter at each stage.

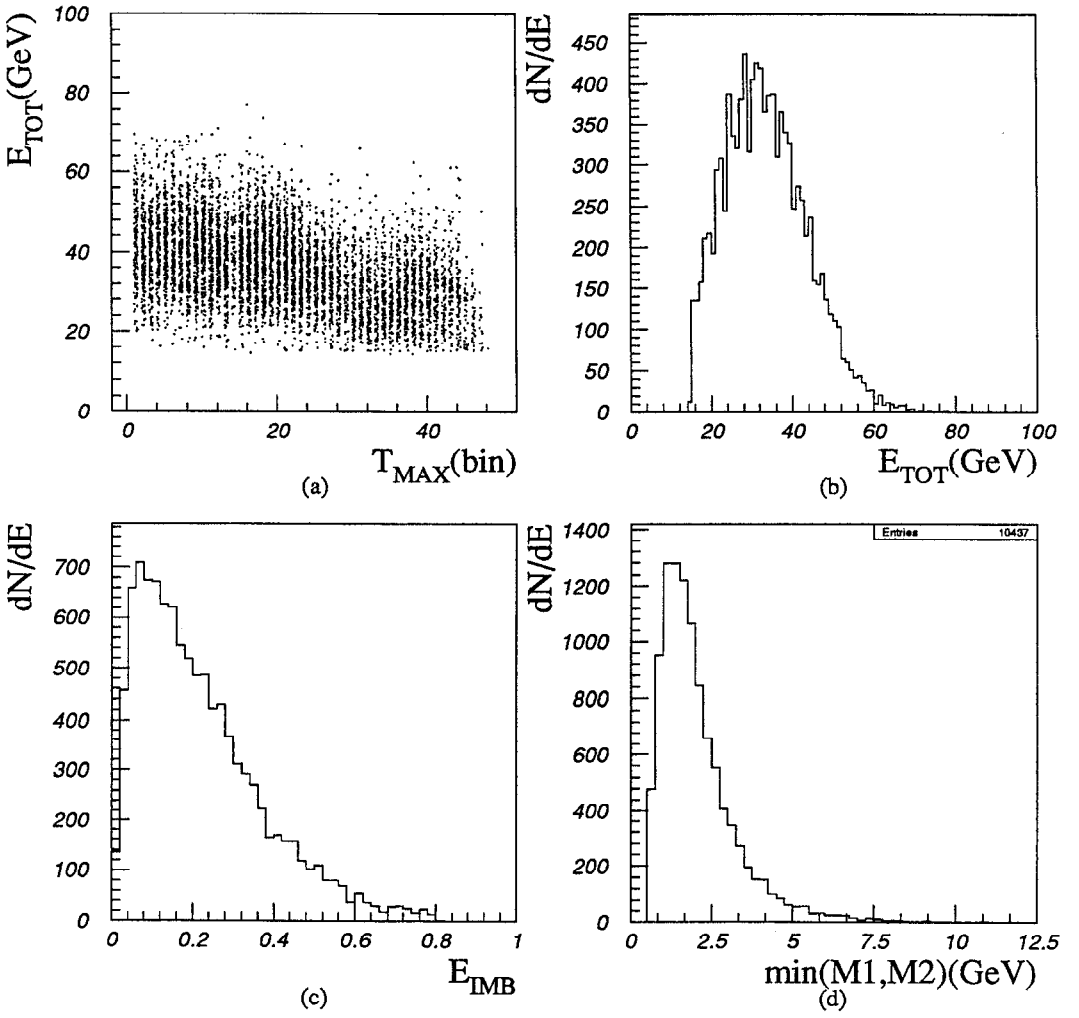

Figure 3.17 (a) is the distribution of the total LAC energy versus Θ_{bin} of the tower having the maximum EM1 energy, (b) is total LAC energy distribution, (c) is the energy imbalance distrbution, (d) is the distribution of the minimum tower energy out of two maximum electromagnetic tower energies for the final selected events.

Background Estimation

Introduction

The background estimation is based on the "double-scanning" technique and uses the "Maximum-likelihood" method. This method was introduced by Evans and Barkas [42] and is applicable even for cases of low statistics. This method also assumes that scans are performed independently using the same event criteria.

Two independent scanners scanned the final event sample by using a three-view event display with information of the LAC tower hits and CDC vectored hits. Each scanned event was classified into event categories by the event criteria which were described in the first introduction of this Chapter.

Let $N1$, $N2$, $N12$, N_{12} and N be as follows:

- $N1$: total number of background events found by a scanner 1
- $N2$: total number of background events found by a scanner 2
- $N12$: total number of background events found by both scanners
- N_{12} : total number of overlapped events by both scanners
- N : total number of background events in the event sample

Since an event is either found or not found by a scanner, the scanning process can be described using binomial statistics. The probability for finding $N1$ out of N events with a scanning probability $P(1)$ is:

$$P_1(N1|N,P(1)) = \frac{N!}{N1!(N-N1)!}[P(1)]^{N1}[1-P(1)]^{N-N1} \qquad (38)$$

In the total number of background events found by the second scanner, there are overlapped events (N_{12}) with the first scanner, and events ($N2 - N_{12}$) which are only found by the second scanner. The probability for finding N_{12} out of $N1$ events

for the second scanner with a scanning probability $P(2)$ is then:

$$P_I(N_{12}|N1, P(2)) = \frac{N1!}{N_{12}!(N1 - N_{12})!}[P(2)]^{N_{12}}[1 - P(2)]^{N1-N_{12}} \tag{39}$$

The probability for finding just $(N2 - N_{12})$ out of $(N - N1)$ events which are not found by the first scanner is:

$$\begin{aligned} P_{II}(N2 - N_{12}|(N - N1), P(2)) \; &= \frac{(N - N1)!}{(N2 - N_{12})!(N - N1 - N2 + N_{12})!} \\ &\quad [P(2)]^{N2-N_{12}}[1 - P(2)]^{N-N1-N2+N_{12}} \end{aligned} \tag{40}$$

The probability for finding $N1$ events by the first scanner, $N2$ events by the second scanner and N_{12} overlapped events by both scanners is given by the product of the above three probabilities:

$$\begin{aligned} P \; &= P(N1, N2, N_{12}|N, P(1), P(2)) \\ &= \frac{N!}{(N - N12)!}[P(1)]^{N1}[P(2)]^{N2}[1 - P(1)]^{N-N1}[1 - P(2)]^{N-N2} \\ &\quad \frac{1}{(N1 - N_{12})!(N2 - N_{12})!N_{12}!} \end{aligned} \tag{41}$$

This probability can be interpreted as the likelihood of the observed values of $N1$, $N2$ and N_{12} for parameters N, P(1) and P(2). The above equation can be intergrated over the parameters P(1) and P(2) to get a likelihood function which has only the single parameter N:

$$\mathcal{L}(N) = \frac{N!(N - N1)!(N - N2)!}{(N - N12)![(N + 1)!]^2} \frac{N1!N2!}{(N1 - N_{12})!(N2 - N_{12})!N_{12}!} \tag{42}$$

This expression can be simplified by a recursive relation of $\mathcal{L}$:

$$\mathcal{L}(N) = \frac{N(N-N1)(N-N2)}{(N-N12)(N+1)^2}\mathcal{L}(N-1) \tag{43}$$

The initial value of $\mathcal{L}(N-1)$ is taken to be $\mathcal{L}(N12) = 1$ because the number N must be at least as large as the number of events found by both scanners. The total number of events is then found by increasing the value of N until the maximum of $\mathcal{L}$ ($\mathcal{L}_{max}$) is obtained.

Results

Table 3.3 shows the scan results of two independent scanners for the 1992 A_{LR} data sample. In Table 3.3 "overlap" means events both scanners classified in the same event category.

Background	Scanner 1	Scanner 2	Overlap
WAB	75	88	49
Beam-Related	71	72	66
Total Background	146	160	115

Table 3.3 Double-scanning results.

By using the above recurrence relation, the likelihood function can be generated with numbers from the scanned results. Figure 3.18 shows the total number of background events in the final data sample with the maximum-likelihood method. The same method was applied to estimate the total number of wide-angle Bhabha and beam-related background events.

Table 3.4 shows the results of the background estimation with errors which were calculated at the 95.4% confidence level, corresponding to $e^{-2}\mathcal{L}_{max}$.

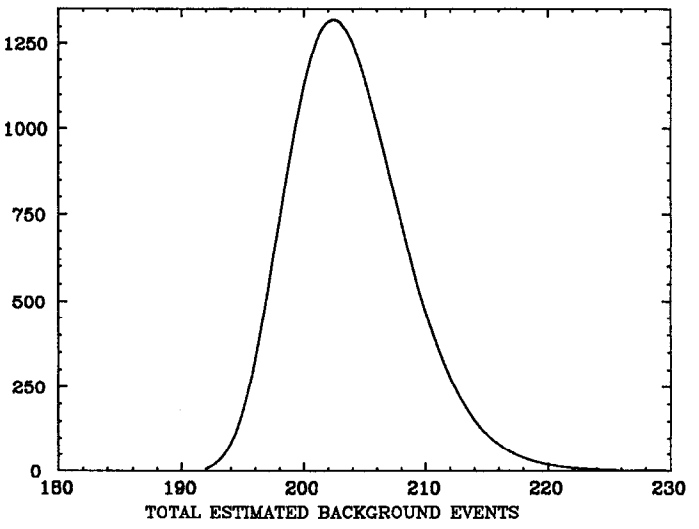

Figure 3.18 Total number of background events in the final data sample based on the maximum-liklihood method.

Background	Estimated number	Fraction in Sample
WAB	133^{+19}_{-12}	1.3%
Beam-Related	80^{+3}_{-0}	0.8%
Total Background	202^{+12}_{-7}	1.9%

Table 3.4 Results of the maximum-likelihood method.

The background events misidentified as hadronic Z° events by the handscan should be considered to estimate additional background. There are two sources for this case: Cosmic-ray and the SLC beam.

The contribution from cosmic-ray backgrounds is negligible due to the total LAC energy and energy imbalance cuts [43]. To estimate the number of background events from beam-related sources, *RANDOM* and *BHABHA* triggered events

were looked at. To find out the probability of seeing a background event which has a good cluster ($E_{TOT} > 5$ GeV) in the opposite hemisphere, 9,099 $RANDOM$-triggered and 25,917 $BHABHA$-triggered events were looked at. Only three events have $E_{TOT} > 5$ GeV in the muonic energy scale. Hence the probability of having an event which has two good clusters in the opposite direction is:

$$\begin{aligned} \text{Mean Probability} &\approx \frac{1}{8}\left(\frac{3}{35,016}\right)^2 \\ &= 9.2 \times 10^{-10} \end{aligned} \tag{44}$$

The factor of 1/8 is required because two clusters should be in opposite octants of the detector for satisfying the energy imbalance cut. For the 1992 polarized run of four months, with 120 Hz repetition rate and 70% SLC uptime [44], the number of beam crossing is about 8.7×10^8. This gives (0.8 ± 0.7) events which are beam-related backgrounds but misidentified as hadronic Z° for the 1992 polarized run. This has a negligible effect for the background estimation.

There are no contributions of backgrounds, which look like hadronic Z° events and are misidentified as hadronic Z°, in the final data sample, from the cosmic-ray and beam-related sources.

It is enough to only consider the numbers in Table 3.4 to estimate the total number of background events in the final data sample. As shown in Table 3.3 the fraction of backgrounds from wide-angle Bhabha and beam-related events is 1.9%. To be conservative, the error for the number of total background events is taken as the sum of the number of the events which one scanner found but the other did not find as the background, instead of taking errors at the 95.4% confidence level. This number can be obtained from Table 3.3 and is 76. The total background in the final data sample is then $1.9 \pm 0.7\%$.

Combined Efficiency of Triggering and Event Selection

The Monte Carlo modelling of the LAC response is not reliable enough to estimate the trigger or event selection efficiencies of hadronic events to the few percent precision required. Instead of estimating efficiency separately, the combined efficiency of triggering and event selection can be made by comparing the number of hadronic Z° events found with the number of small-angle Bhabha events in the luminosity monitor and small angle tagger (LMSAT). The cross sections of hadronic Z° [45] and small-angle Bhabha [46] have been calculated reliably and well measured at LEP [47], respectively.

The ratio of numbers of hadronic Z° to small-angle Bhabha events has a relation with the ratio of cross sections of these processes through the ratio of the combined trigger and selection efficiency for hadronic Z° to those for small-angle Bhabha events [48]:

$$\epsilon_{bgk}\frac{N_{had}}{N_{Bh}} = \frac{\sigma_{had}}{\sigma_{Bh}}\frac{\epsilon_{had}}{\epsilon_{Bh}}\frac{1}{\epsilon_E} \tag{45}$$

where ϵ_{bgk} is the estimated fraction of true hadronic Z° in the final data sample, $N_{had}(N_{Bh})$ is the number of hadronic Z° (small-angle Bhabha) events found by the selection procedure, $\sigma_{had}(\sigma_{Bh})$ is the cross-section of hadronic Z° (small-angle Bhabha), $\epsilon_{had}(\epsilon_{Bh})$ is the combined efficiency of triggering and event selection of hadronic Z° events (small-angle Bhabha events), and ϵ_E [49] is a correction factor for compensation of the effective reduction in cross-section due to non-zero center-of-mass energy spread.

Since Monte Carlo simulation in the LMSAT detector describes the data well, the Bhabha triggering and selection efficiency is reliable and can be used. With the assumption that the Bhabha trigger is independent of the hadronic Z° trigger, the combined efficiency of triggering and event selection is given by the following

relation from the above equation:

$$\epsilon_{had} = \frac{N_{had}}{N_{Bh}} \frac{\sigma_{Bh}}{\sigma_{had}} \epsilon_{Bh} \epsilon_{bgk} \epsilon_E \tag{46}$$

Table 3.5 shows the number of hadronic Z° (including tau pair) and small-angle Bhabha events for several run blocks to consider any time dependence of the triggering.

Run Block	Number of Hadronic Z°	Number of Effective Bhabhas	Ratio
11556 - 11825	753	1,781.5	2.37
12093 - 12430	1,316	2,954	2.24
12456 - 13995	7,306	16,610	2.27

Table 3.5 Run blocks for hadronic Z° and small-angle Bhabha events.

The ratio in Table 3.5 was calculated by N_{Bh}/N_{had} for each run block and the number of effective Bhabhas was calculated by the following relation:

$$N_{Bh} = N_{pre} + \frac{N_{gros}}{2} \tag{47}$$

where N_{pre} is the number of small-angle Bhabha events which have clusters in each hemisphere in the "precise" fiducial region and N_{gros} is the number of small-angle Bhabha events which have at least one cluster in each hemisphere outside this fiducial region. The fiducial region in the LMSAT is defined as the region from the second to fourth towers outward in polar angle from the beamline. Runs 11978–12089 and 12431–12455 were excluded in Table 3.5 because the SLC interaction point was shifted and because of a luminosity monitor data acquisiton problem, respectively.

Quantity	Value
N_{had}	9375 ± 97
N_{Bh}	21345 ± 146
σ_{had}	29.5 ± 0.4 nb
σ_{Bh}	$67.9 \pm 0.5 \pm 0.7$ nb
ϵ_{Bh}	0.9 ± 0.01
ϵ_E	1.03 ± 0.01
ϵ_{bgk}	0.96 ± 0.005

Table 3.6 Numerical values used for the combined efficiency.

Table 3.6 shows the numerical values which were used for calculating the combined efficiency of triggering and event selection of hadronic Z°. Here tau events were estimated to be 2% of the data sample and backgrounds from wide-angle Bhabha and beam-related events were estimated to be 2% of the data sample. The combined efficiency of triggering and selection for hadronic Z° is:

$$\epsilon_{had} = (90.0 \pm 2.5)\% \tag{48}$$

Figure 3.19 shows the distribution of $|\cos\theta|$ of the thrust axis of the final data sample. Figure 3.20 is the distribution of the efficiency as a function of the $|\cos\theta|$ of the thrust axis and it shows that the efficiency in the overlap region drops and the efficiency in the deep forward region is not better than 50%. The average combined efficiency of triggering and selection for the barrel region is better than 95%.

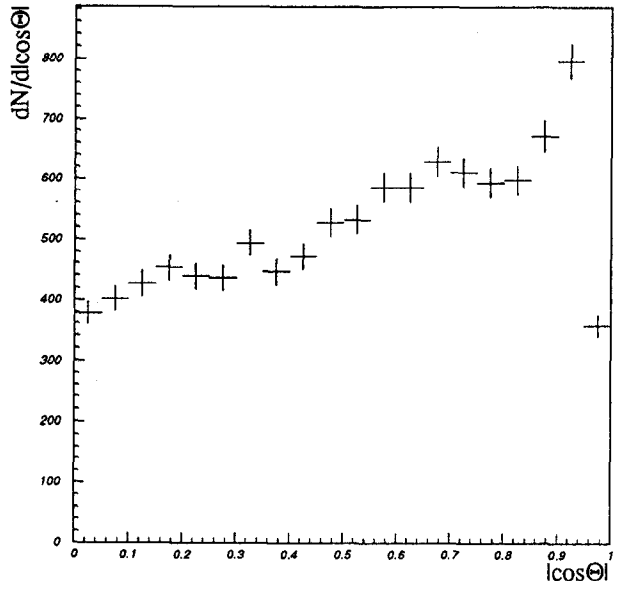

Figure 3.19 Uncorrected angular distribution of the final sample events.

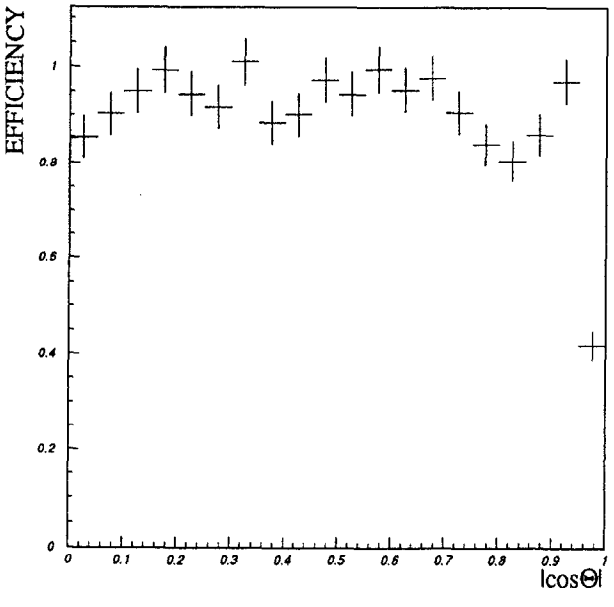

Figure 3.20 Efficiency distribution of the LAC.

CHAPTER IV

POLARIZATION MEASUREMENT

Introduction

Since the magnitude of the polarization of the electron beam is not purely left- or right-handed in the experiment, we do not measure the left-right cross section asymmetry (A_{LR}) directly, but the measured left-right cross section asymmetry ($A_{LR}^{\rm mea}$). The $A_{LR}^{\rm mea}$ has a relationship with the A_{LR} by the following equation:

$$A_{LR}^{\rm mea} = \mathcal{P} A_{LR} \tag{49}$$

where $\mathcal{P}$ is the measured polarization of the longitudinally polarized electron beam. It is required to measure the electron beam polarization very accurately to provide a precise measurement of A_{LR}.

$A_{LR}^{\rm mea}$ is measured in the experiment by:

$$A_{LR}^{\rm mea} = \frac{N_L(\mathcal{P}) - N_R(\mathcal{P})}{N_L(\mathcal{P}) + N_R(\mathcal{P})} \tag{50}$$

where N_L (N_R) is the number of detected Z° events with left- (right-) handed polarized electron beam. From Eqs. (16), (49) and (50) A_{LR} is given by

$$A_{LR} = \frac{(\frac{N_L - N_L^{bgk}}{\epsilon_L \mathcal{L}_L}) - (\frac{N_R - N_R^{bgk}}{\epsilon_R \mathcal{L}_R})}{\mathcal{P}_R(\frac{N_L - N_L^{bgk}}{\epsilon_L \mathcal{L}_L}) + \mathcal{P}_L(\frac{N_R - N_R^{bgk}}{\epsilon_R \mathcal{L}_R})} \tag{51}$$

with the following definitions:

$$\begin{aligned} N^{bgk}_{L/R} &= N^{bgk} \pm \frac{\delta N^{bgk}}{2} \\ \mathcal{L}_{L/R} &= \mathcal{L} \pm \frac{\delta \mathcal{L}}{2} \\ \epsilon_{L/R} &= \epsilon \pm \frac{\delta \epsilon}{2} \\ \mathcal{P}_{L/R} &= \mathcal{P} \pm \frac{\delta \mathcal{P}}{2} \end{aligned} \tag{52}$$

where $N_{L/R}$ is the number of detected Z° events, $N^{bgk}_{L/R}$ is the number of background events in data sample, $\mathcal{L}_{L/R}$ is the integrated luminosity, $\epsilon_{L/R}$ is the average detection efficiency, and $\mathcal{P}_{L/R}$ is the average beam polarization for left- and right-handed polarized electron beam. From the above two equations, A_{LR} is given to first order in the errors by:

$$A_{LR} = \frac{A^{\rm mea}_{LR}}{\mathcal{P}}[1 - \frac{2N^{bgk}}{N} + (A^{\rm mea}_{LR} - \frac{1}{A^{\rm mea}_{LR}})(\frac{\delta \mathcal{L}}{2\mathcal{L}} + \frac{\delta \epsilon}{2\epsilon}) + A^{\rm mea}_{LR}\frac{\delta \mathcal{P}}{2\mathcal{P}}] \tag{53}$$

When the beam polarization measurement is the dominant source of systematic error, which is our case, we can write that the total measurement error in the A_{LR} measurement as:

$$\delta A_{LR} = \sqrt{\frac{1}{\mathcal{P}^2}\frac{1}{N_Z}(1 - \mathcal{P}^2 A^2_{LR}) + A^2_{LR}(\frac{\delta \mathcal{P}}{\mathcal{P}})^2} \tag{54}$$

The first and second terms are the statistical and the systematic errors, respectively. Since the A_{LR} measurement is the ratio of the cross section difference to the Z° production rate, most beam related systematic effects are cancelled.

Measurement of the Compton Laser Polarization

The Laser Polarization Measurement

The polarization of the Compton laser source (CLS) at the Compton interaction point (CIP) was measured before and after runs by measuring transmitted light intensities. A linear polarizer was inserted into the circularly polarized laser beam and the transmitted maximum and minimum light intensities were measured with a photodiode by rotating the linear polarizer. The magnitude of the circular polarization of the CLS is then given by the following equation:

$$\mathcal{P}_\gamma = \frac{2\sqrt{I_{\min} + I_{\max}}}{I_{\min} + I_{\max}} \tag{55}$$

where $\mathcal{P}_\gamma$ is the polarization of the CLS and $I_{\min}$ ($I_{\max}$) is the minimum (maximum) transmitted intensity of the CLS.

The systematic error in the laser polarization measurement comes from the uncertainties in the alignment of the polarizer in the laser beam. Since the average maximum and minimum transmitted intensities were used for the polarization values, the spread of the different values of $I_{\max}$ and $I_{\min}$ for different orientations of the polarizer gave different polarization values and was considered to be the systematic error. The systematic error was found to be of the order of 1%.

Figure 4.1 shows the hardware setup of the polarization monitoring on the CLS bench and Figure 4.2 shows the spread of the laser polarization values from the laser bench monitor. The spread in the laser polarization values, which comes from Pockels cell misalignments or incorrect Pockels cell voltage settings, was monitored with the prism and the pair of joule-meters on the CLS bench.

Since the polarization values were not corrected for this spread and $\sigma = 0.8\%$ in the measurement, this effect was considered as an additional systematic error of 1%. The statistical error in the polarization measurements was about 0.1% which

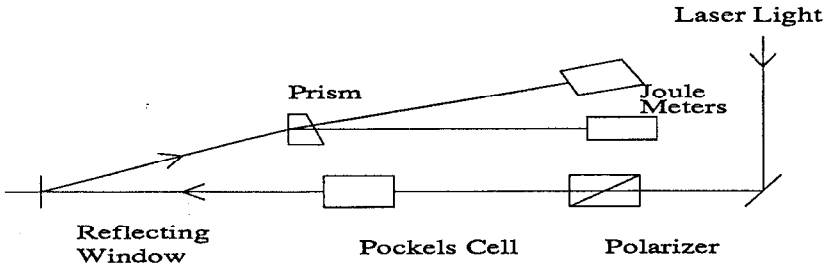

Figure 4.1 A schematic diagram of the Compton laser polarization monitor on the Compton laser bench.

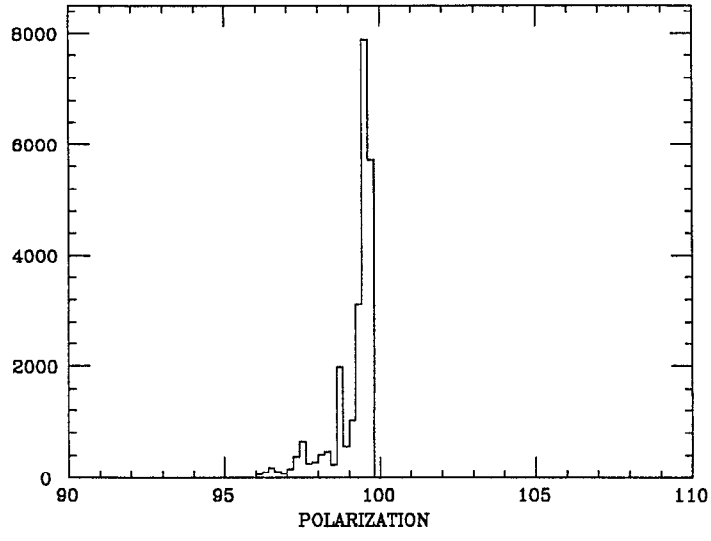

Figure 4.2 The distribution of the Compton laser polarization on the Compton laser bench.

is negligible. The circular polarization of the Compton laser light was measured to be

$$\mathcal{P}_\gamma = (93 \pm 2)\% \tag{56}$$

Even though the laser polarization was measured as ≈99% just before the Vaccum Transport Line (VTL), which takes the laser beam from laser shack to the SLC tunnel, it was observed that the laser polarization dropped after the VTL exit window and further dropped at the CIP after passing through the steering lens.

The Photon Helicity

Positive and negative high voltages on the Pockels cell on the laser bench produce right- and left-handed circularly polarized laser light, respectively. The helicities of the laser beam were checked by comparing results from the "Fresnel setup", which is based on the total internal reflection technique, with those from "Pockels setup" [50]. Figure 4.3 shows the Pockels cell setup on the CLS bench with quarter-wave plate and Figure 4.4 shows the Fresnel setup using the Fresnel prisms on the CLS bench. The Fresnel setup is based on the fact that the parallel and perpendicular components, which are relative to the reflection plane, of linear polarization at 45° incident angle undergo different phase shifts after total internal reflection:

$$\tan\frac{\delta}{2} = -\frac{\cos\theta}{\sin^2\theta}(\sin^2\theta - \frac{1}{n^2}) \tag{57}$$

where θ is the incident angle, n is the refractive index of the Fresnel prism, and δ is the relative phase shift, which is the phase shift difference between the perpendicular and parallel components. About a 90° phase shift can be achieved and right-handed circularly polarized light is produced by the Fresnel setup. It

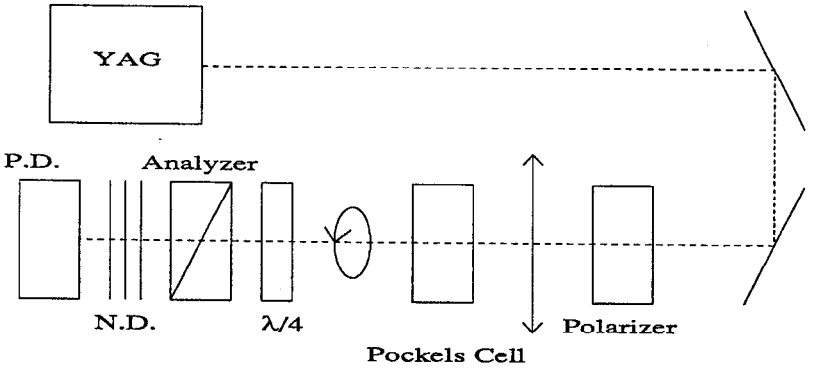

Figure 4.3 A schematic diagram of the Pockels cell setup on the Compton laser bench.

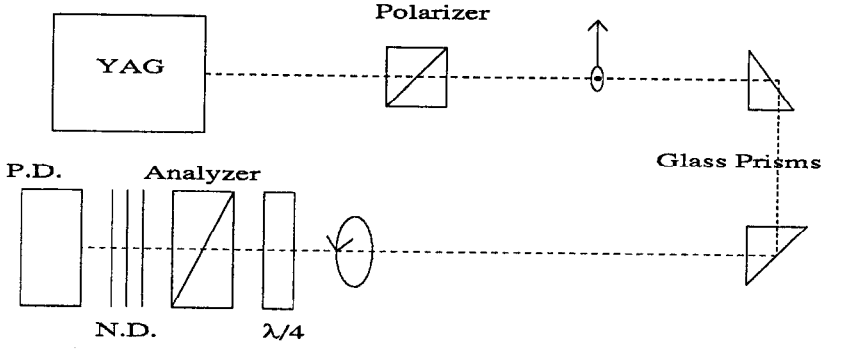

Figure 4.4 A schematic diagram of the Fresnel prisms setup on the Compton laser bench.

was confirmed that the positive high voltage setting on the Pockels cell gives the quarter-wave plate settings consistent with those by the Fresnel setup.

Measurement of the Electron Beam Polarization

The Electron Polarization Measurement

The helicity of the electron beam is randomly flipped on a pulse-to-pulse basis at the 120 Hz SLC frequency by changing the helicity of the polarized light source (PLS) laser. The Čerenkov detector is used to measure the magnitude of the electron beam polarization. The Čerenkov detector, based on Compton scattering, measures the raw asymmetry in each Čerenkov channel. The electron beam polarization ($\mathcal{P}_e$) was measured from the Čerenkov raw asymmetry measurement (A_i) and Compton laser polarization ($\mathcal{P}_\gamma$) with the analyzing power (α_i) of channel i:

$$\mathcal{P}_e = \frac{A_i}{\mathcal{P}_\gamma \alpha_i} \tag{58}$$

where α_i, the analyzing power, is the average Compton asymmetry for the channel i weighted by the unpolarized Compton cross section and the EGS simulated detector response function. Since the scattered electrons are separated from the unscattered electrons by a pair of analyzing bend magnets and there is a direct correspondence between the scattering angle in the center-of-mass frame and the energy of the final state particles in the laboratory frame with the Compton scattering, the raw asymmetry dependence of the scattering angle in the center-of-mass frame (A_θ) can be replaced by the raw asymmetry dependence of the detector position from the beamline in the transverse direction (A_x). Figure 4.5 shows the dependence of the unpolarized Compton cross section and the Compton asymmetry at a distance of 355.8 cm from the bend magnets.

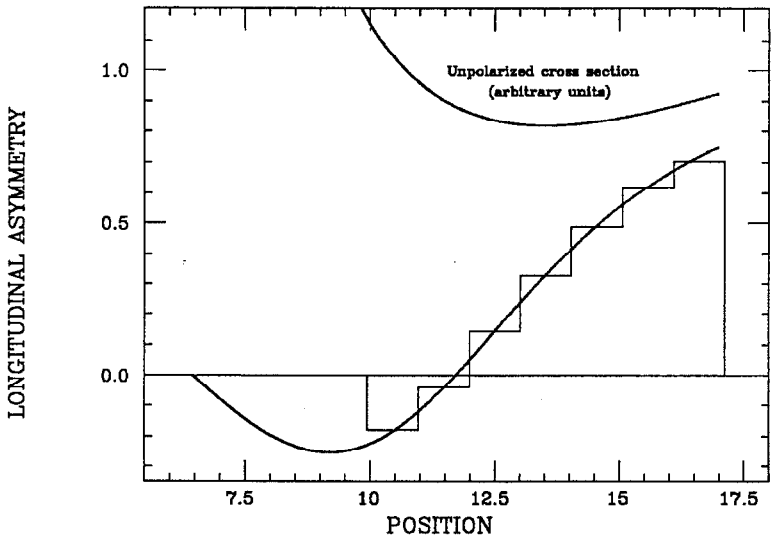

Figure 4.5 The dependence of the unpolarized Compton cross section and Compton asymmetry on the distance (cm) from the beamline in the transverse direction.

Since the largest asymmetry occurs at 17.4 GeV and the zero-asymmetry occurs at 25.2 GeV of the scattered electron energy, and the detector accepts electrons in the momentum range of 17-30 GeV, these two points were used for calibrating the detector. Since the dectector is mounted on a table which can be moved transverse to the beamline, the detector was moved to find the location of the Compton kinematic edge relative to the channel edges. Channel 6 is the outermost channel fully illuminated by the scattered Compton electrons and Figure 4.6 shows the result of the endpoint scan. The kinematic endpoint from the outer edge of channel 6 for the nominal table is 0.86 cm, which corresponds to 3.7 mm from the center of channel 7. The uncertainty in the measurement of the endpoint scan was 0.3 mm. This corresponds to 0.49% and 0.18% uncertainties in the analyzing powers of channels 6 and 7, respectively. There are channel-to-channel statistical correlations due to laser beam fluctuation. Since the pulse-by-pulse Compton data in the 1992

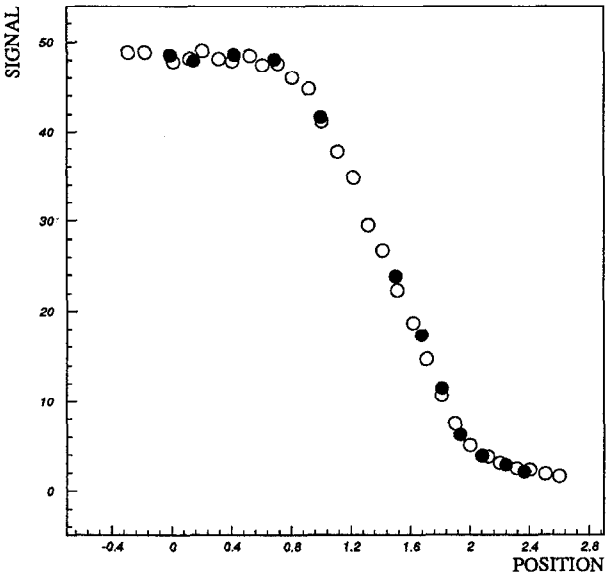

Figure 4.6 Result of an endpoint scan for channel 6. The position shown is the detector position from nominal in cm unit. Open circles and filled circles are for EGS simulation and data, respectively.

run is not available, there is no information of this correlation. Therefore, a single channel measurement was used for the polarization measurement. 742 out of 10224 events in the final data sample used channel 6 and the rest of events used channel 7 for the polarization measurement. The final event selection which is associated with the polarization measurement is described in the next chapter. It gives an uncertainty in the polarization measurement of 0.2%.

For finding the location of the zero-asymmetry point, the asymmetry measurement in channels 2 and 3, which straddle the zero-asymmetry point, were used:

$$A_o = \mid \frac{A_2}{A_3 - A_2} \mid \tag{59}$$

where A_2 and A_3 are the raw asymmetries of channel 2 and 3, respectively. The average A_o is 0.22 ± 0.01 and this measurement gives the distance from the zero

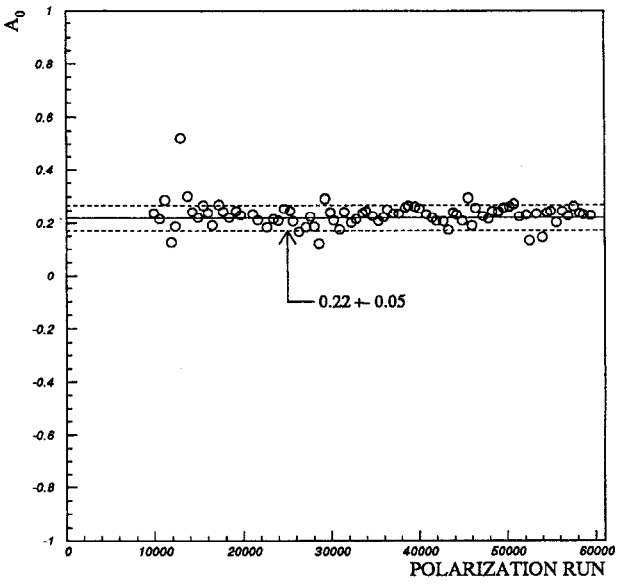

Figure 4.7 A_0 measurement of the polarimeter runs for monitoring the time dependence of the position of the zero-asymmetry point.

asymmetry point to the center of channel 2 as approximately 22% of one channel width, which is 1cm. Simluation shows that there is 0.01 cm shift in A_0 away from the undeflected beamline, which comes from the cross section, showering and nonlinearity of the asymmetry function. This gives 0.23 cm distance between the zero-asymmetry point and the center of channel 2. Since channels 6 and 7 are close to the well-measured endpoint, the analyzing powers of these channels are insensitive to the measurement of the zero-asymmetry point. In other words, there is no uncertainty coming from the zero-asymmetry point measurement on the analyzing powers of channels 6 and 7.

Figure 4.7 shows the monitoring of A_0 for the time dependence of the zero-asymmetry point of the polarimeter runs. Since the zero-asymmetry point is stable and channels 6 and 7 are insensitive to motion of the zero-asymmetry point, there

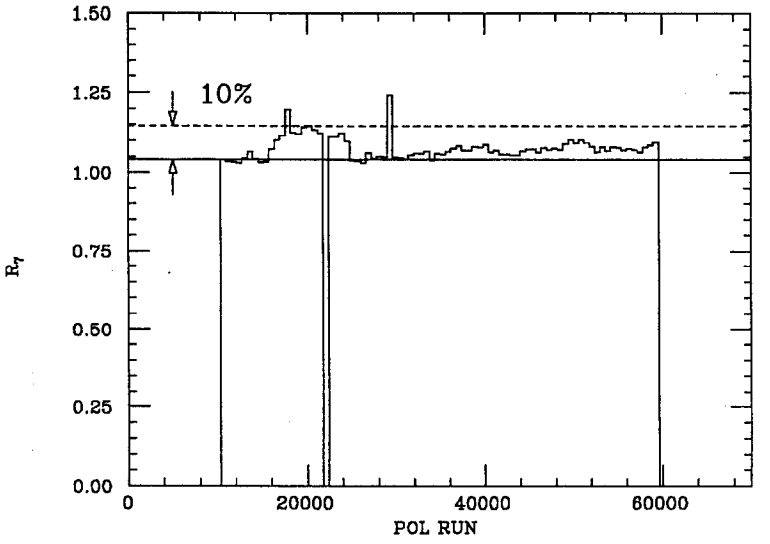

Figure 4.8 Ratio of signals of detector channel 7 to channel 2 for monitoring the time dependence of the detector calibration.

is no systematic error which comes from the time dependence.

From the measurement of $R_7 = S_7/S_2$ the time dependence of the endpoint was checked. Here S_7 (S_2) is the mean signal of channel 7 (2) after backgrounds are subtracted. The spike around run 30,000 comes from a gain change for a linearity test and the large digression between runs 15,000 and 25,000 comes from lowered phototube voltages due to an increased Compton luminosity [51]. With this understanding, the difference between the R_7 and the observed signal differences is less than 10%, corresponding to 1 mm of motion in the endpoint. The largest digression in R_7 corresponds to less than 0.5 mm for the endpoint. That is, the endpoint is constrained to be within 0.25 mm of the position derived from the endpoint scan. This provides an additional systematic error which is almost the same as the endpoint scan calibration and it is ascribed as an 0.2% uncertainty in the polarization measurement. There is a total 0.4% uncertainty in the polariza-

tion measurement due to the detector calibration and the time dependence of the calibration.

Shifts in the Compton asymmetry measurement can come from many effects such as nonlinearity of the phototubes, ADC response, and background biases for different phototube pulse heights. The R1398 phototube base was designed by the Berkeley group to give a linear response for photoelectron fluxes from the photocathode. The effects were studied by changing the phototube gain with the front-end voltage while fixing the back-end voltage at 600 volts in the phototube base.

Figures 4.9 and 4.10 show the relative measured asymmetry versus the phototube pulse heights for channels 6 and 7, respectively. It shows both channels are saturated from 300 ADC counts, corresponding to 1.0 volt pulse height. In the 1992 polarized run the typical pulse heights were 80−150 ADC counts for most of the data.

In order to study the detailed behavior in the unsaturated region below 200 ADC counts, the polarized electron beam data collected with constant tube voltages was used. The Proportional Tube Detector (PTD) pulse height range was divided into four bins and the Čerenkov response was measured across almost the entire range of the observed pulse heights for each PTD pulse height bin. This is possible because the background of the Čerenkov is different from that of the PTD. Thus, the PTD and the Čerenkov pulse heights are only partially correlated for whole runs, and so the Čerenkov asymmetry can be normalized to those of the PTD in a way which is unbiased by the PTD nonlinearity.

Figures 4.11 and 4.12 show the relative asymmetry as a function of the pulse heights for channels 6 and 7, respectively, in the well-defined unsaturated region. All combined nonlinearity effects for pulses between 50 and 150 ADC counts are less than 1% and the pulses outside of this region used the information from Figure

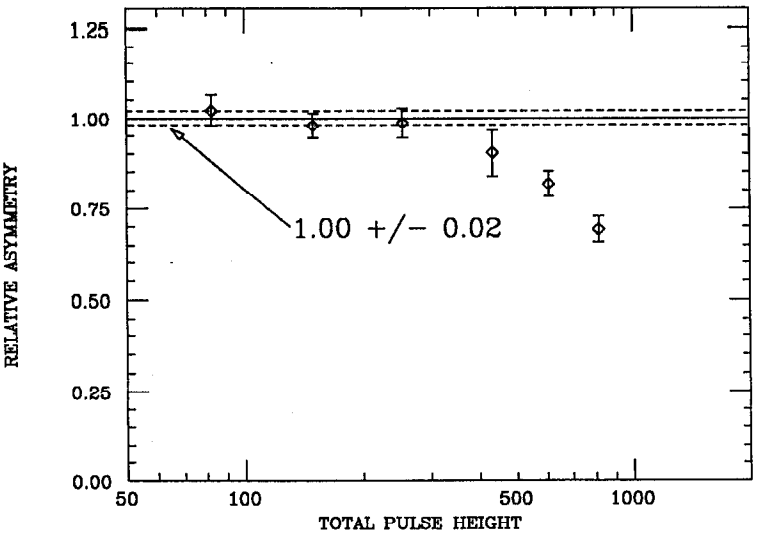

Figure 4.9 The measured relative asymmetry as a function of the phototube pulse heights for channel 6.

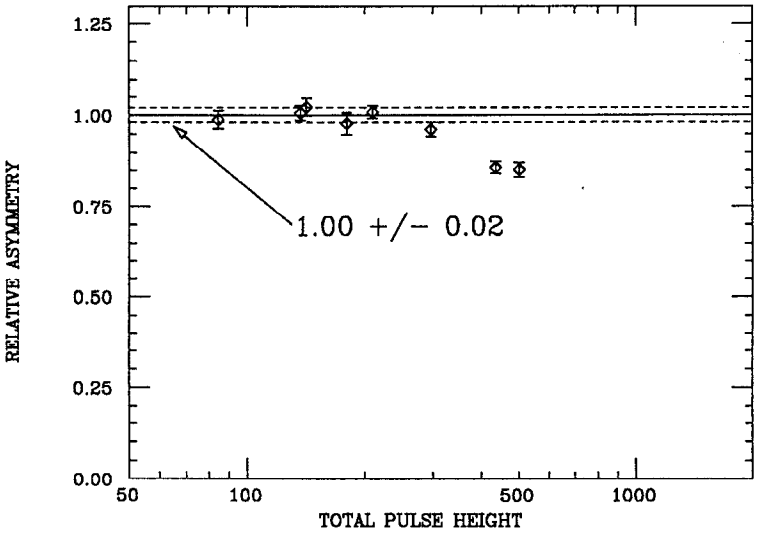

Figure 4.10 The measured relative asymmetry as a function of the phototube pulse heights for channel 7.

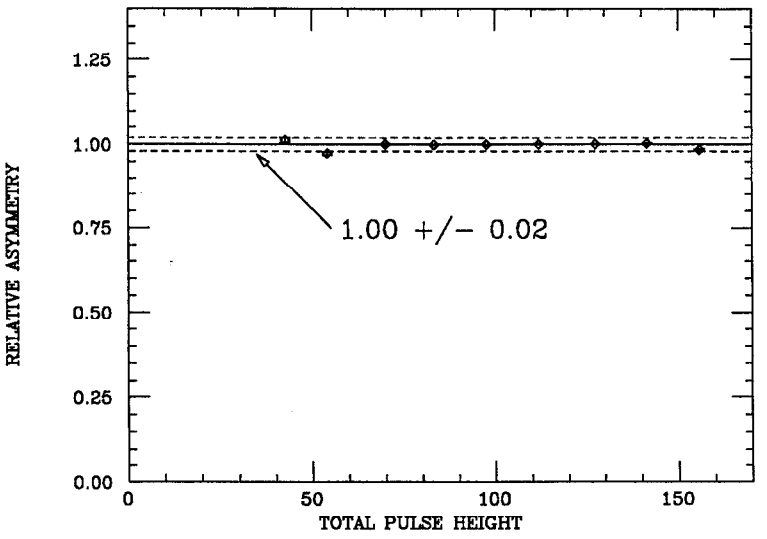

Figure 4.11 The measured relative asymmetry as a function of the phototube pulse heights for channel 6 in the well-defined unsaturated region.

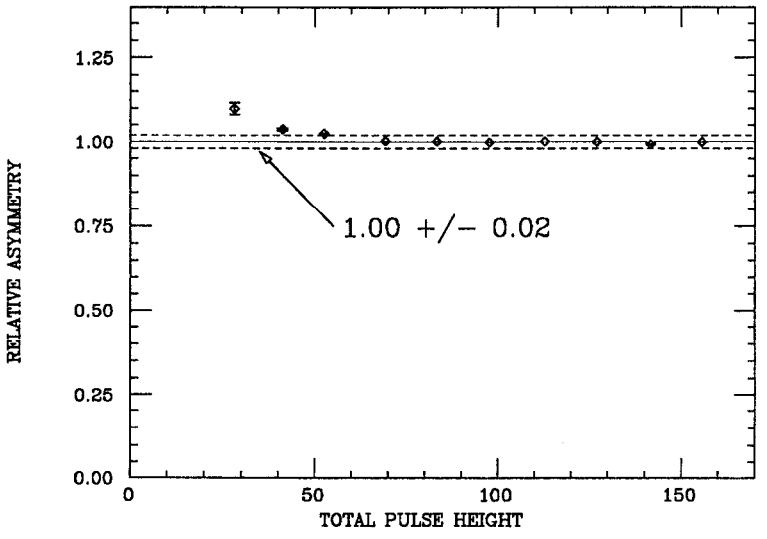

Figure 4.12 The measured relative asymmetry as a function of the phototube pulse heights for channel 7 in the well-defined unsaturated region.

Čerenkov Channel	a_i	A_i	a_i/a_7	A_i/A_7
1	−0.1794	−0.0375	−0.2552	−0.2577
2	−0.0402	−0.0082	−0.0572	−0.0566
3	0.1422	0.0275	0.2023	0.1899
4	0.3262	0.0681	0.4642	0.4677
5	0.4877	0.1020	0.6940	0.7011
6	0.6154	0.1285	0.8758	0.8833
7	0.7027	0.1455	1.0000	1.0000

Table 4.1 The lead-in calculated analyzing powers and the average measured raw asymmetries.

4.9 and 4.10 for correcting the nonlinearities. We ascribed a conservative systematic error on the order of the size of the correction, and it gives 1.5% systematic uncertainty in the polarization measurement from the detector linearity.

There are two different kinds of the electronic cross-talk. When the Compton laser fired without beams, about 0.5−1.0 ADC counts were observed due to pick-up of the laser firing. We ascribe 0.3 ADC counts uncertainty in the measurement and this gives a systematic uncertainty $0.3/S_i$, where S_i is the ith Čerenkov channel signal. For a typical run S_i is about 100 ADC counts and this effect gives 0.3% uncertainty in the polarization measurement.

For the cross-talk due to channel correlations, it was checked by turning off all channels but one in HV. It gives about 0.3 ADC counts per volt. Since one volt corresponds to 300 ADC counts, the effect of channel-to-channel cross-talk gives 0.1% uncertainty in the polarization measurement. Thus, there are 0.4% uncertainties in the polarization measurement from this electronic cross-talk.

Systematic Error	Contribution ($\delta A_{LR}/A_{LR}$)
Laser Polarization	2%
Calibration	0.4%
Linearity	1.5%
interchannel consistency	0.9%
Electronic croos-talk	0.4%
Polarization Measurement	2.7%

Table 4.2 Systematic Uncertainties from the polarization measurement.

Table 4.1 shows the calculated analyzing powers for the calibration derived from the edge scan and zero-point asymmetry determination with correction from the EGS simulation, and the average measured raw asymmetries for each Čerenkov channel. The analyzing powers were corrected for detector resolution and acceptance using the EGS simulation. Columns 3 and 4 show the normalized analyzing powers and the measured asymmetries to channel 7. The difference of 0.008 between the expected and measured asymmetry ratio of channels 6 and 7 corresponds to a difference in the measured mean polarization of $\delta\mathcal{P}/\mathcal{P} = 0.009$. Since this discrepancy was not understood, this was included as an additional systematic error. It gives 0.9% systematic uncertainty in the polariztion measurement.

Table 4.2 shows the systematic errors in the A_{LR} measurement which come from the detector contribution to the polarization measurement. Figure 4.13 shows the average measured Compton asymmetry for each channel along with the predicted asymmtery with the assumption of the Compton laser polarization of 93%. The average electron beam polarization is 22.4%.

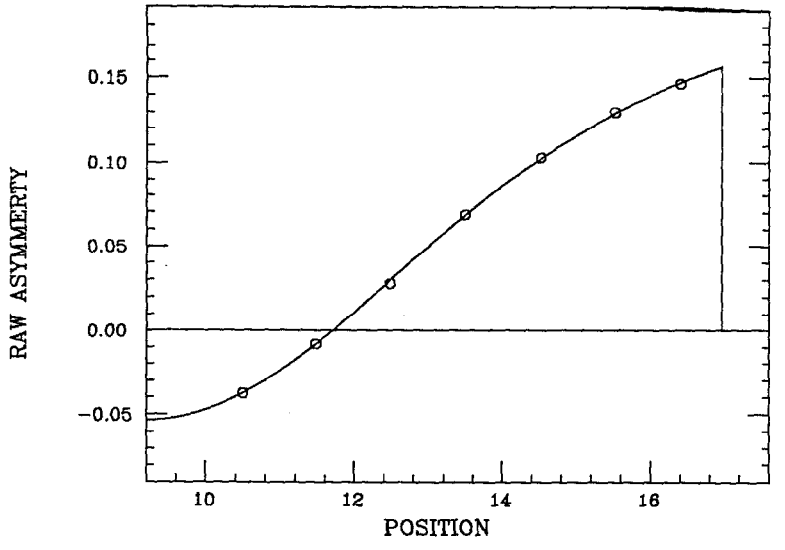

Figure 4.13 Average measured Compton asymmetry over the data sample in the detector for seven Čerenkov channels versus the distance from the beamline in the transverse direction (cm). The Compton asymmetry function is fit to data using the normalization factor $\mathcal{P}_\gamma \mathcal{P}_e$.

The Electron Beam Helicity

The positive and negative high voltages on the Pockels cell on the polarized electron source produce right-handed and left-handed circularly polarized laser light, respectively. The helicities of the electron beam were predicted from this determination and the knowledge of the spin dynamics of GaAs. The right-hand polarized electron beam is produced by right-handed laser light. Voltage sign bits of the Pockels cell in the polarized electron source were sent to the Klystron Veto Module (KVM) data stream and the SLD CAMAC directly. These bits give the helicity information of the longitudinally polarized electron beam for a given beam pulse.

The helicity sign of the electron beam polarization was checked with the sign of the Compton scattering cross section by the Compton polarimeter and the helicity

of the Compton laser polarization. It was confirmed that the scattering cross section of $J_z = 3/2$ is larger than that of $J_z = 1/2$ in Compton scattering [52]. The cross section of the spin parallel is larger than that of anti-parallel in Compton scattering. The helicity of the electron beam was therefore checked by measuring the sign of the Compton asymmetry with the Čerenkov detector for both laser polarizations:

$$A_{e(L/R)} = \frac{N_{e(L/R)\gamma(R)} - N_{e(L/R)\gamma(L)}}{N_{e(L/R)\gamma(R)} + N_{e(L/R)\gamma(L)}} \tag{60}$$

The sign of A_e is positive or negative for left-hand or right-hand polarized electron beam, respectively.

CHAPTER V

ANALYSIS and RESULT

Introduction

The polarization measurement of the electron beam was based on the single channel measurement in the 1992 analysis. As long as channel 7 was active, it was used and otherwise, channel 6 was used for the polarization measurement. The absolute statistical error in the single polarization measurement is $\delta\mathcal{P}_e \sim 0.8\%$ since the polarimeter runs continually for three minutes at 11 H_Z.

As mentioned in the previous chapter, there are redundant paths for synchronization of the beam helicity with the SLD data acquisition, which are the polarization bits from the Klystron Veto Module (KVM) and the direct-line to a SLD CAMAC crate (MACH). The beam helicities were checked for the redundant paths and any events which had inconsistent beam helicities for the redundant paths were discarded from the final data sample. 120 out of 10,437 filter-passed events had different beam helicities for the two paths and were discarded from the final data sample.

In order to get reliable polarization values, only good polarization runs were used and the time of the produced Z° event was compared with that of the polarization measurement performed. To be considered as a good polarization run, it was required that the mean raw signal of the channel be greater than 35 ADC counts, the background subtracted signal be greater than 5 ADC counts, there be more than 5 laser pulses for each laser and electron polarization helicity combination, the laser bench joulemeter asymmetry be greater than 0.5, and there be

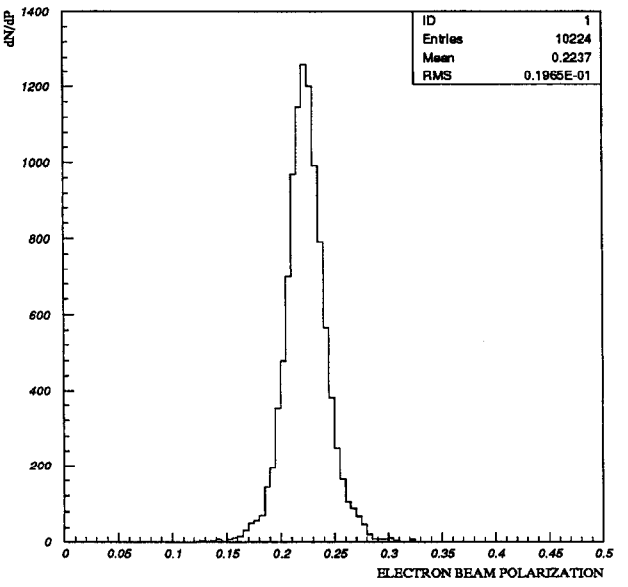

Figure 5.1 The distribution of the electron beam polarization of the final data sample.

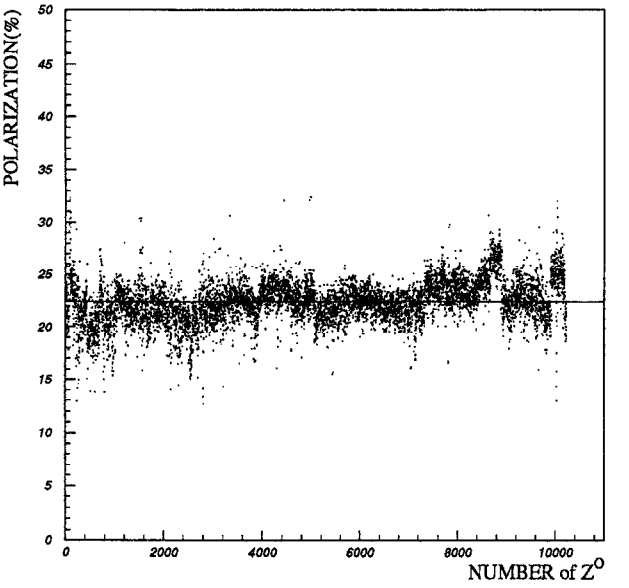

Figure 5.2 The time dependence of the electron beam polarization measurement. The solid line shown is the luminosity weighted average polarization value.

less than 5% uncertainty in the measured raw asymmetry. The events which had more than an hour in time separation between polarization run and Z° event were discarded, and the 10,224 remaining events were used for the A_{LR} measurement of the 1992 polarized run.

Figure 5.1 shows the polarization distribution of 10,224 events in the final data sample. The average luminosity weighted polarization was:

$$\langle \mathcal{P} \rangle \;=\; (22.4 \pm 0.6)\% \tag{61}$$

where the uncertainty is the systematic error in the polarization measurement. Figure 5.2 shows the run number ordered by time of detection versus measured electron beam polarization.

The A_{LR} Measurement

5,226 out of 10,224 events were produced with left-hand polarized electron beam and 4,998 events were produced with the right-hand polarized electron beam. From Eq. (50), the $A_{LR}^{\rm mea}$ is:

$$\begin{aligned} A_{LR}^{\rm mea} =& \frac{(5226 - 4998)}{10224} \\ =& (2.23 \pm 0.99) \times 10^{-2} \end{aligned} \tag{62}$$

where 0.99×10^{-2} is the statistical error. The left-right cross section asymmetry is then determined from the average luminosity weighted polarization value and the measured left-right cross section asymmetry:

$$\begin{aligned} A_{LR} =& \frac{A_{LR}^{\rm mea}}{\mathcal{P}} \\ =& \; 0.100 \pm 0.044(\text{stat.}) \end{aligned} \tag{63}$$

Corrections to A_{LR}

When we account for effects of polarization and beam energy correlated systematics, Eq. (53) is given by the following relation:

$$A_{LR} = \frac{A_{LR}^{\rm mea}}{\mathcal{P}} + \frac{1}{\mathcal{P}}[A_{LR}^{\rm mea}\delta f_b + (A_{LR}^{\rm mea})^2 A_{\mathcal{P}} - E_{cm}\frac{\sigma'(E_{cm})}{\sigma(E_{cm})}A_E - A_\epsilon - A_{\mathcal{L}}] \quad (64)$$

where δf_b is the background fraction in the final data sample, $\sigma(E_{cm})$ is the unpolarized Z° cross section at the center-of-mass energy E_{cm}, $\sigma'(E_{cm})$ is the derivative of the cross section with respect to the center-of-mass energy E_{cm}, $A_{\mathcal{P}}$ is the left-right asymmetry of the electron beam polarization, A_E is the left-right asymmetry of the center-of-mass energy, A_ϵ is the left-right asymmetry of the product of the SLD detector acceptance and efficiency, $A_{\mathcal{L}}$ is the left-right asymmetry of the integrated luminosity.

Backgrounds

Since the effect of backgrounds in the final data sample is a dilution of the observed asymmetry, the contribution of the backgrounds in the A_{LR} measurement should be considered. In Chapter 3, it was estimated that there are 1.9% of beam-related and wide-angle Bhabha backgrounds in the A_{LR} data sample. This gives a 0.2% correction in the A_{LR} value. The uncertainty of the background estimation was 0.7% and will be considered in the systematic uncertainty.

We expect a zero left-right cross section asymmetry for the backgrounds and we looked at the background events, which were observed as backgrounds in Chapter 3, as a consistency check. 12 out of 192 events were discarded due to inconsistent polarization bits in the redundant paths and due to the time comparision cut. 97 of the remaining 180 background events were produced with left-handed polarized electron beam and 83 events were produced with the right-handed polarized

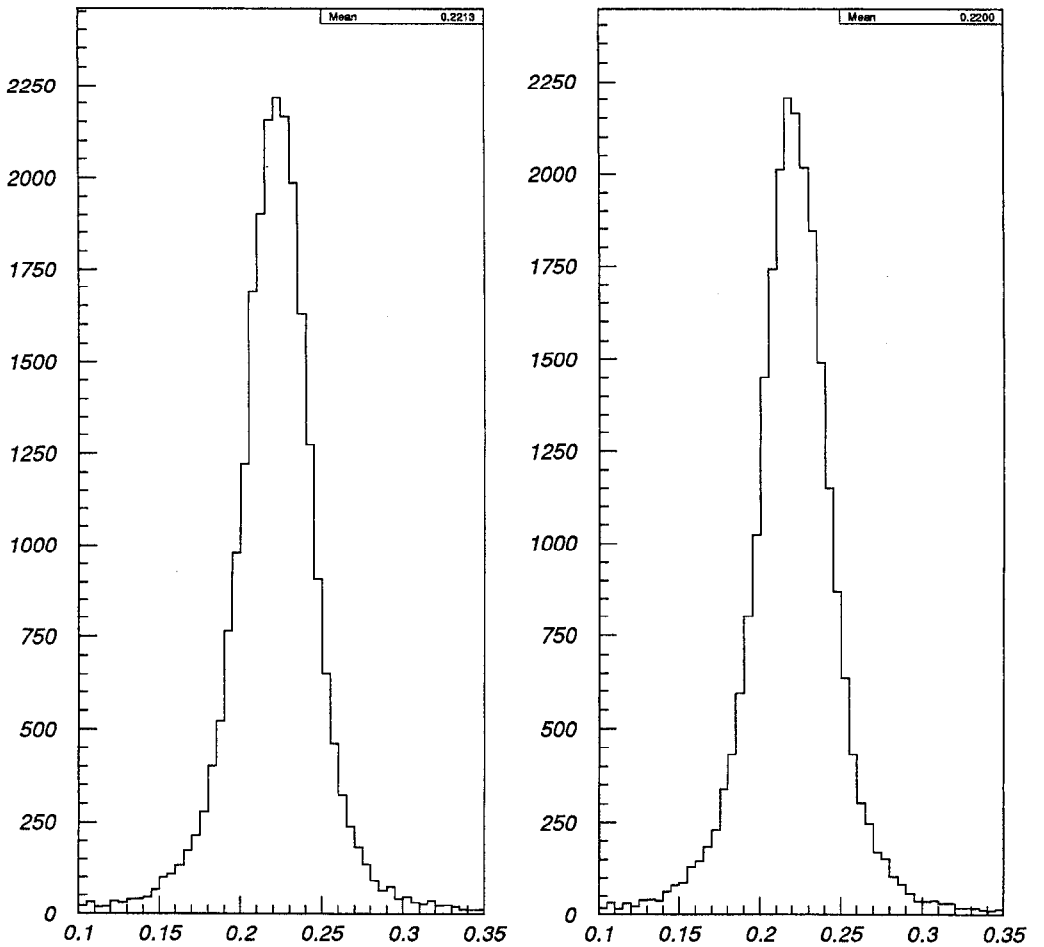

Figure 5.3 The polarization distributions (%) of left-hand and right-handed polarized electron beam.

electron beam. It gives $A_{LR_{\rm bgk}}^{\rm mea} = 0.078 \pm 0.074$, which is consistent with zero asymmetry within the statistical error.

Polarization Asymmetry

The polarization asymmetry is measured by comparing mean polarizations for the left- and the right-handed polarized electron beams. Figure 5.3 shows the polarization distribution over the whole 1992 polarization run for left- and right-handed polarized electron beams.

The polarization asymmetry for the left- and right-handed polarized electron beam is then:

$$\begin{aligned} A_{\mathcal{P}} &= \frac{(\mathcal{P}_L - \mathcal{P}_R)}{(\mathcal{P}_L + \mathcal{P}_R)} \\ &= \frac{(22.00 - 22.13)}{(22.00 + 22.13)} \\ &= -2.9 \times 10^{-3} \end{aligned} \tag{65}$$

where $\mathcal{P}_L(\mathcal{P}_R)$ is the mean electron beam polarization for the left- (right-) handed electron beam from Figure 5.3. The polarization asymmetry gives a 6.4×10^{-4} % correction to the A_{LR}, which is negligible.

Energy Asymmetry

A primary source of the energy asymmetry is a beam current asymmetry for left- and right-handed polarized electron beam via beam-loading of the accelerator. The energy spectrometer was not synchronized with the electron beam helicities and there was no direct measurement for the left-right asymmetry of the center-of-mass energy. There is an empirical relation for the SLC beam energy by the beam-loading of the accelerator:

$$E_{L/R} = E_0 - \frac{200\ MeV}{10^{10}} I_{L/R} \tag{66}$$

where $I_{L/R}$ is the measured electron intensity in a bunch for the left (right) polarized electron beam and E_o is the measured center-of-mass energy. We measured the beam current asymmetry from the toroid signals and it was $(1.29 \pm 0.55) \times 10^{-4}$. The A_E is then:

$$A_E = -\ 7.9 \times 10^{-7}$$

This gives $7.0 \times 10^{-3}\%$ correction in the A_{LR}, which is negligible.

Acceptance/Efficiency Asymmetry

As long as the efficiency for detecting a fermion at a polar angle is the same as that of an antifermion at the same polar angle, A_{LR} is insensitive to the detector acceptance and efficiency. Since the SLD detector has a uniform and symmetric solenoidal field, the product of the acceptance and the efficiency is polar-angle symmetric for fermions and antifermions. Hence, A_ϵ is consistent with zero.

Luminosity Asymmetry

The most likely source of a significant left-right luminosity asymmetry is the asymmetry in the beams emitted by the polarized electron source and the effect is expected to be very small. The luminosity asymmetry can be measured from small-angle Bhabha scattering events, which is the best tool for the measurement of the luminosity asymmetry. Since there are only 25,615 small-angle Bhabha events, with 12,832 events produced with left-handed electron beam and 12,783 events produced with right-handed electron beam, in the 1992 polarized run, we can not use the small-angle Bhabhas for the luminosity asymmetry measurement due to the statistical error. If we use small-angle Bhabha events for the luminosity asymmetry measurement, there is a 2.7% uncertainty in the A_{LR} correction.

Instead of using the small-angle Bhabha events, three electron beam parameters which determine the SLC luminosity are used for more precise $A_{\mathcal{L}}$ determina-

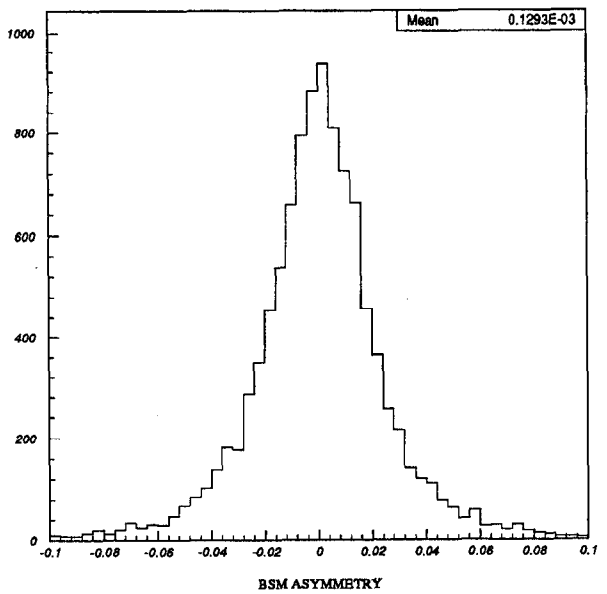

Figure 5.4 Beamstrahlung asymmetry for left- and right-handed polarized beam.

tion: beam current, electron-positron beam offset, and beam size. The luminosity asymmetry $A_{\mathcal{L}}$ has a relationship with the above three quantities:

$$A_{\mathcal{L}} = A_{N^-} + A_{\sigma_-} + A_{\triangle} \tag{67}$$

where A_{N^-} is the beam current asymmetry, A_{σ_-} is the beam offset asymmetry, and $A_{\triangle}$ is the beam size asymmetry. The beam size asymmetry is not measured directly but it can be extracted from the flux of the beamstrahlung photons produced by beam-beam interaction:

$$A_{BSM} = A_{N^-} - 0.3A_{\triangle} \tag{68}$$

where A_{BSM} is the detected beamstrahlung photon flux asymmetry for left- and right-handed polarized beam. Figure 5.4 shows the beamstrahlung asymmetry over

Systematic Error	Contribution (%) ($\delta A_{LR}/A_{LR}$)
Polarization Measurement	2.7
Luminosity Uncertainty	1.9
Background Uncertainty	0.7
Total	3.4

Table 5.1 Total Systematic Uncertainties in the A_{LR} measurement.

the whole 1992 run and is measured as $(1.3 \pm 1.0) \times 10^{-4}$.

$$A_{N^-} = (1.29 \pm 0.55) \times 10^{-4} \tag{69}$$

$$A_{\sigma_-} = (0.2 \pm 1.0) \times 10^{-4} \tag{70}$$

From the values of these three quantities, $A_{\mathcal{L}}$ is $(1.8 \pm 4.2) \times 10^{-4}$. Thus, the correction from the luminosity asymmetry in the A_{LR} is 0.08% and it is negligible. Since there is a large uncertainty in the luminosity asymmetry and it gives a 0.19% uncertainty in the correction of the A_{LR} value, this uncertainty will be considered as a systematic error instead of correcting the A_{LR} value.

Total Systematic Error

Table 5.1 shows the summary of the main systematic errors in the A_{LR} measurement.

Extraction of the Electroweak Mixing Parameter

When we consider all the corrections described above, A_{LR} in Eq. (63) is

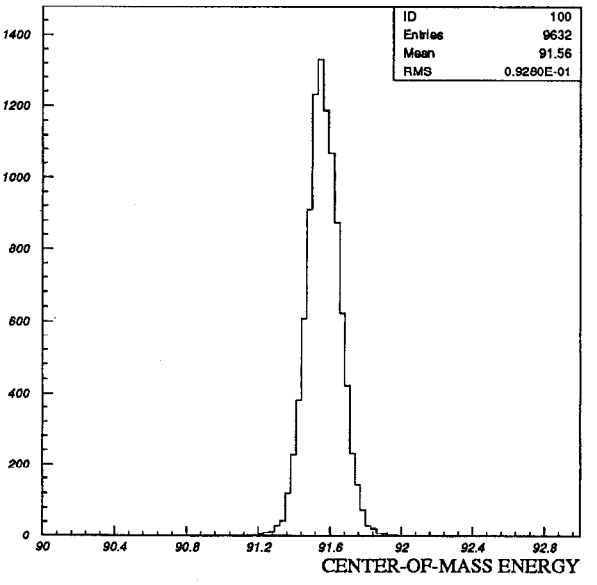

Figure 5.5 Center-of-mass energy distribution of the final data set.

replaced by,

$$A_{LR} = 0.102 \pm 0.044 \pm 0.003 \tag{71}$$

where the second and third terms are the statistical and systematic errors, respectively. From the relationship between A_{LR} and the effective electroweak mixing angle ($\sin^2\theta_w^{\text{eff}}$), Eq. (19), is extracted:

$$\sin^2\theta_w^{\text{eff}} = 0.2372 \pm 0.0056 \pm 0.0004 \tag{72}$$

where the second and third terms are the statistical and systematic errors, respectively.

Corrections to the Electroweak Mixing Parameter

So far, all of calculations were based on the assumption that the center-of-mass energy is the same as the mass of the Z°.

The electron and positron beams pass through precision energy spectrometers before they are dumped after collision at the SLC interaction point. Figure 5.5 shows the distribution of the center-of-mass energies for the A_{LR} data sample after requiring that the energy of each beam should be greater than 45.4 GeV but less than 46.1 GeV. The average center-of-mass energy was 91.56 GeV. But we have to remember that A_{LR} is insensitive to the measurement uncertainty of the center-of-mass energy within several hundred MeV. Since the SLC was not running at the Z° pole, the effective electroweak mixing parameter should be corrected for this. The $ZSHAPE$ routine, which was modified for longitudinally polarized electron beam, was used for finding the correction due to the energy deviation from the Z° mass. The correction is 3×10^{-4} for the difference between the Z° pole and SLC center-of-mass energy, and for initial state radiation. The electroweak mixing angle is then:

$$\sin^2\theta_w^{\text{eff}} = 0.2375 \pm 0.0056 \pm 0.0004 \qquad (73)$$

Summary of Results

Of all triggered events in the 1992 polarized beam runs, 10,437 events were selected as good hadronic Z° or tau pair events.

The estimated background contamination in the selected event sample from the beam-related backgrounds and wide-angle Bhabha events was $(1.9 \pm 0.7)\%$. 10,224 out of 10,437 events were finally selected for the measurement of the left-right cross section asymmetry after checking the integrity of the polarization bits and the time separation between the polarization measurements and the Z° events.

The raw left-right cross section asymmetry was measured from these 10,224

Correction Source	Contribution (%) ($\delta A_{LR}/A_{LR}$)
Background	2
Left-right Polarization Asymmetry	6.4×10^{-3}
Left-right Energy Asymmetry	0.07
Left-right Efficiency Asymmetry	0
Left-right Luminosity Asymmetry	0.8
Total	2

Table 5.2 Corrections to the A_{LR} measurement from secondary sources.

events:

$$A_{LR}^{\text{mea}} = (2.23 \pm 0.99) \times 10^{-2}$$

where the second term is the statistical error.

The average luminosity weighted polarization was:

$$\langle \mathcal{P} \rangle \;=\; 22.4\% \pm 0.6\% \text{ (syst.)}$$

The left-right cross section asymmetry was measured:

$$A_{LR} = 0.100 \pm 0.044 \text{ (stat.)}$$

Table 5.2 shows the corrections in the A_{LR} due to several secondary effects. The A_{LR} was corrected for the secondary sources in the Table 5.2 and after accounting for the systematic errors in the Table 5.1. We find:

$$A_{LR} = 0.102 \pm 0.044 \text{ (stat.)} \pm 0.003 \text{ (syst.)}$$

The effective electroweak mixing angle was extracted from the A_{LR} value after correcting for the SLC center-of-mass energy deviation from the Z° pole and initial-state radiation:

$$\boxed{\sin^2\theta_w = 0.2375 \pm 0.0056 \text{ (stat.)} \pm 0.0004 \text{ (syst.)}}$$

Figure 5.6 shows the comparision of asymmetry values from the data of the LEP experiments [53] and the SLD experiment. The forward-backward asymmetry of the tau polarization (P_τ^{FB}) measures the same coupling as A_{LR} does. The tau polarization asymmetry (A_τ) is equal to A_{LR} in size with the assumption that lepton couplings to gauge bosons are the same (lepton universality).

Since the 1992 analysis of the A_{LR} was done with about 10,000 hadronic Z° events, the statistical error is the dominant uncertainty in the measurement. Our result shows that there is no inconsistency with the Standard Model prediction of the effective electroweak mixing angle within the statistical error.

Strained GaAs [54] instead of bulk GaAs is used for the photocathode with about 865 nm wavelength Ti:Sapphire laser [55] in the 1993 run. The SLC/SLD achieved more than 50,000 hadronic Z° events with above 60% longitudinally polarized electron beam in the 1993 run and the combined uncertainty in the effective electroweak mixing angle measurement is much improved, and is expected to be 0.001.

Figure 5.7 shows the A_{LR} dependence on the top quark mass (M_t) in the minimal Standard Model for a Higgs mass (M_H) of 200 GeV. The SLD A_{LR} measurement is given by the horizontal bands. The 1992 result is shown for both 68.3%

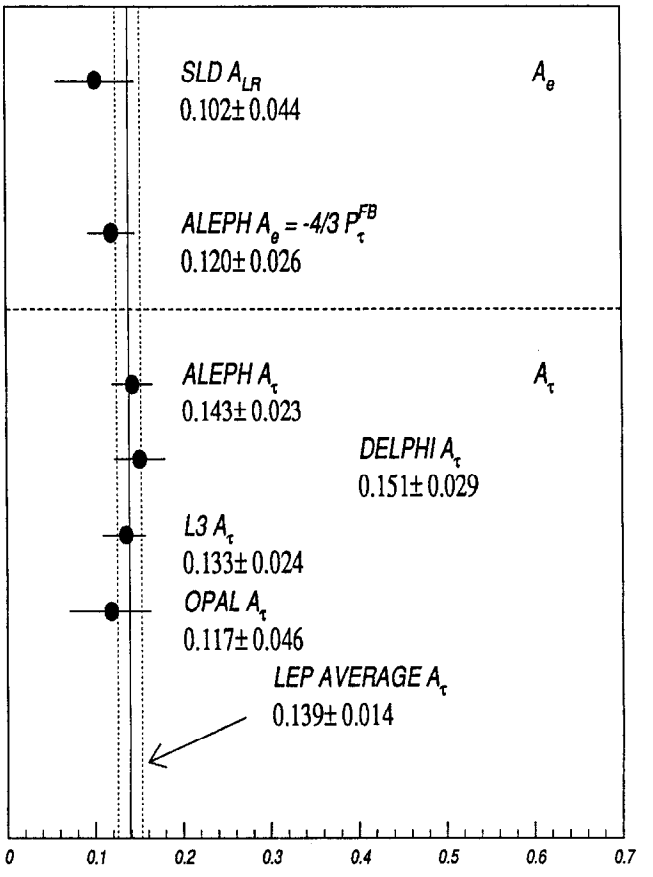

Figure 5.6 Comparision of the asymmetry measurements with LEP experiments.

and 95% confidence levels. The SLD measurement sets an upper limit on M_t at 205 GeV at 95% C.L. Also shown is the expected band (errors only) from the 1993 A_{LR} measurement.

Figure 5.8 shows a plot of the T and S_Z parameters [56], which characterize possible deviations from the Standard Model, for Γ_Z, Γ_{ee} [57] and the A_{LR} measurements with values of $M_t(\overline{MS})$ of 140 GeV and M_H of 200 GeV. The circle and cross points are for M_H of 200 GeV and 1000 GeV, respectively, for different top

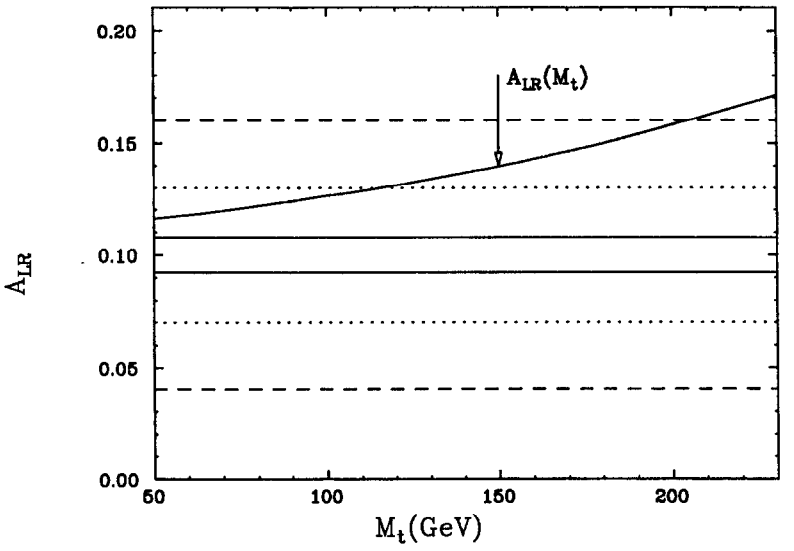

Figure 5.7 The curve gives the A_{LR} dependence on the top quark mass in the minimal Standard Model for M_H=200 GeV. The 1992 A_{LR} measurement is given as dotted and dashed bands for 68.3% and 95% confidence levels, respectively. The solid band gives the errors expected for the 1993 A_{LR} measurement.

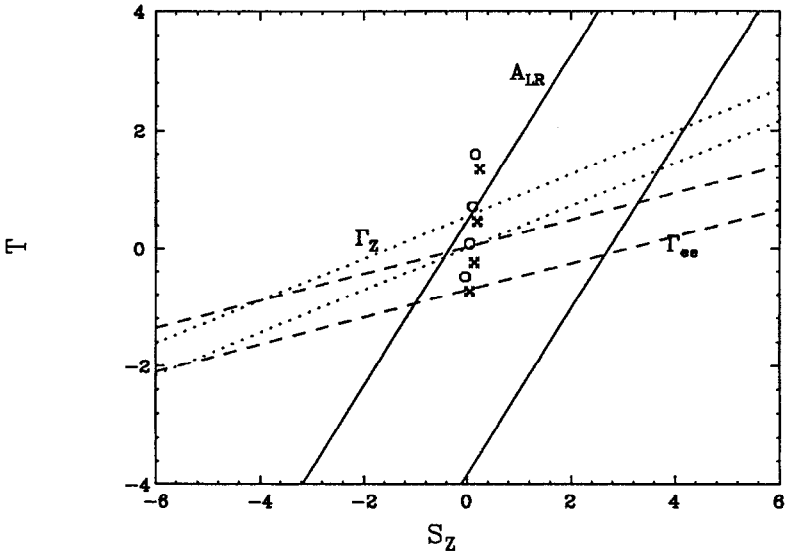

Figure 5.8 T versus S_Z plot for Γ_Z, Γ_{ee} and the 1992 A_{LR} measurements. Each circle and cross pair represents the Standard Model prediction for a given top quark mass, the pair at smallest T is for M_t=100 GeV, and the next pairs for M_t=150, 200, and 250 GeV. The circles and crosses are for a Higgs mass of 200 and 1000 GeV, respectively.

quark masses. Technicolor models [58] result in a shift in S_Z of about $1/6\pi$ for each heavy doublet, so that values of S_Z as large as $1-2$ are possible. However, for $M_t \geq 120$ GeV , the 1992 SLD result does not exclude this possibility.

CHAPTER VI

DISCUSSION

Introduction

In this Chapter, event selection procedures for the 1993 A_{LR} data sample, a study to improve background fractions with the LAC tower hit information, like the 1992 event selection procedures, and a study of event selection procedures with the help of the tracking in the central drift chamber, are presented.

1993 A_{LR} Event Selection

Introduction

Reconstructed cluster information from the LAC is used for selecting only hadronic Z° events for the 1993 A_{LR} analysis. The event selection procedures with the LAC clusters and background estimations in the A_{LR} data sample are described briefly in this section.

Event Selection

There are two stages for selecting hadronic Z° events. In the first stage the LAC tower hit information is used as an offline hadronic "trigger". Most non-Z° events are removed at this stage.

After applying high tower threshold cuts, which are 60, 60, 120, and 120 ADC counts on the four LAC layers, respectively, the total energy of the four LAC layers (E_{HI}) and total number of tower hits in the electromagnetic layers (N_{HIT}) are calculated. The total energy of four LAC layers (E_{LO}) is calculated after

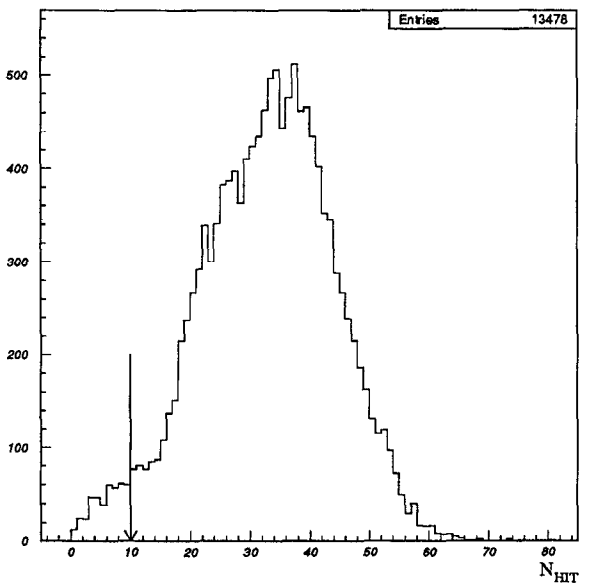

Figure 6.1 The distribution of the number of the electromagnetic tower hits after applying 60 ADC counts tower threshold cuts on the electromagnetic layers.

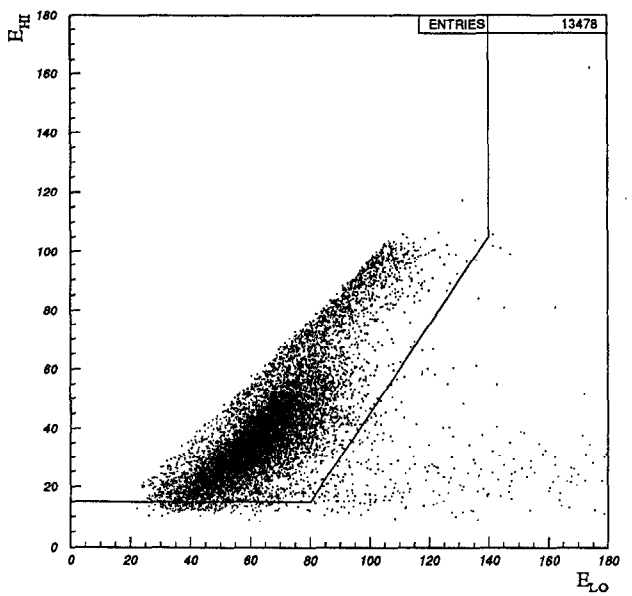

Figure 6.2 Sum of tower hits energy on the four LAC layers after applying high (E_{HI}) and low tower (E_{LO}) threshold cuts on the four LAC layers.

applying low tower threshold cuts which are 8, 8, 12, and 12 ADC counts on the four LAC layers, respectively. Energies of the electromagnetic and hadronic layers were obtained by multiplying conversion factors, 0.524/128 and 1.384/128, on the ADC values of the electromagnetic and hadronic layers, respectively. (This is the trigger energy scale described in Chpater 3; the trigger energy scale is twice the muonic energy scale.)

Figure 6.1 shows the distribution of N_{HIT} for events which passed the KZ0FLT filter which is described in Chapter 3. Since hadronic Z° events are expected to deposit some energy in the electromagnetic layers, the N_{HIT} cut was applied. The line shown in the Figure is the applied N_{HIT} cut:

- $N_{HIT} \geq 10$

Figure 6.2 shows the distribution of E_{HI} and E_{LO}. Since an SLC background muon deposits 20–30 ADC counts in the LAC layers, it is expected that most muon hits are discarded by applying high tower threshold cuts. Many SLC muon events are then populated in the region of low E_{HI} and high E_{LO}. The lines shown are the applied cuts for E_{HI} and E_{LO} in the trigger energy scale:

- $E_{HI} > 15$
- $E_{LO} < 140$
- $E_{HI} > 1.5 \times (E_{LO} - 70)$

In the second stage the reconstructed LAC cluster information is used for removing wide-angle Bhabha and tau pair events and further removing beam-related background events. For reconstructing clusters in the LAC, tower threshold cuts of 7 and 9 ADC counts for the electromagnetic and hadronic layers were applied and the towers which are closest to the beamline, $\Theta_{bin} = 48$, were removed.

The LAC cluster energy was calculated in the muonic energy scale and conversion factors, 439.0 ADC/GeV and 166.9 ADC/GeV, were used for the electromagnetic and hadronic layers, respectively. These conversion factors are lower by 10%

from the real conversion factors due to the 90% charge collection efficiency [59].

To be considered a good cluster, three requirements were made. Each cluster was required to have more than 100 MeV total energy deposition and non-zero energy deposition in the electromagnetic layers. The cluster was also required not to be identified as an SLC muon cluster.

When a cluster meets either the first or the remaining three conditions below, the cluster is considered to be an SLC muon cluster:

1. $N_{BAR} < 3$ or $N_{BAR} > 1000$

   where N_{BAR} is the number of the LAC barrel tower hits in the cluster.

2. $N_{PHI} \leq N_{TH} - 2$

   where N_{PHI} is the number of the adjacent LAC barrel tower hits in the layer and azimuthal plane, and N_{TH} is the number of the adjacent LAC barrel tower hits in the polar angle in the same layer and azimuthal angle.

3. $N_{PHI} \leq 20$

4. $N_{END} \leq 5$

   where N_{END} is the number of the tower hits in the endcap LAC.

Figure 6.3 shows the distribution of the total LAC cluster energy (E_{CLS}) versus energy imbalance (E_{IMB}) of the events which passed the first stage cuts. To remove beam-related background events which have low energy and high energy imbalance, E_{CLS} and E_{IMB} cuts were applied. The line shows the applied cuts for the E_{CLS} and E_{IMB}:

- $E_{CLS} > 15$ (muonic scale)
- $E_{IMB} < 0.6$

The number of clusters (N_{CLS}) is larger in the endcap than the barrel region due to relatively large electronics noise and its closer distance from the beamline. Figure 6.4(a) shows the number of clusters depending on the $|\cos\theta|$ of the thrust axis and the line is the applied number of clusters cut. Figure 6.4(b) and (c) are

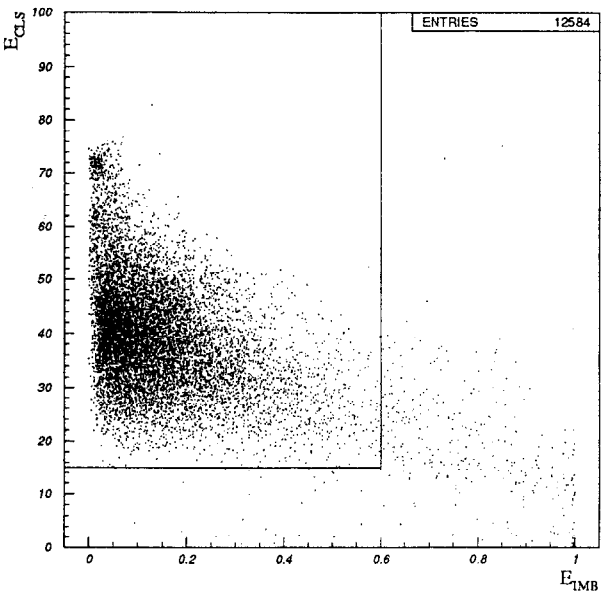

Figure 6.3 The scatter plot of the total energy deposition of the four LAC layers versus the energy imbalance of the events which passed the offline hadron "trigger".

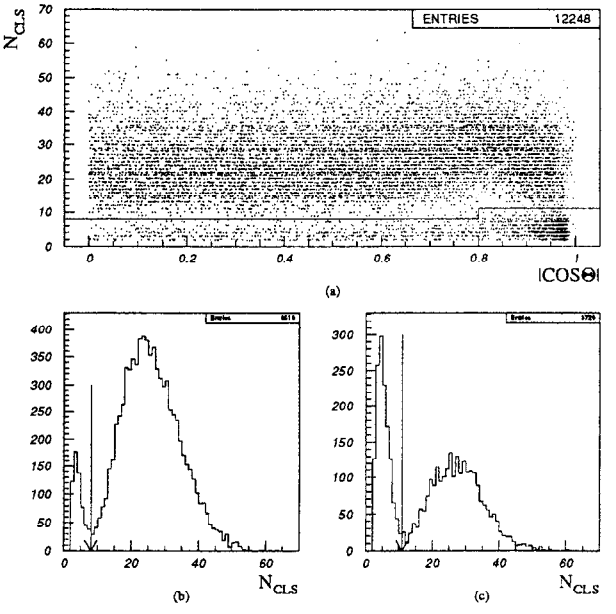

Figure 6.4 (a): The scatter plot of the number of good clusters for the LAC and the $|\cos\theta|$ value of the thrust axis. (b) and (c) are the distributions of the number of good clusters for $|\cos\theta| < 0.8$ and $|\cos\theta| \geq 0.8$, respectively. The lines are the applied number of clusters cuts depending on $|\cos\theta|$.

the distributions of the number of clusters for $|\cos\theta| < 0.8$ and $|\cos\theta| \geq 0.8$, respectively:

1. $N_{CLS} > 8$ for $|\cos\theta| < 0.8$
2. $N_{CLS} > 11$ for $|\cos\theta| \geq 0.8$

Background Estimation

10,002 events were selected as hadronic Z° events out of all triggered events in the 1992 polarized run after applying cuts which are described as the first and second stages. To estimate backgrounds from wide-angle Bhabha and beam-related events in the final selected events, the same methods which are described in Chapter 3 were used.

Table 6.1 shows the scan results of two scanners with the same event criteria as described in Chapter 3.

Background	Scanner 1	Scanner 2	Overlap
WAB	11	25	9
Beam-related	23	18	14

Table 6.1 Scan results of two scanners.

From the maximum-likelihood method, the background contamination of the event selection based on reconstructed calorimetry clusters is estimated to be $(0.6 \pm 0.3)\%$.

Modification of 1992 Event Selection

Introduction

A study for improving contaminations from wide-angle Bhabha and beam-related backgrounds with event selections based on the LAC tower hits information is presented.

Improving the KWABID filter

Since the KWABID filter identifies wide-angle Bhabha events (WABs) by the energy sum of four maximum tower hits in the electromagnetic layers of the LAC, WABs are mis-identified as hadronic Z^0 or tau pair events if transverse shapes of showering are large due to pre-showering or there is large energy leakage into hadronic layers.

To improve the selection of WABs, tower hit and energy information of the electromagnetic and hadronic layers of the LAC are used instead of using only four maximum electromagnetic tower hits, and the study is done with the events which passed the KZ0FLT filter.

Tower threshold cuts of 30 ADC counts are applied to the four LAC layers to calculate the energy deposition of the electromagnetic (E_{EM}) and hadronic layers (E_{HAD}) and the number of tower hits in the electromagnetic (E_{HIT}) and hadronic layers (H_{HIT}). All energy variables are calculated in the muonic scale.

Figure 6.5 shows the distribution of $(E_{HIT} + H_{HIT})/(E_{EM} + E_{HAD})$ versus $|\cos\theta|$ of the thrust axis, which was also calculated based on the LAC tower hits. Since WABs have relatively few tower hits but large energy deposition, the lower band in Figure 6.5 belongs to WABs. There is energy degradation in the deep endcap region. Cuts were determined separately depending on the $|\cos\theta|$ due to this energy degradation in the deep endcap region.

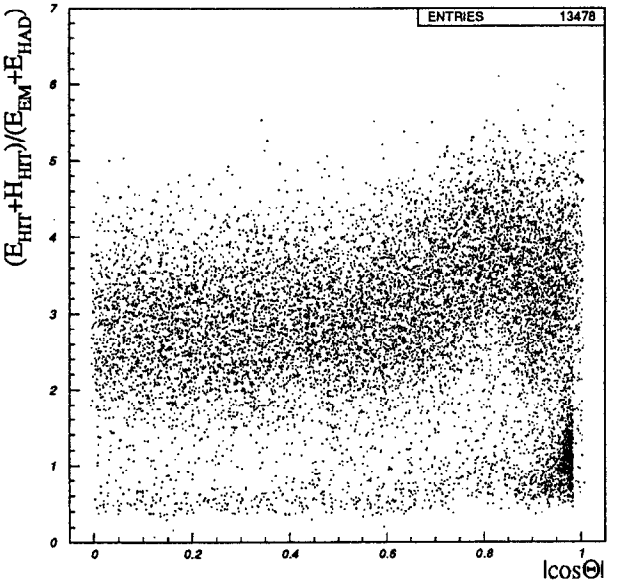

Figure 6.5 The distribution of the total LAC tower hits divided by the total LAC energy versus $|\cos\theta|$ of the thrust axis.

Figures 6.6 and 6.7 show the distributions of the energy-weighted hit (EWH) versus the hit-weighted energy (HWE) of the 1992 A_{LR} data sample and 13,478 events which passed the KZ0FLT filter for $|\cos\theta| < 0.95$, respectively. The EWH and HWE are defined:

$$EWH = \frac{(E_{EM} \times E_{HIT} + E_{HAD} \times H_{HIT})}{(E_{EM} + E_{HAD})} \tag{74}$$

$$HWE = \frac{(E_{EM} \times E_{HIT} + E_{HAD} \times H_{HIT})}{(E_{HIT} + H_{HIT})} \tag{75}$$

Figures 6.8 and 6.9 show the corresponding distributions of EWH versus HWE for the two data samples, where $|\cos\theta| \geq 0.95$. The solid lines shown are cuts which are applied to remove possible WABs.

The following cuts are applied for the EWH and HWE:

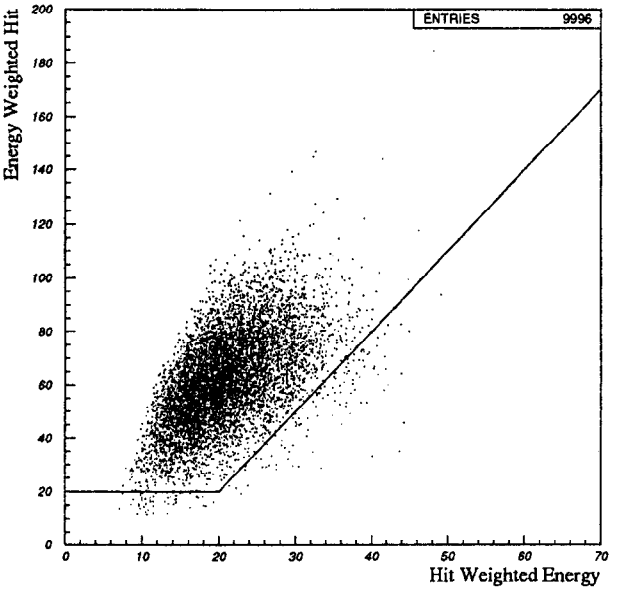

Figure 6.6 The scatter plot of the energy-weighted hits (EWH) versus the hit-weighted energies (HWE) for the 1992 A_{LR} data sample for $|\cos\theta| < 0.95$.

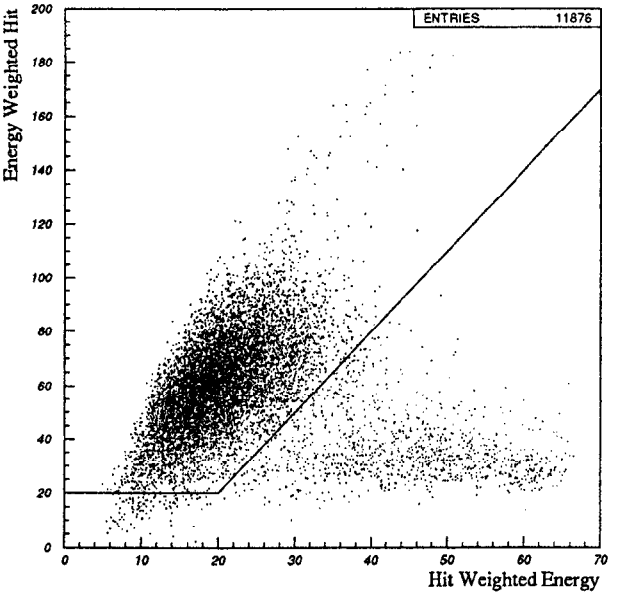

Figure 6.7 The scatter plot of the energy-weighted hits (EWH) versus the hit-weighted energies (HWE) for the events which passed the KZ0FLT filter for $|\cos\theta| < 0.95$.

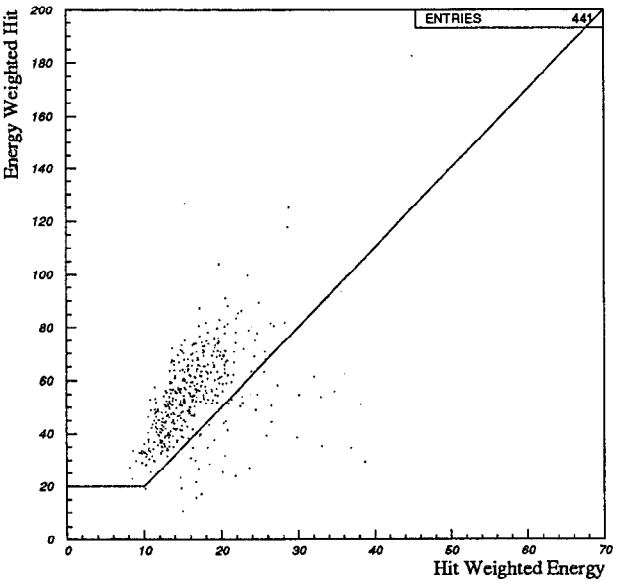

Figure 6.8 The scatter plot of the energy-weighted hits (EWH) versus the hit-weighted energies (HWE) for the 1992 A_{LR} data sample for $|\cos\theta| \geq 0.95$.

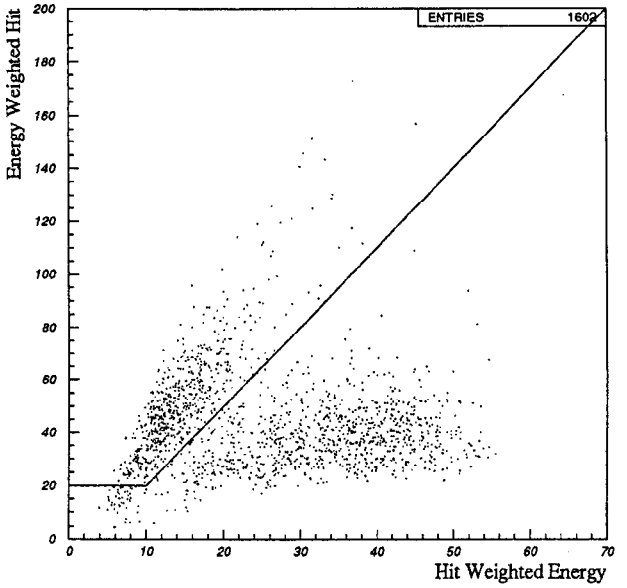

Figure 6.9 The scatter plot of the energy-weighted hits (EWH) versus the hit-weighted energies (HWE) for the events which passed the KZ0FLT filter for $|\cos\theta| \geq 0.95$.

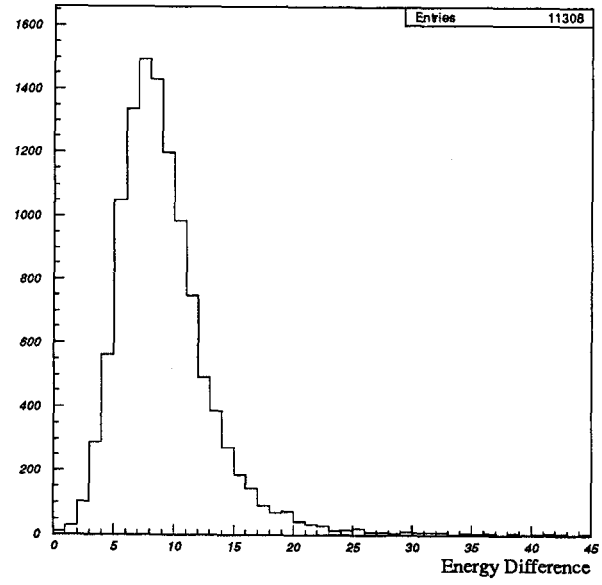

Figure 6.10 The distribution of the difference between the E_{LAC} and E_{TOT} for the events which passed the energy-weighted hit and hit-weighted energy cuts.

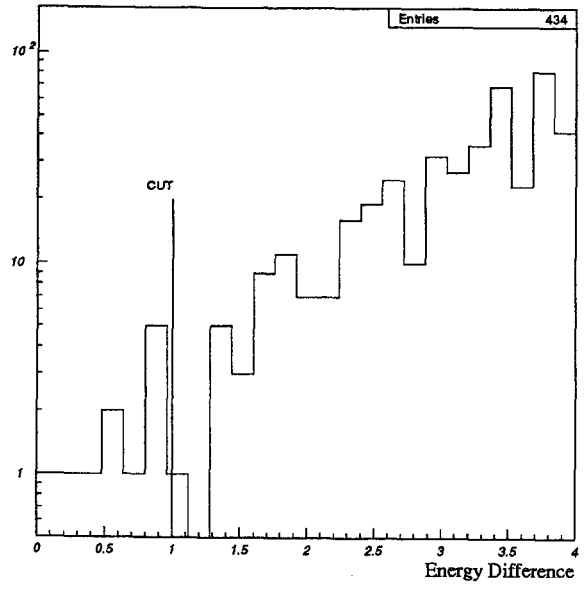

Figure 6.11 The distribution of the difference between the E_{TOT} and E_{LAC} for the events which have less than 4 GeV difference.

1. $EWH > 20$ and $EWH > 3 \times (HWE - 40)$ for $|\cos\theta| < 0.95$
2. $EWH > 20$ and $EWH > 3 \times (HWE - 10)$ for $|\cos\theta| \geq 0.95$

Of 10,437 events, 219 events failed by these cuts and 54 events out of the 219 events turned out to be background by the previous handscan. Out of 54 background events, 44 were classified as WABs. Of the 13,478 KZ0FLT events, 2,170 events failed and 11308 events passed these same cuts.

Since good WABs are expected to deposit most of their energy in the electromagnetic layers (E_{TOT}), E_{TOT} is compared with the summed LAC energy (E_{LAC}) after applying 30 ADC counts tower threshold cuts on the four LAC layers. Figure 6.10 shows the distribution of ($E_{LAC} - E_{TOT}$) for all events after the EWH and HWE cuts and Figure 6.11 is for events which have less than 4 GeV energy difference between the E_{LAC} and E_{TOT}. The following cut is made for further removing WABs:

- $E_{LAC} - E_{TOT} > 1$

Of 11,308 events, 11 events failed by this cut and all of these events were classified as WABs by handscan.

Improving the KMONOJT filter

To remove beam-related backgrounds the energy ratio of the hadronic to electromagnetic layers ($E_{RATIO} = E_{HAD}/E_{EM}$) was examined. Figure 6.12 shows the E_{RATIO} distribution. The following cut is made:

- $E_{RATIO} < 3$

206 events failed by applying $E_{RATIO} < 3$.

Beam-related backgrounds are expected to have small E_{TOT} no matter how many tower hits in the four LAC layers they have. Figure 6.13 shows the distribution of the E_{TOT} versus the number of tower hits in the LAC (N_{LAC}) above readout tower thresholds. The following cut is made:

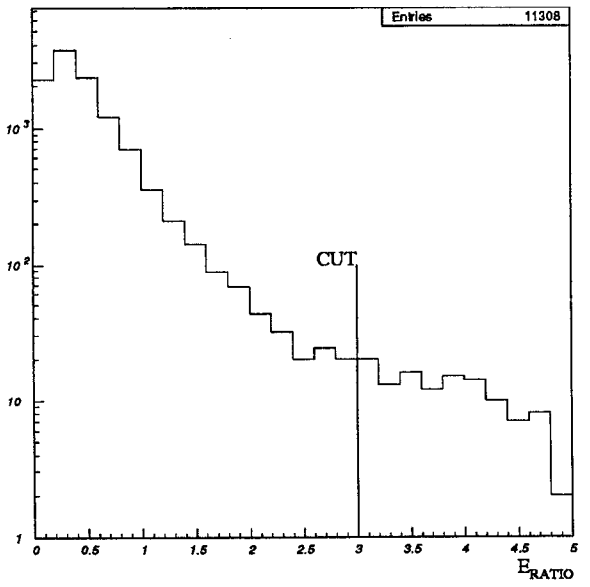

Figure 6.12 The ratio distribution of the hadronic energy to the electromagnetic energy after applying 30 ADC counts tower thresholds on the four LAC layers.

- $E_{TOT} > 15$ for $N_{LAC} > 1000$

133 events failed after applying this cut.

Figure 6.14 shows the E_{TOT} and E_{IMB} distributions for events which passed all of the above cuts. To further remove beam-related backgrounds, a tight E_{TOT} cut is applied and a E_{IMB} cut is also applied.

- $E_{TOT} > 12$
- $E_{IMB} < 0.8$

The solid lines shown are the cuts which are applied for E_{TOT} and E_{IMB}. Finally of 13,478 events, 9,877 events passed all of the above cuts.

44 events out of 9,877 were background events from the previous handscan results which are presented in Chapter 3. 24 out of 44 events were WABs and 20 are beam-related background events. 149 events are not in the 1992 A_{LR} data

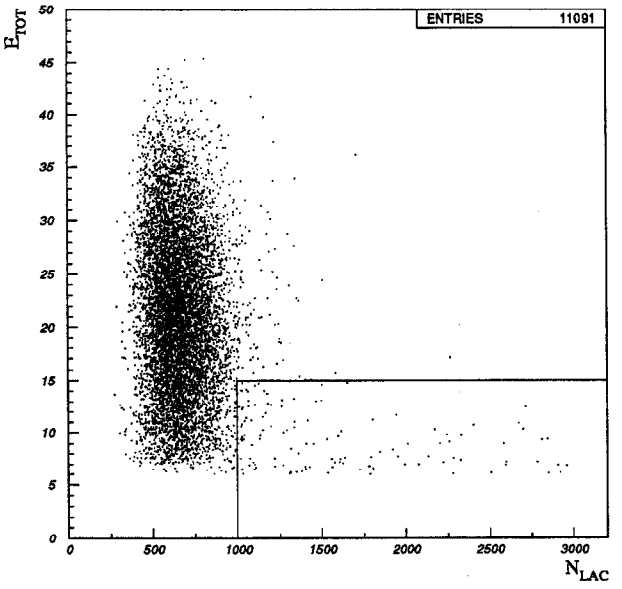

Figure 6.13 The scatter plot of the E_{TOT} versus the number of tower hits above readout tower threshold cuts.

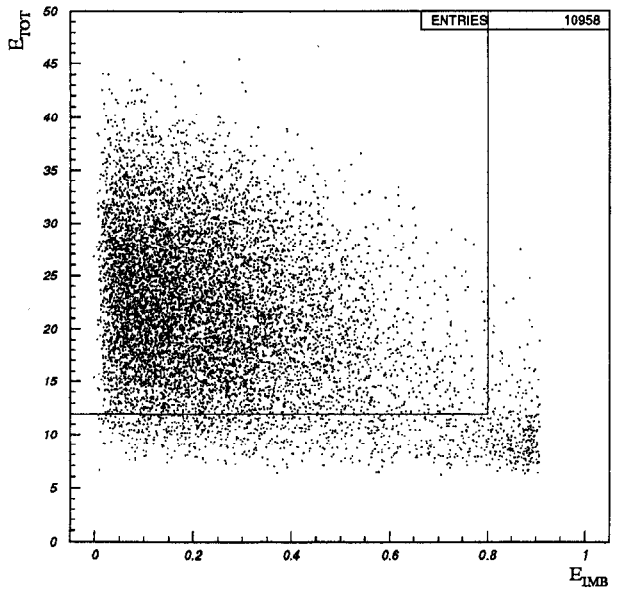

Figure 6.14 The scatter plot of E_{TOT} versus E_{IMB}.

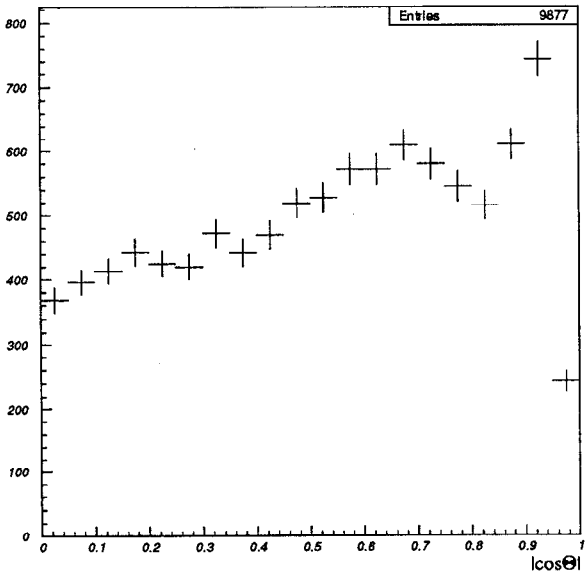

Figure 6.15 Angular distribution for final selected events.

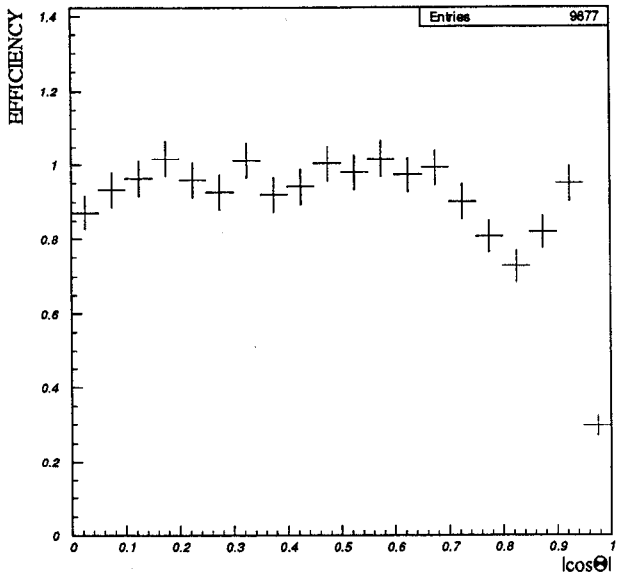

Figure 6.16 Efficiency distribution as a function of the acceptance of the LAC for final selected events.

sample and 86 events out of 149 are identified as good events by using fitted track information in the CDC, which will be described in the next section. 63 (149−86) events are handscanned and 6 events are classified as WABs and 5 are classified as beam-related backgrounds. The total estimated background by handscan is 0.6%.

Figure 6.15 shows the $|\cos\theta|$ distribution of the thrust axis for the final selected events and Figure 6.16 is the efficiency distribution as a function of $|\cos\theta|$. The lower efficiency of this procedures compared with the 1992 event selection procedures mostly comes from the deep endcap region ($|\cos\theta| > 0.95$).

Tracking Assisted Event Selection

Introduction

A study of the event selection with the LAC tower hit information and the central drift chamber (CDC) tracking information is presented in an effort to improve background contaminations [60].

Event Selection Procedure

The 1992 A_{LR} data sample was selected by the procedures based on tower hit information of the LAC and endcap WIC pads, as described in Chapter 3. The SLD is expected to have 50,000 hadronic Z° with high polarization in the 1993 run and it will be important to reduce beam-related and wide-angle Bhabha backgrounds in the A_{LR} runs with high statistical precision.

As an approach to reduce the backgrounds, the study of the hadronic Z° and tau pair events selection using tracking information, along with the LAC and WIC tower hits information, was done. The study was done with 13,478 events which passed the KZ0FLT filter with the 1992 polarized run. 9,013 of these events have fitted track information as found by the CDC. There are many reasons that events do not have the fitted track information. Endcap events do not have the CDC

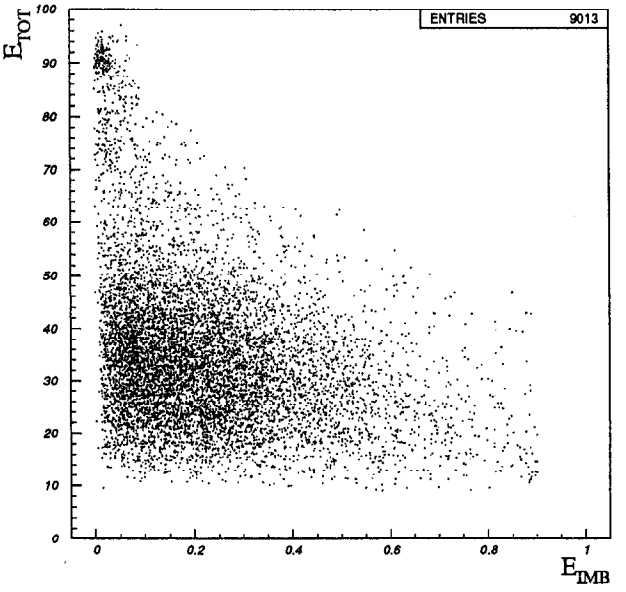

Figure 6.17 Total LAC energy versus energy imbalance distribution for events which have fitted track information in the central drift chamber.

information. The CDC information will not be readout if there are superlayer HV trips, as described in the "trigger" section in Chapter 2. "Energy trigger" events readout only the calorimetric part of the detector and do not have the CDC information.

Figure 6.17 shows the scatter plot of E_{TOT} (in the electronic energy scale) versus E_{IMB} for the events which have the fitted track information. By comparing with Figure 3.10, most beam-related background which have high-E_{IMB} and low-E_{TOT} are removed by simply requiring fitted tracks in the CDC.

Figure 6.18 and 6.19 are the distributions of the closest approach point of the track to the origin in the transverse plane relative to the beam axis and along the beam axis, respectively. The small peak around 5 cm in the negative Z direction is due to the SLC interaction point shift in runs 12431–12455. It was required that

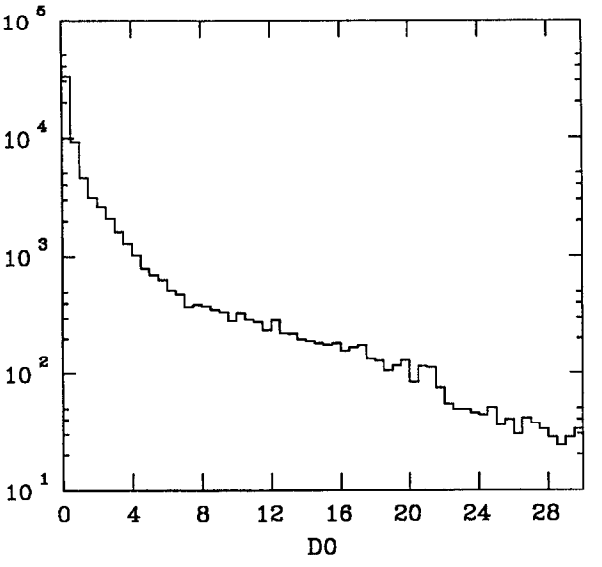

Figure 6.18 The distribution of the closest approach point (D0 in cm) of the track to the SLC interaction point in the transverse plane to the beamline.

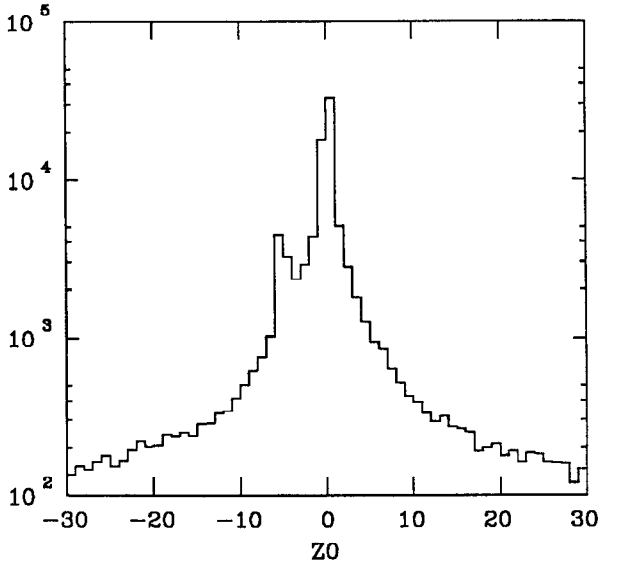

Figure 6.19 The distribution of the closest approach point (Z0 in cm) of the track to the SLC interaction point along the beamline.

the tracks be within 5 cm of the origin in the transverse plane and 10 cm along the beam axis, respectively. This is used as the definition of good tracks. Figure 6.20 is the scatter plot of E_{TOT} versus the number of good tracks (N_{CH}) for the 9013 events. Wide-angle Bhabha events appear in the region of high-E_{TOT} and $N_{CH} = 2$, and a N_{CH} cut was applied for removing wide-angle Bhabha events:

- $N_{CH} > 2$

Figure 6.21 is the scatter plot of the E_{TOT} versus E_{IMB} for $N_{CH} > 2$. By the handscan the events which are around 90 GeV with low-E_{IMB} and $3 < N_{CH} < 5$ are possible radiative wide-angle Bhabha or tau pair events. To make sure we do not include possible radiative wide-angle Bhabha events, the following cut is made:

- $E_{TOT} < 70$ GeV

From the handscan it is estimated that this procedure only retains less than 0.1% background from wide-angle Bhabha and beam-background events.

This procedure is compared with the 1992 A_{LR} data sample. 1,424 events were lost due to lack of tracking information and 924 events failed the good-tracking cut ($N_{CH} > 2$) and energy cut ($E_{TOT} < 70$). On the other hand this procedure introduced 390 new events which are not in the 1992 A_{LR} data sample. These events include many tau pairs which populate the low-N_{CH}, high-E_{TOT} region (mis-identified as wide-angle Bhabha events by the KWABID filter). Of the 390 events, about 150 events have less than 14.5 GeV energy (which is the E_{TOT} cut in the KMONOJT filter). Figure 6.22 shows that there is no edge in the low energy region compared with Figure 3.17(b) which has an edge where the E_{TOT} cut is applied.

From the study, it may be expected that the good track and E_{TOT} cuts are enough to remove most beam-related background and wide-angle Bhabha events. But since it is required that the efficiency of this procedure should be more than 95% to decrease the error in the A_{LR} measurement compared with the 1992 event

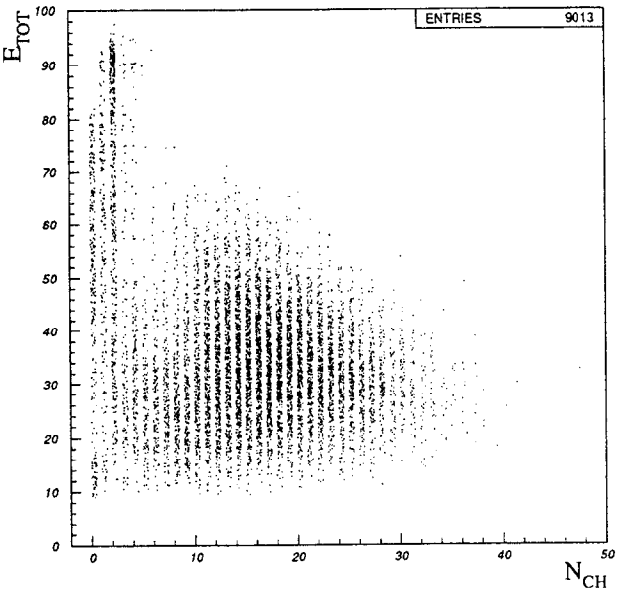

Figure 6.20 The distribution of the E_{TOT} versus the number of good tracks for events which have fitted track information in the central drift chamber.

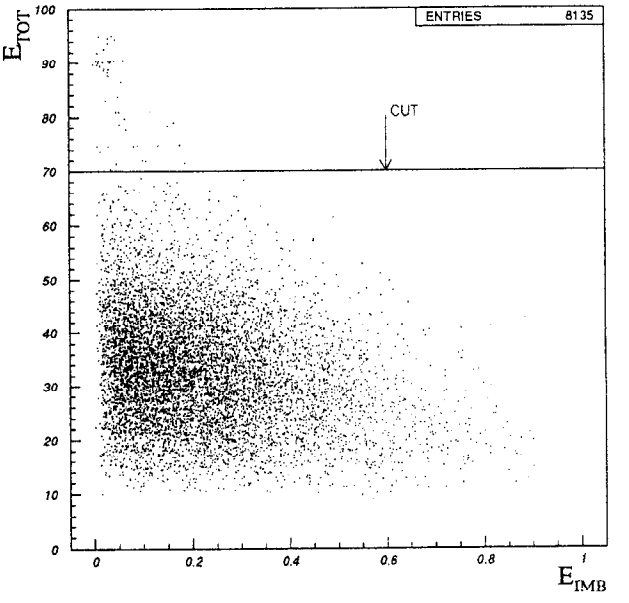

Figure 6.21 The distribution of E_{TOT} and E_{IMB} for the events which passed the number of good tracks cut ($N_{CH} > 2$).

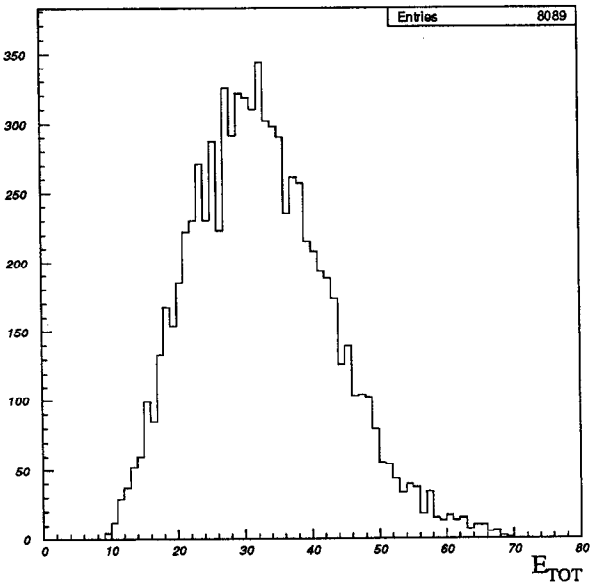

Figure 6.22 E_{TOT} distribution for the final selected events using the KZ0FLT filter and the number of good tracks cut.

selection procedures, it is suggested that the KAL-only procedure be used for events which do not have fitted tracking information and that the procedure described above be used for events which have fitted tracking information.

REFERENCES

[1] S.L. Glashow, Nucl. Phys. **22** (1961) 579; S. Weinberg, Phys. Rev. Lett. **19** (1967) 1264; A. Salam and J.C. Ward, Phys. Lett. **13** (1964) 13.

[2] E. Abers and B. Lee, Phys. Rep. **9C** (1973) 1; M.A.B. Bég and A. Sirlin, Annu. Rev. Nucl. Sci. **24** (1974) 379; D. Bailin, J. Phys. **G3** (1977) 321.

[3] P. Higgs, Phys. Rev. Lett. **12** (1964) 132.

[4] G. Arnison *et al.* (UA1 Collaboration), Phys. Lett. **126B** (1983) 398; P. Bagnara *et al.* (UA2 Collaboration), Phys. Lett. **129B** (1983) 130.

[5] F. Abe *et al.* (CDF Collaboration), Phys. Rev. Lett. **65** (1990) 2243.

[6] D. Decamp *et al.* (ALEPH Collaboration), Z. Phys. **C53** (1992) 1.

[7] P. Abreu *et al.* (DELPHI Collaboration), Phys. Lett. **B276** (1992) 536; O. Adriani *et al.* (L3 Collaboration), Phys. Lett. **B292** (1992) 454; D. Decamp *et al.* (ALEPH Collaboration), Phys. Lett. **B263** (1991) 325; R. Akers *et al.* (OPAL Collaboration), CERN-PPE-93-149, July (1993), submitted to Z. Phys. C.

[8] J.C. Taylor, "Gauge Theories of Weak Interactions", N.Y. Cambridge University Press (1976) p.105.

[9] V. Barger and S. Pakvasa, Phys. Lett. **B81** (1979) 195; G. Kne and M. Peskin, Nucl. Phys. **B195** (1982) 29.

[10] Review of Particle Properties, Phys. Rev. **D45** (1992) VII 145.

[11] G. Bardin *et al.*, Phys. Lett. **137B** (1984) 135.

[12] The LEP Collaborations, CERN-PPE-93-53, March (1993).

[13] D.C. Kennedy, B.W. Lynn, C.J.-C. IM, and R.G. Stuart, Nucl. Phys. **B321** (1989) 83.

[14] R. Kleiss *et al.*, CERN 89-08, Vol. 3 (1989) p.50.

[15] R. Kleiss, F.M. Renard, and C. Verzegnassi, Nucl. Phys. **B286** (1987) 669.

[16] A. Blondel, B.W. Lynn, F.M. Renard, and C. Verzegnassi, Nucl. Phys. **B304** (1988) 438.

[17] M. Consoli and W. Hollik, CERN 89-08, Vol. 1 (1989) p.32.

[18] B.W. Lynn, M.E. Peskin, and R.G. Stuart, CERN 86-02, Vol 1 (1986) p.90.

[19] G. Passarino and M. Veltman, Phys. Lett. **B237** (1990) 537; W.J. Marcino and A. Sirlin, Phys. Rev. Lett. **46** (1981) 163.

[20] W.J. Marciano, Ann. Rev. Nucl. Part. Sci. **42** (1991) 469.

[21] G. Altarelli, CERN 88-06, Vol. 1 (1988) p.13.

[22] D. Blockus *et al.*, Proposal for Polarization at the SLC, April (1986).

[23] K. Pitts, SLD Physics Note 20, April (1993).

[24] M.L. Swartz, SLAC-PUB-4689, July (1988).

[25] M. Woods, J. Frisch, K. Witte and M. Zolotorev, SLAC-PUB-5965, Dec. (1992).

[26] V. Bargman, L. Michel and V.L. Telegdi, Phys. Rev. Lett., **2** (1959) 435.

[27] M.J. Fero *et al.* (SLD Collaboration), SLAC-PUB-6026, Dec. (1992).

[28] S.B. Gunst and L.A. Page, Phys. Rev. **92** (1953) 970.

[29] G. Blaylock, SLD Physics Note 22, June (1993).

[30] SLD Design Report, SLAC-273 (1984).

[31] C.J.S. Damerell *et al.*, Nucl. Instr. Meth. **A288** (1990) 236.

[32] S.C. Berridge *et al.*, IEEE Trans. Nucl. Sci. **39** (1992) 1242.

[33] T. Markiewicz and L. Rochester, SLD Note 231, March, (1993).

[34] K. Abe *et al.*, SLAC-PUB-6276, "Performance of the CRID at SLD", Invited talk at Workshop on Rich Imaging Čerenkov Detectors, Bari, Italy, June 2–6, (1993).

[35] D. Axen *et al.*, Nucl. Instr. Meth. **A328** (1993) 472.

[36] A.C. Benvenuti *et al.*, Nucl. Instr. Meth. **A290** (1990) 353.

[37] M. Breidenbach *et al.*, IEEE Trans. Nucl. Sci. **36** (1989) 23.

[38] H. Park, R. Ben-David, R. Dubois, R. Frey and P.C. Rowson, SLD Phys. Note 17, Feb. (1993).

[39] R. Dubois *et al.*, IEEE Trans. Nucl. Sci. **33** (1986) 194; S. González, SLD Phys. Note 24, Oct. (1993).

[40] E. Vella and J. Yamartino, SLD Note 213, Feb. (1992).

[41] T. Sjöstrand, Comp. Phys. Comm. **28** (1983) 229.

[42] D.A. Evans and W.H. Barkas, Nucl. Instr. Meth. **56** (1967) 289.

[43] R. Ben-David and H. Park , SLD Phys. Note 18, July (1993).

[44] N. Phinney, Talk in SLD Collaboration Meeting at Saratoga, May (1993).

[45] R. Kleiss *et al.*, CERN 89-08, Vol. 3 (1989) p.50.

[46] S. Jadach and B. Ward, Phys. Rev. **D40** (1989) 3582.

[47] The LEP Collaborations, Phys. Lett. **B276** (1992) 247.

[48] P.N. Burrows, H. Park, K. Pitts, and J. Yamartino, SLD Note 229, Jan. (1993).

[49] J.A. Nash, SLAC-Report-356 (1990).

[50] M.J. Fero *et al.*, SLD Note 221, Oct. (1992).

[51] B. Schumm and R. Elia, SLD Note 222, Nov. (1992).

[52] S.D. Drell, SLD Note 226, Sep. (1992).

[53] P. Abreu *et al.* (DELPHI Collaboration), Z. Phys. **C55** (1992) 555; D. Decamp *et al.* (ALEPH Collaboration), Phys. Lett. **B265** (1991) 430; O. Adriani *et al.* (L3 Collaboration), Phys. Lett. **B294** (1992) 466; G. Alexander *et al.* (OPAL Collaboration), Phys. Lett. **B266** (1991) 201.

[54] T. Maruyama, Edward L. Garwin, R. Prepost, and G. Zapalac, Phys. Rev. **B46** (1992) 4261.

[55] J. Frisch, M.B. Woods, and M. Zolotorev, SLAC-PUB-5950, Oct. (1992).

[56] W.J. Marciano, Phys. Rev. **D20** (1979) 274; S. Fanchiotti and A. Sirlin, Phys. Rev. **D41** (1990) 319; J.L. Rosner, EFI-92-58, Nov. (1992), Presented at Particles and Fields 92, Batavia, IL, Nov. 10-14 (1992).

[57] The LEP Collaborations, CERN-PPE-93-157, Aug. (1993).

[58] W.J. Marciano, Presented at 19th Annual SLAC Summer Inst., July 26-Aug. 6 (1993).

[59] J.M. Yamartino, SLD Physics Note 14, Nov. (1992).

[60] H. Park, R. Frey, A. Lath, and P.C. Rowson, SLD Physics Note 19, April (1993).